Transport Phenomena in Bi_2Se_3 and Related Compounds

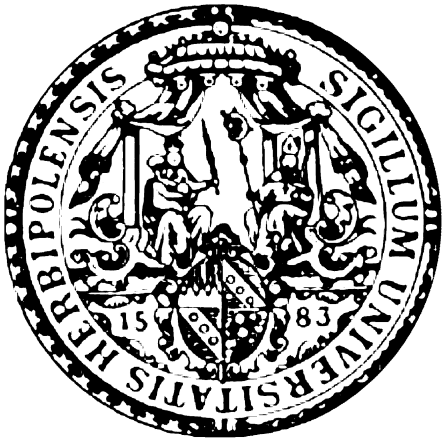

Dissertation zur Erlangung des
naturwissenschaftlichen Doktorgrades
der Julius-Maximilians-Universität Würzburg

vorgelegt von

Stefan Grauer
aus Würzburg

Würzburg, 2017

Dissertation, Julius-Maximilians-Universität Würzburg

Eingereicht am: 28.07.2017
bei der Fakultät für Physik und Astronomie

1. Gutachter: Prof. Dr. Laurens W. Molenkamp
2. Gutachter: Dr. Christian Schneider
3. Gutachter: .....
der Dissertation.

Vorsitzende(r) Prof. Dr. Jens Pflaum

1. Prüfer: Prof. Dr. Laurens W. Molenkamp
2. Prüfer: Dr. Christian Schneider
3. Prüfer: Prof. Dr. Haye Hinrichsen
im Promotionskolloquium

Tag des Promotionskolloquiums: 01.12.2017

Doktorurkunde ausgehändigt am: .....

Contents

List of abbreviations

1D	One-dimensional
2D	Two-dimensional
2-DEG	Two-dimensional electron gas
3D	Three-dimensional
AFM	Atomic-force microscopy
AHE	Anomalous Hall effect
ARPES	Angle-resolved-photo-emission
FT	Fourier transform
MBE	Molecular beam epitaxy
QAHE	Quantum anomalous Hall effect
QHE	Quantum Hall effect
QSHE	Quantum spin Hall effect
SdH	Shubnikov-de Haas
SOC	Spin-orbit coupling
SQUID	Superconducting quantum interference device
STS	Scanning tunneling spectroscopy
TEM	Transmission electron microscopy
TME	Topological magneto-electrical effect
TI	Topological insulator
TRIM	Time-reversal invariant momenta
UHV	Ultra-high-vacuum
LMR	Linear magnetoresistance
WL	Weak localization
WAL	Weak anti-localization
FWHM	Full width at half maximum
XRD	X-ray Diffraction

Chapter 1

Introduction

One of the most significant technological advances in history was driven by the utilization of a new material class: semiconductors. The earliest study of a semiconductor, the increase of conductance with temperature, goes back to Faraday in 1833. Progress in this field remained slow until the development of the band theory of solids by Wilson in 1931 [1], explaining the electronic states in a crystal, thus laying the theoretical groundwork for the understanding of the behavior of semiconductors. This led to the division of solids into three classes, metals and insulators which were already known and semiconductors, a new class of which the resistance and band gap is between that of an insulator and metal. The applications of semiconductors are manifold: transistors, diodes, LEDs and in thermoelectrics. New physics was observed as well, like the Quantum-Hall-Effect [2]. The technological advance in the semiconductor industry, however, is about to slow down. Making transistors ever smaller to increase the performance and trying to reduce and deal with the dissipative heat will soon reach the limits dictated by quantum mechanics with Moore himself, predicting [3] the death of his famous law in the next decade.

A possible successor for semiconductor transistors is the recently discovered material class of topological insulators [4–6], an addition to the three already known classes. A material which in its bulk is insulating but has topological protected metallic surface states or edge states at its boundary. These states originate from the nontrivial band structure, because its band inversion has to be lifted at the transition to a trivial band structure, and are protected by time

reversal symmetry. Their electrical transport characteristics include forbidden backscattering [4] and spin-momentum-locking [4, 6] with the spin of the electron being perpendicular to its momentum.
Topological insulators therefore offer an opportunity for high performance devices with low dissipation, and applications in spintronic where data is stored and processed at the same point. Additionally the majorana fermion is predicted at a superconductor to topological insulator interface [7]. A pair of bound and spatially separated majorana fermions, which posses non-Abelian exchange statistics would be a possible realization of a Quantum-Bit [8], providing another possibility to speed up certain computations.
Topological insulators offer interesting new physics as well and are predicted to host new phenomena. In the most developed topological insulator material, HgTe [9], the Quantum-Spin-Hall-Effect [4, 10] with two counter-propagating spin polarized edge channels, has already been shown by the group led by Molenkamp [11]. Another topological insulator material, magnetically doped $(Bi_{1-x}Sb_x)_2Te_3$, displays the Quantum-Anomalous-Hall-Effect [12], combining ferromagnetism with a topological insulator resulting in quantized conductance at zero external magnetic field. Also the existence of magnetic monopoles, until now unknown in nature, has been proposed in topological insulators [13].
There are several topological insulator materials with new ones still being discovered. The compounds Bi_2Se_3, Bi_2Te_3 and Sb_2Te_3 [14] offer relatively high energy band gaps, up to 0.3 eV in Bi_2Se_3, and a rather simple band structure with a single dirac cone at the gamma point of the Brillouin zone. Furthermore, unlike for example $Bi_{1-x}Sb_x$ [15], they are stoichiometric compounds and in principle no complicated methods, like introducing strain, pressure or accurately controlling the composition, are needed to make them work.

While there certainly already is a lot of progress in the field and technological advance is fast in our time topological insulators are still in the state of basic research. Their development is in progress for only a decade. For semiconductors it took almost a century from their discovery till their application. The expectations are already high, as indicated by over 5000 publications about topological insulators since 2005, but extensive research still needs to be done.
The existence of the surface state in Bi_2Se_3 and related materials was already

shown in spectroscopy measurements [16, 17]. The goal of this work is to search in these materials for evidence of the surface state in electrical transport experiments and explore its physics. As necessary requirements, the transport properties have to improved and knowledge about the transport behavior has to be gained. The main obstacle is the parasite high bulk doping, which dominates the electrical transport.

The theoretical background for understanding the new class of topological insulators and what makes a system a topological insulator will be given in the following chapter, along with a closer look at Bi_2Se_3 and related materials. Also the proof of the existence of a surface state in these materials by spectroscopy in literature is briefly reviewed.
The focus in chapter three is on the transport experiments done in this work. First the carrier density is examined in a one and two carrier model and ways to reduce the densities are investigated. The observed features in the magnetoresistance, namely linear magnetoresistance, weak anti-localization and Shubnikov-de Haas oscillations are discussed and analyzed in respect to their possible origin, the topological surface state or bulk carriers.
The most significant discoveries of this thesis are presented in chapter four and five, where the possibilities of magnetic doping with Cr and V are explored. As it turns out by doping with Cr or V, even in thin layers, out-of-plane ferromagnetism can be realized as confirmed by SQUID-measurements. This leads to a large anomalous Hall effect which can be amplified by tuning the growth and composition of the material. This leads to the Quantum-Anomalous-Hall-Effect, edge channel transport with quantized conductance at zero external magnetic field, which is realized and studied [18]. Finally, by studying the flow diagram of this state, the realization of the "axion insulator" is proven for the first time. This demonstrates the proposed existence of a new term in Maxwell's equations stemming from the magnetic monopole [13].
At the end of the thesis a summary will be given in English as well as in German.

Chapter 2

Topological Insulators

In this chapter first a general overview of the theory of topological insulators (TIs), and subsequently with a focus on Bi_2Se_3 and related compounds is given. Following that, evidence from the literature for the existence of a topological surface state with a linear dispersion found in these materials is shown.

2.1 Theoretical background

Topological insulators are a new material class. It is defined by a band gap in the bulk, like an insulator, but with the addition of a metallic state on its boundary, protected by time reversal symmetry, with a linear dispersion relation. They exist as two-dimensional (2D) systems, e.g. HgTe quantum wells with topological states on the edge, and as three dimensional (3D) systems, e.g. Bi_2Se_3 or strained HgTe, with states on the surface. These states are a consequence of the nontrivial topology of the bandstructure of the material which, at its boundary, has to be changed to a trivial one.

2.1.1 Topology of the band structure

Topology as a description for the band structure of a material was first introduced for the Quantum-Hall-Effect (QHE) [19]. In a sufficiently strong magnetic field the carriers of a two dimensional electron gas (2-DEG) form one dimensional (1D) chiral channels at the edges, while all the other carriers localize. The number of edge channels n and the quantized value of the Hall conductivity $\sigma_{xy} = \frac{ne^2}{\hbar}$ can

be expressed by the Chern number $n \in \mathbb{Z}$ [19, 20]. The value of this number follows from topological constraints to the electron wave function which, in this case, are given by the magnetic field.
Similarly, as proposed by Kane [5], the topology of the band structure of an insulator can be described by a Z_2 topological invariant for time-reversal invariant systems. A Z_2 invariant only has two possible values. The first on is 0, which in this case resemble a trivial insulator and the second one is 1, a TI with edge or surface states. A demonstrative way to explain this classification is to start with an insulator with a band gap. The Fermi energy lies inside the band gap and at the boundary of the insulator there may or may not be states existing in the gap. Two kind of symmetries have to be considered. First, the time reversal symmetry under which $\vec{k}$ is odd and E is even. Therefore it is sufficient to consider only positive k-values, since $E(\vec{k}) = E(-\vec{k})$. Second, the translational symmetry which maps $\vec{k}$ to $\vec{k} + \vec{K}$, with the reciprocal lattice vector $\vec{K}$, and therefore $E(\vec{k}) = E(\vec{k}+\vec{K})$. By combining both symmetries some special points in the Brillouin zone can be mapped onto themselves: the so called time-reversal invariant momenta (TRIM) Γ_i. As a consequence the TRIM have to be two-fold degenerate, usually the degeneracy between spin-up and spin-down electrons. Away from these special points the degeneracy can be lifted. At the 1D boundary of a 2D system there are two TRIM and there are two differing cases, as displayed in fig. 2.1. Either the states in the gap cross the Fermi energy an even amount of times, including zero and no states in the gap, or an odd amount of times. By a smooth transformation of the Hamiltonian the states in the gap can be pushed away from the Fermi energy, but the number of crossings can only change by two at a time. Therefore, by a smooth transformation, an even amount of crossings can be reduced to zero: the states are not protected against perturbations and will easily localize. An odd amount of crossings on the other hand cannot be reduced to zero. There is always a single remaining state protected by time reversal symmetry, the edge or surface state. These two cases differ in their topology of the band structure and the number of crossings n can be used to determine the topological Z_2 invariant ν:

$$\nu = n \bmod 2 \ . \tag{2.1}$$

In three dimensions there are in total four Z_2 invariants, $\nu_0; (\nu_1\nu_2\nu_3)$ [6], but only

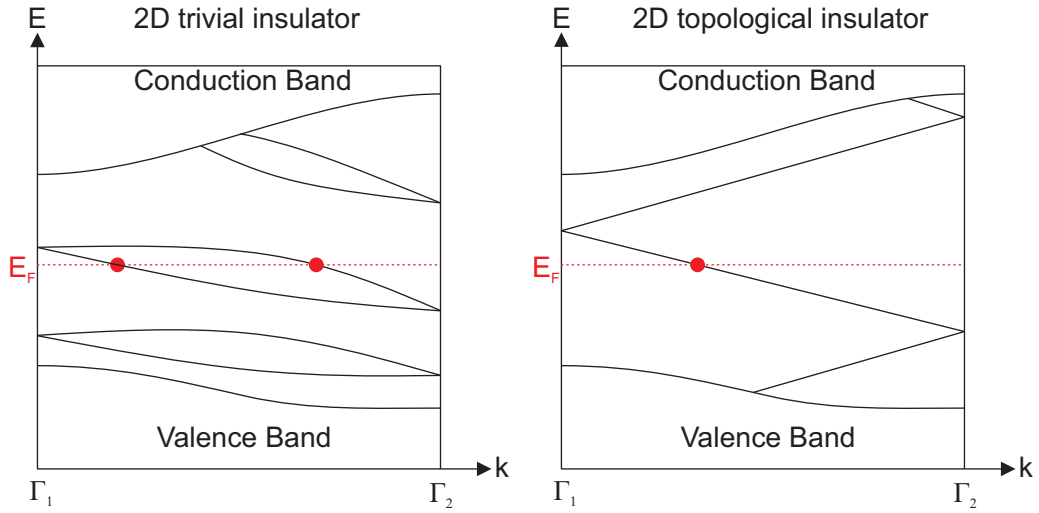

Fig. 2.1: Schematic band structure for a two dimensional trivial insulator and a TI, with one dimensional edge states in the gap. The trivial insulator has an even amount of crossing of the Fermi energy, for example two as marked by the red dots, and the TI has and odd amount. For the trivial insulator the bands can be pushed in a way that no more states exist at the Fermi energy. For the TI this is not possible.

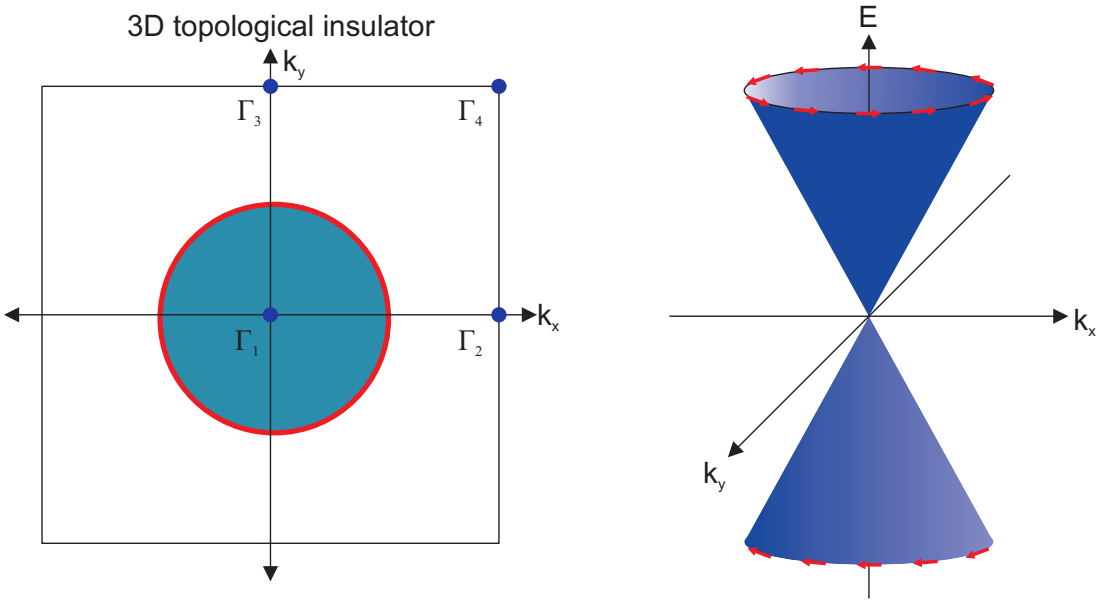

Fig. 2.2: The schematic band structure of a three dimensional TI, with a two dimensional surface state around a single dirac point and the dispersion of the resulting surface state, a Dirac cone, is shown. The red arrows represent the spin polarization of the state.

the first one makes the distinction for a TI. In principle for every surface every connection between two of the now four TRIM can be visualized as the left or right side of fig. 2.1. As a result there are now either an even or an odd number of TRIM, also denoted as Dirac points, topologically protected enclosed by the Fermi surface arcs. The invariant ν_0 now defines the number of Dirac points of the surface which are enclosed by the Fermi surface arcs. For $\nu_0 = 0$ every surface has an even number, 0, 2, or 4, of Dirac points enclosed and, similar to the two dimensional case, changes by two are possible. There is no topological protection. If $\nu_0 = 1$ every surface has an odd number, 1 or 3, of Dirac points enclosed by the Fermi surface arcs and the state is topologically protected, like in the schematic in fig. 2.2 resulting in the also shown Dirac cone.

2.1.2 Determination of topological insulator materials

Now that the classification of TIs is established it is important to identify a material as a trivial or as a topological insulator. In inversion symmetric crystals there is a relatively simple criterion by which the distinction can be made. Namely the inversion of the valence and conduction band, with different parities, at one gamma point [6, 9, 21]. The former conduction band becomes a valence band and the former valence band is now the conduction band. This band inversion is a change of the topology of the band structure, it cannot be undone by a smooth transformation of the Hamiltonian. At the boundary to a material with a trivial band structure the inversion has to be lifted. The result is an additional Dirac point enclosed by the Fermi surface arc and therefore, as previously explained, a change in the Z_2 invariant. By examining the parity eigenvalue ξ of all occupied bands m at all gamma points in a inversion symmetric crystal the Z_2 invariant ν can be calculated as [21]:

$$(-1)^{\nu} = \prod \delta_i \ , \tag{2.2}$$

with

$$\delta_i = \prod_{m=1}^{N} \xi_{2m}(\Gamma_i) \ , \tag{2.3}$$

where it is only necessary to examine ξ_{2m}, because the bands $2m$ and $2m-1$ share the same parity eigenvalue as they are Kramers degenerate partners.

2.1.3 The topological insulators Bi_2Se_3, Bi_2Te_3 and Sb_2Te_3

To actually identify topological insulator materials one now needs to find an inversion symmetric crystal where the valence and conduction band have opposite parity and a band inversion occurs. A prominent mechanism for band inversion is strong spin-orbit coupling (SOC). The strength of SOC, E_{SOC}, is correlated to the nuclear charge Z, with $E_{SOC} \propto Z^4$, therefore heavy atom materials like Bi_2Se_3, Bi_2Te_3, Sb_2Se_3 and Sb_2Te_3, which are inversion symmetric crystals and where valence and conduction band have different parity, are promising candidates, as suggested by Zhang [14].

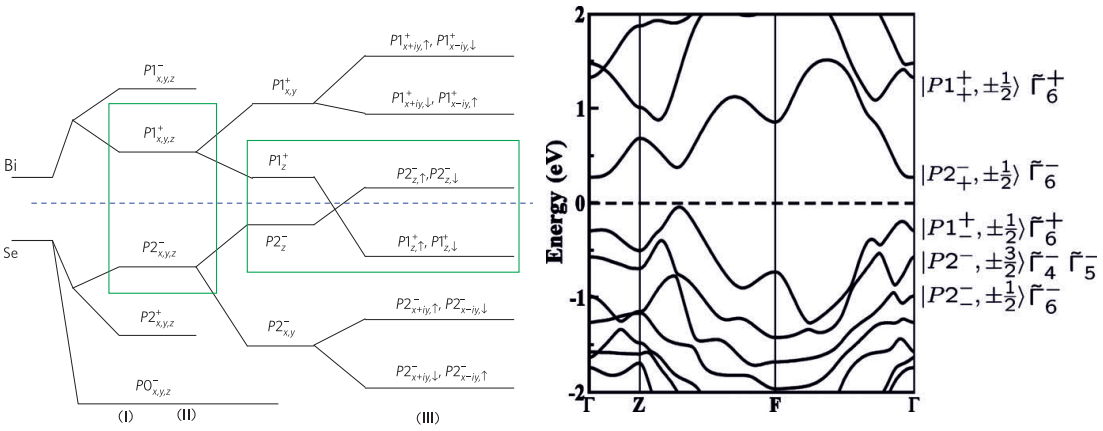

Fig. 2.3: On the left side a schematic of the band inversion at the Γ-point in Bi_2Se_3 taken from Zhang [14] is shown. Displayed is, starting from the atomic p-orbitals, the evolution of the energy of the bands at the Fermi energy by turning on chemical bonding (I), crystal-field splitting (II), and SOC (III), which leads to the band inversion of two bands with different parities, namely $P2_z^-$ and $P1_z^+$. On the right side the bulk band structure obtained from *ab initio* calculations by Liu [22] is shown.

In his paper he did a parity analysis of the highest eight occupied bands and found that by turning on the SOC the product of the parities changes at one gamma point, a consequence of the band inversion displayed in fig. 2.3, for Bi_2Se_3. Under the likely assumption that the lower bands remain occupied one δ_i in eq. 2.3 changes sign and with eq. 2.2 the Z_2 invariant ν and therefore the topolgical phase changes. In Bi_2Te_3 and Sb_2Te_3 the parity of the occupied bands changes as well, only for Sb_2Se_3, the material with the lightest atoms and therefore weakest SOC, it remains unchanged. The conclusion is, that the strong SOC leads to a

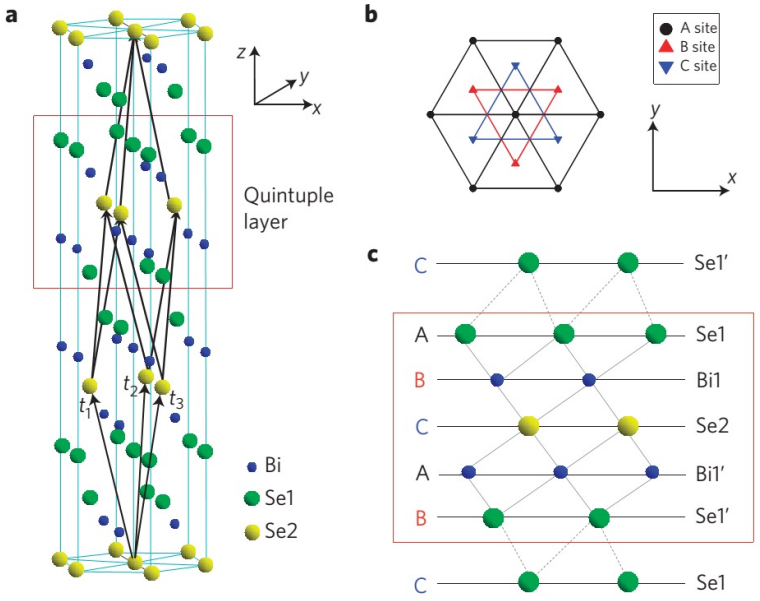

Fig. 2.4: The figure is taken from Zhang [14]. In a) the crystal structure for Bi_2Se_3, with the three primitive lattice vectors t_1, t_2, t_3 and a quintuple layer marked by a red square, is displayed. Part b) shows a top view of the hexagonal lattice structure with the three different positions A, B and C and c) a side view displaying the stapling order of these positions.

band inversion at the gamma point and, since the material without SOC can be assumed to be a trivial insulator, makes Bi_2Se_3, Bi_2Te_3 and Sb_2Te_3 topological insulators.

Bi_2Se_3 and the related materials have a rhombohedral crystal structure with the space group D^5_{3d} $R\bar{3}m$ and five atoms per unit cell. The atoms form a layered structure with five atomic layers making up a so called quintuple layer with a height of approximately 1 nm, as seen in fig. 2.4. The order in such a layer is Se-Bi-Se-Bi-Se and the bonds between these atoms are strong. In contrast the bond between two quintuple layers, two Se atoms, is a van-der-Waals bond and is therefore weak. The inversion symmetry of the crystal is given by the inversion center at the Se-atom in the middle of the quintuple layer. For Bi_2Te_3 Se is replaced by Te and for Sb_2Te_3 Bi and Se are replaced by Sb and Te respectively. The crystal structure remains otherwise the same.

2.1.4 Electrical transport in the topological surface state

What we want to observe is the electric transport of the surface state in these materials. To get some knowledge about the expected behavior, the properties of the topological surface state are examined.
As a prerequisite for achieving an odd number of crossings of the Fermi energy in the gap the spin degeneracy has to be lifted for the surface state away from the TRIM. Because the spin is odd under time reversal, the present time-reversal symmetry demands that two opposite points in k-space, $\vec{k_1}$ = -$\vec{k_2}$, also have opposite spin. For the surface state the spin direction rotates by 2π around the Dirac-point, as depicted in fig. 2.2. This means that upon making a closed cycle around the Dirac point the acquired phase of the state will be only π since the spin of an electron requires a 4π rotation to acquire a phase factor of 2π. For a time-reversal system the allowed values of the acquired phase are only 0 or π, otherwise two time-reversed paths would differ. Therefore smooth changes of the acquired phase for a closed path are not allowed and the value is the same for every closed path. This phase factor is called the Berry phase and is the cause of destructive interference for backscattering. This leads to the suppression of backscattering and the inability of the electrons to localize even in the presence of strong disorder a [23].
Under a strong magnetic field, as in a conventional 2-DEG, the topological surface state will form edge channels and show the QHE. But in contrast to the conventional 2-DEG the surface state shows the so called half-integer quantization [21]:

$$\sigma_{xy} = \left(n + \frac{1}{2}\right) \frac{e^2}{h} \text{ , with } n \in \mathbb{N}_0 \text{ .} \tag{2.4}$$

This is a consequence of the existence of a zero filling factor for Dirac electrons [24]. In the case for graphene this has been measured, but since in graphene there are four Dirac-points half-integer quantization is measured four times and a direct measurement of $\sigma_{xy} = \frac{1}{2}\frac{e^2}{h}$ is not possible. For a 3D TI there are at least two surfaces measured, the top and bottom one, again masking a direct observation of the half-quantization. But as a consequence one can measure a series of odd integer quantized levels $\sigma_{xy} = (2n+1)\frac{e^2}{h}$, as long as the difference in carrier density for the two different surfaces can be neglected, like it was done for the 3D TI strained HgTe [25].

Before making these observations in Bi_2Se_3 and related materials the carrier density has to be in the regime where an observation of the QHE is possible. A rough estimate of the expected carrier densities can be taken by considering ARPES measurements on for example Bi_2Se_3 [26]. Here the Fermi energy lies about 300 meV above the Dirac-point and about 100 meV above the minimum of the conduction band. The linear dispersion of the Dirac-state is $E_{surface}(k) = \hbar v_F k$ with $v_F = 5 \cdot 10^5$ m/s and the dispersion of the bulk state is $E_{bulk}(k) = \hbar k^2/(2m^*)$, with $m^* = 0.12$ m_e. This results in: $n_{surface} = 6 \cdot 10^{12}$ cm^{-2} and $n_{bulk} = 6 \cdot 10^{18}$ cm^{-3}. For an in the bulk insulating topological insulator the Fermi energy has to lie in the energy gap and the maximal distance to the Dirac-point would be about 200 meV resulting in a maximum carrier density of $n_{surface} = 3 \cdot 10^{12}$ cm^{-2}.

2.2 Evidence of the topological surface states in Bi_2Se_3 and related compounds

The first proposal of a TI [9] was swiftly realized in HgTe-quantum wells [11], where the edge states of this two dimensional system were measured in electrical transport experiments. The topological nature, with an insulating bulk, of this material is therefore proven, but HgTe remains a challenging material. The handling of the toxic Hg which is in its liquid phase at room temperature is dangerous and complicated and HgTe posses only a small band gap which is only opened by strain or dimensional restrictions [9]. Therefore it is worthwhile to look for alternatives to this already established material.

The proposal of Bi_2Se_3 and related compounds [14], previously only known for their thermoelectric properties [27], as topological insulators generated extensive interest in research. First crystals were swiftly synthesized and spectroscopic measurements, to prove the existence of the surface state, were done.

The first observation of the surface state in these materials was made in an angle-resolved photoemission spectroscopy experiment (ARPES) by Chen et al. [16] on Bi_2Te_3, an example of an ARPES measurements is displayed in fig. 2.5. The studied material is n-type and a state with a V-like shape connecting the valence and conduction band is revealed. This observation was confirmed in following ARPES measurements, as well for Bi_2Se_3 [26, 30–32], but not for Sb_2Te_3. Because Sb_2Te_3 is inherently p-doped [33], the Fermi energy is below the Dirac-

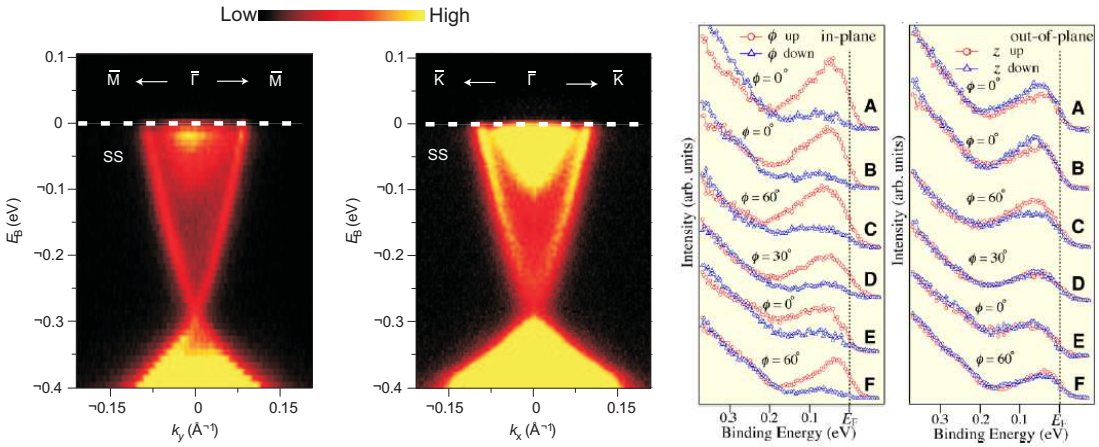

Fig. 2.5: On the left side ARPES measurements done on Bi_2Se_3 published by Xia et al. [26] are shown. Displayed is the density of states in k_y and k_x direction. The surface state, between valence and conduction band, with a nearly linear dispersion is resolved. On the right side is the result of Spin-resolved ARPES measurements by Souma et al. [28] on Bi_2Te_3 at different k-points for in-plane and out-of-plane spin direction. A strong in-plane spin-polarization, perpendicular to $\vec{k}$, is measured for the energy range of the surface state.

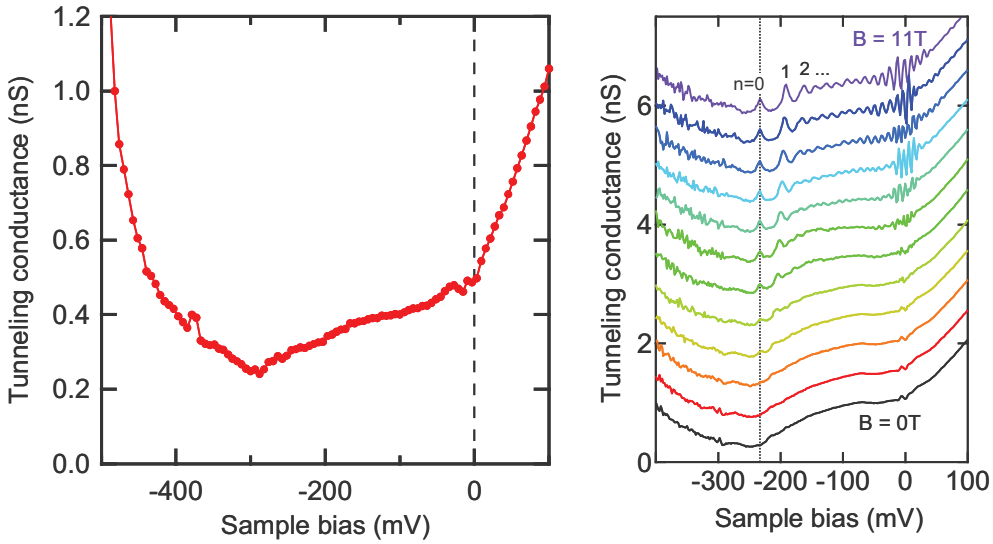

Fig. 2.6: STS measurements by Hanaguri et al. [29] on Bi_2Se_3. On the left side the tunneling spectrum showing the existence of states in the gap is displayed. The approximately linear increase of their density is reflected by the linear increase of the tunneling conductance. On the right the tunneling spectra for different magnetic fields showing the formation of Landau levels are shown. The unmoving level at $n = 0$ and the unequally spaced Landau levels are characteristics of the topologically protected surface state.

point, and only the occupied states can be measured with ARPES preventing an observation of the surface state. Later on, the spin-polarization was shown as well in spin-resolved ARPES measurements [28, 34, 35], as displayed in fig. 2.5. Therefore the Dirac-like nature of the surface state, a linear dispersion and spin polarization, is shown.
Another method to demonstrate the existence of a surface state is by scanning tunneling spectroscopy (STS). By probing the energy dependence of the local density of states at the surface with STS the existence of states in the gap with an approximately linear dispersion was measured. By applying a magnetic field, the Landau quantization of the energy levels of these states showing predicted characteristics of the topologically surface state, unequally spaced levels and an unmoving level at the Dirac-point, see fig. 2.6, was shown as well [17, 29, 36].
The existence of a Dirac-like surface state in these material therefore is proven, but to conduct reliable electrical transport experiments on it, an insulating bulk is needed as well. So far, many transport measurements showing features which could be interpreted as signs of the surface state were published. Among other, Shubnikov-de Haas oscillations [37–57], linear magnetoresistance [41, 58–67], the ambipolar field effect [60, 68], weak anti-localization [50, 59, 62, 63, 69–75] and spin-polarization [76] were reported in these materials, but always the considerable contribution of the bulk makes the interpretation of the results ambiguous.

Chapter 3

Transport Properties

Electrical transport experiments are a useful characterization method and essential for the development of new electronic devices. The exploration of the new physics offered by the TI materials can only be realized if the surface and edge states are accessible in transport, but so far, the remaining bulk conductance in Bi_2Se_3 and related compounds makes a distinct observation of the surface state in transport experiments impossible. Because of its simple band structure, the biggest band gap and the Dirac-point lying in the band gap out of the three compounds, Bi_2Se_3 was chosen as a starting point.
In the following chapter the growth of the material, the causes for imperfections in the crystal, presumably leading to the bulk conductance, and attempts to improve the crystal quality are described. Afterward results of transport measurements conducted on these samples are presented and analyzed in a one or two carrier model. The influence of an improved crystal quality on the carrier density is investigated and further attempts to reduce the carrier density by partially replacing Bi with Sb are described. The present features in the magnetoresistance, weak anti-localization (WAL), linear magnetoresistance (LMR) and Shubnikov-de Haas (SdH) oscillations are analyzed, focusing on the identification of their origin, either from the bulk or the surface state, and are compared to the literature.

3.1 Unintentional doping

The fabrication of Bi_2Se_3 and related compounds is done by molecular beam epitaxy (MBE) in an ultrahigh-vacuum (10^{-9} mbar) chamber. Bi and Sb belong to the group V elements, Se and Te belong to the group VI elements, therefore, in a simple picture, the group V element acts a as donator of three electrons and the group VI element as an acceptor of two electrons.
In principal, by MBE a high crystal quality can be achieved, but first the individual problems of the growth of the target material have to be solved. The complex crystal structure, difference in vapor pressure of the involved materials and van-der-Waals bonds between the quintuple layers make the growth of Bi_2Se_3 and related compounds difficult. These problems result in crystal imperfections leading to unintentional doping of the material and scattering centers for the carriers.

3.1.1 Possible doping effects

The most common crystal imperfections and doping effects for Bi_2Se_3 and possible methods to reduce them are described in the following. These defects can also apply to the other compounds Bi_2Te_3 and Sb_2Te_3, by replacing Se with Te and Bi with Sb in the text. They are:

- Se vacancies, V_{Se}, causing n-type doping [77–79]
- The antiside defect Bi_{Se}, where Bi occupies a Se position [80]
- Bi_2-layer intercalation between the van-der-Waals bonds [80]
- Low crystal quality at the interface to the substrate [81]
- Rotational twins, forming domains which are rotated in respect to each other by 180° [81, 82]
- Lamellar twins, meaning a change in the stacking order in growth direction [83]

Some of the mentioned defects are displayed in fig. 3.1. To reduce their amount and thereby improve crystal quality adjustments to the crystal growth have been made.

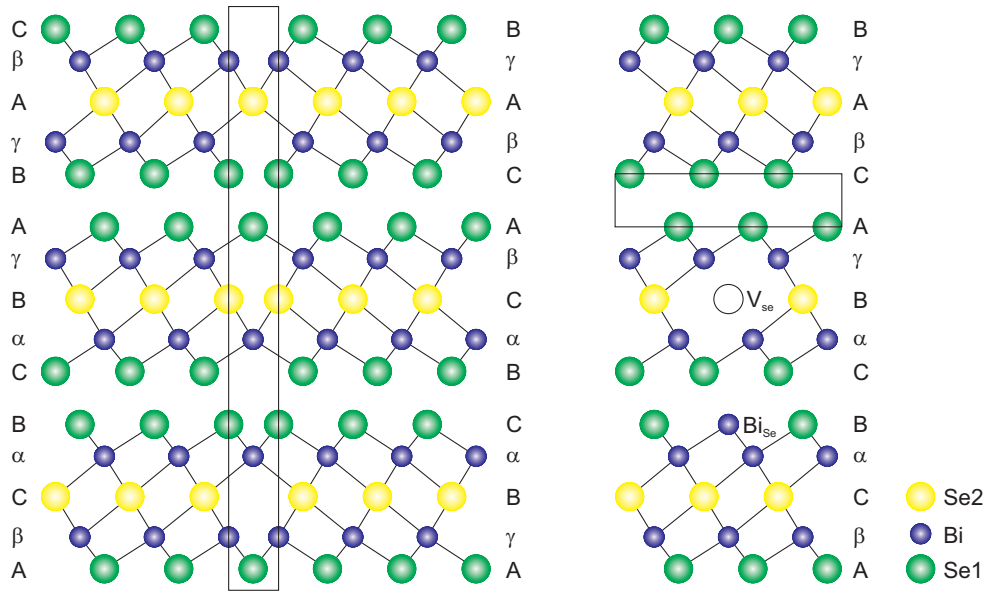

Fig. 3.1: Schematic drawing of the cross section of Bi_2Se_3 in the [100] direction. On the left side a rotational twin and on the right side a lamellar twin and additionally the defects V_{Se} and Bi_{Se} are displayed.

An easy way to decrease the formation of V_{Se}, Bi_{Se} and Bi_2-layer intercalation is to grow under high Se-flux conditions. Thus Se is always available for incorporation and the probability of defects, where Se atoms are missing or are being replaced, is diminished. Bi_2Se_3 is the Selenium richest Bi-Se compound and using a high Se flux does not lead to other defects in the growth making it a suitable method. The low crystal quality at the interface is likely a consequence of the van-der-Waals bond connecting the layer with the substrate [81]. Due to the weak bond the correct orientation is not distinctly favored in energy, and other orientations are present as well. The same reasoning applies to the formation of rotational twins. The crystal structure of the substrate is not completely conveyed to the grown layer and two possible domain orientations, rotated by 180° to each other, emerge. An enhancement of the transmission of the substrate structure is needed and this can be provided by the use of a rough substrate. Usually a substrate roughness is not wanted because it will result in a rough grown layer. But in this case the frequent steps of the substrate height, due to the roughness, can form covalent bonds with the growing layer and they as well as the steps themselves

provide a distinct crystal orientation for the growing layer. This results in a suppression of twinning and an increase of the crystal quality at the interface [84]. A downside to this approach is the formation of translational domains, because the step size of the substrate differs from the lattice constant of the grown crystal in growth direction [84].
The formation of lamellar twins is not depended on the substrate, but on the atomic interactions of the crystal and therefore can be regarded as an intrinsic crystal feature [83].
By applying these measures the crystal quality of the grown Bi_2Se_3 was improved as determined by XRD, AFM and TEM measurements [81, 83, 84].

3.2 Magnetoresistance

By measuring the magnetoresistance of materials one gains knowledge about their electrical properties. For example from the Hall resistance one can extract the carrier density, combined with the sheet resistance one can get the mobility, or when observing oscillations in the resistance one gets the Fermi area. This information is useful to determine the electrical quality of the grown crystals and to clarify its usefulness for further transport experiments looking for evidence of the topological surface state. Since the goal is to explore the behavior of the surface state the features in the magnetoresistance are analyzed in respect to their possible origins.
For proper transport measurements a defined sample geometry, enabling the measurement of the longitudinal and Hall voltage, is needed. Therefore samples of the grown layers were prepared into a Hall bar geometry by standard optical lithography. First the film is patterned, either by ion beam etching with argon or by wet etching with a brom:ethylene glycol (1:200) solution. In principle wet etching is less destructive than etching with an ion beam, but no qualitative difference is seen in the electrical transport for the measured layers. Next the metallic contacts, consisting of 50 nm AuGe, 5 nm Ti and 50 nm Au are deposited by evaporation in an ultra-high-vacuum (UHV) chamber. The first layer of AuGe is commonly used for contacting semiconductors like GaAs or InP [85], providing a low contact resistance because of the diffusion of Ge, and works for the Bi_2Se_3-layers as well. If required for the specific sample a topgate is made by growing an

insulating layer by atomic layer deposition comprised of 20 nm AlO_x and 1 nm HfO_x and forming a metal electrode of 5 nm Ti and 100 nm Au. The HfO_x-layer is necessary to protect the AlO_x which would be etched by the chemicals used for the optical lithography in the subsequent step. The insulator at the metal contacts is then removed by etching with HF:H_2O (1:200). An exemplary picture of a processed sample is shown in the optical picture of fig. 3.2, consisting of two Hall bars, a large and a small one with dimensions of 600 x 200 μm^2 (length x width) and 30 x 10 μm^2 respectively and topgates. Afterward the sample is glued into a chip carrier and the metal contacts of the sample are connected to pads of the chip carrier by ultrasonic wire bonding. The chip carrier can then be mounted into a sample stick suitable for measurements in a cryostat equipped with a superconducting magnet.

The measurements were conducted at cryogenic temperatures at $T = 4.2$ K, the temperature of liquid helium at atmospheric pressure, or lower. If not stated otherwise, the temperature was at $T = 4.2$ K. Depending on the setup, the magnetoresistance was taken by applying a dc or an ac bias voltage and measuring the voltage drop over a reference resistance, determining the current through the sample, and over the desired contacts on the sample, as exemplary displayed in the schematic part of fig. 3.2. For all layers there was no qualitatively difference between measurements on the small or large Hall bar. A distinction of measurements on the small or large Hall bar is therefore not made.

3.2.1 Reducing the carrier density and the two carrier model

The transport results on the first Bi_2Se_3-layers are dominated by bulk carriers interfering with an observation of the surface state. Therefore the carrier density has to be reduced. In the following an overview of the evolution of the transport properties, with improving crystal quality, and an analysis of the obtained data in the one and two carrier model are given.

The first Bi_2Se_3-layers in our group were grown on Si(111) and have a poor crystal quality. When monitoring the resistance with decreasing the temperature one observes an approximately linear decrease of the longitudinal resistance, until saturation at about $T = 20$ K, as for example in fig. 3.3, resembling metallic behavior. The decrease in resistance is caused by a decrease of phonon scattering

as the temperature decreases. In contrast, for an intrinsic semiconductor an exponential increase of the resistance, because of carrier freeze out, would be expected.

The Hall resistance, ρ_{xy}, shows a linear increase with the magnetic field with a slope $R_H = \Delta\rho_{xy}/\Delta B$ over the whole range and the longitudinal resistance, ρ_{xx}, changes by about 0.5%/T in an almost linear way. Additionally ρ_{xx} shows a cusp for small magnetic fields, a feature that will be discussed later. An exemplary measurement is shown in fig. 3.4.

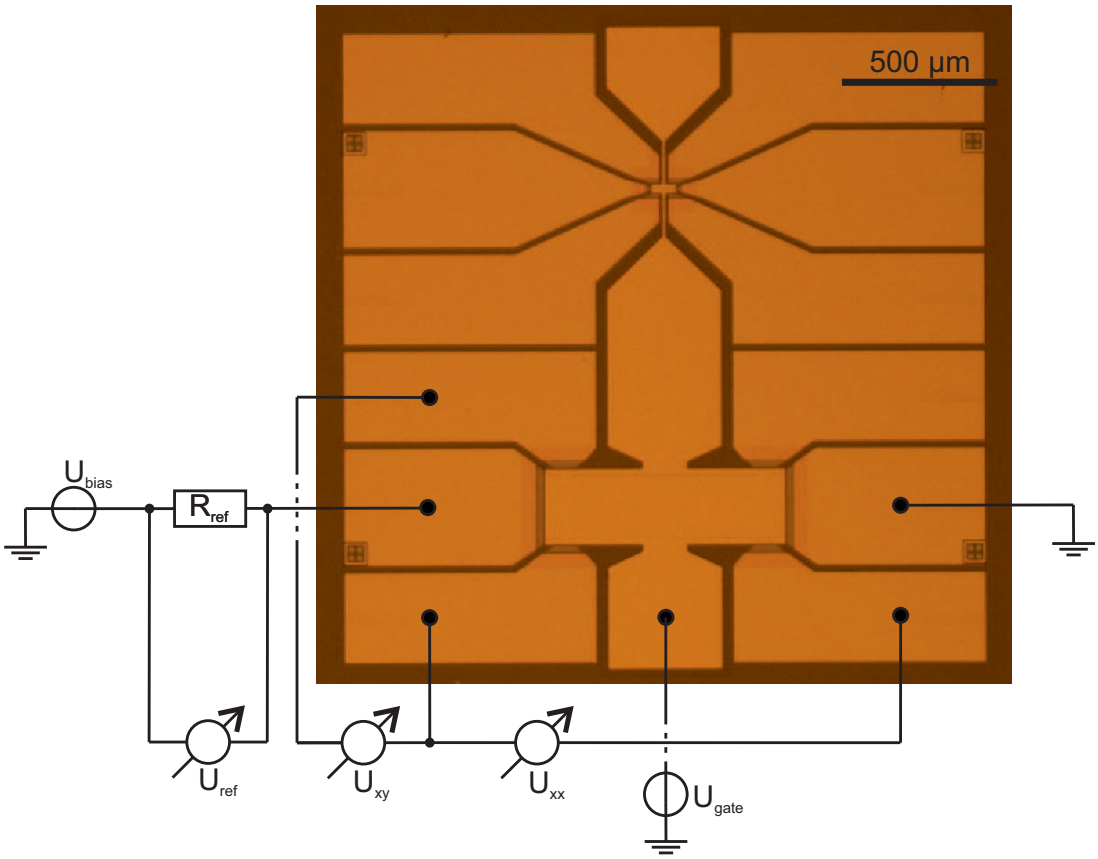

Fig. 3.2: Optical picture of an Hall bar device with a topgate fabricated by standard optical lithography and a scaling bar for reference in the upper right corner. Added is a schematic of a dc measurement circuit.

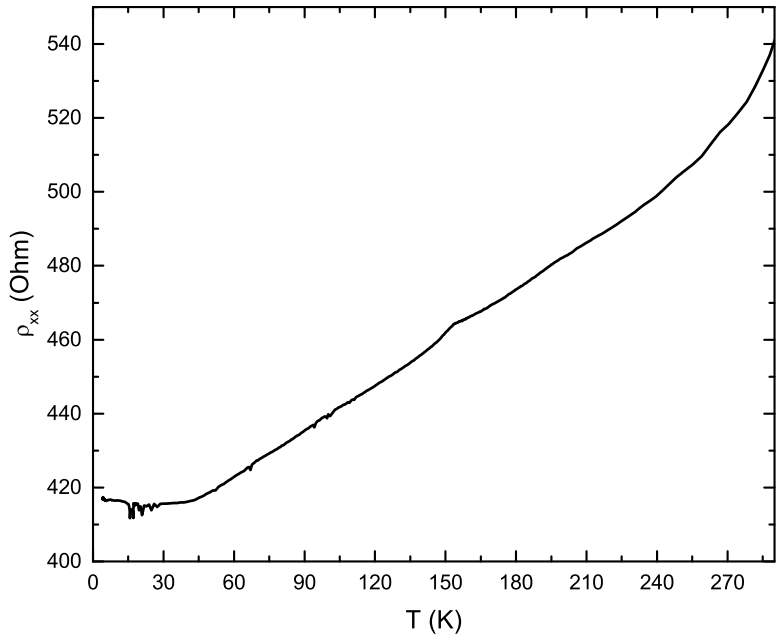

Fig. 3.3: Longitudinal resistivity of the same sample as in fig. 3.4 during cooling at $B = 0$ T.

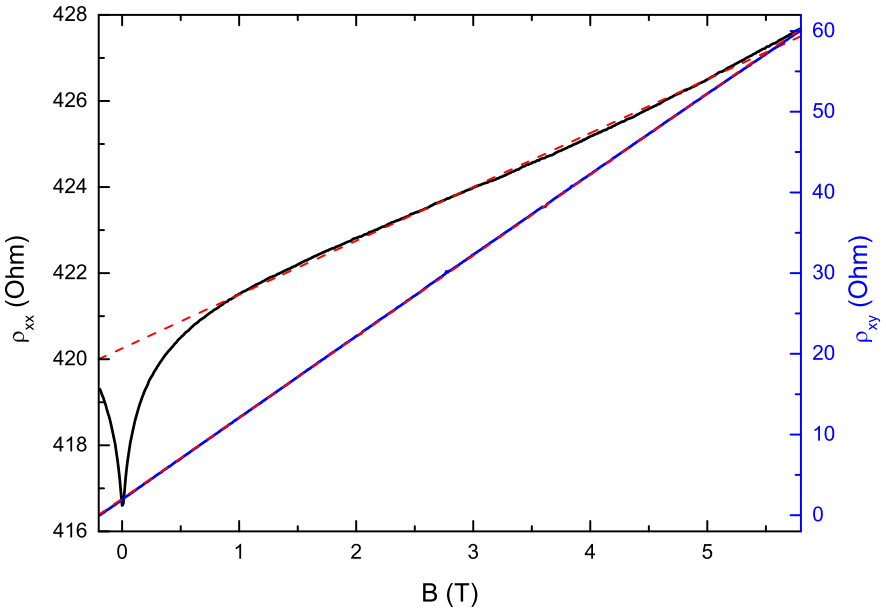

Fig. 3.4: Measurement on a Hall bar at $T = 4.2$ K showing ρ_{xx} (black) and ρ_{xy} (blue) of a Bi_2Se_3-layer grown on Si(111) with a thickness of $d = 70$ nm. The red dashed lines represent linear fits to the resistances. The Hall resistivity is linear over the whole magnetic field range and the longitudinal resistivity is nearly linear up from 1.5 T and around $B = 0$ T the longitudinal resistivity forms a cusp.

The carrier density and mobility can be calculated by:

$$n = \frac{1}{q \cdot R_H \cdot d} , \tag{3.1}$$

$$\mu = \frac{1}{q \cdot n \cdot \rho_{xx}} , \tag{3.2}$$

with the charge q of the carriers and the film thickness d. The carrier density for these samples is around $1 \cdot 10^{19}$ cm^{-3}, n-type, and the resulting mobilities lie around 200 cm^2/Vs to 400 cm^2/Vs. With thicknesses of around 100 nm the 2D density would be of the order of 10^{14} cm^{-2}, too large for a surface state, see for example section 2.1.4. Overall the transport behavior is similar to a highly doped semiconductor. The goal is to improve the crystal quality to lower the densities and get higher mobilities.
An increase in crystal quality was achieved and shown in publications from our group [81, 84]. By switching the substrate from Si(111) to InP(111), the lattice-mismatch of substrate to layer is decreased from 7.8 % to 0.16 %, reducing the strain in the grown crystal and resulting in a decrease of the full width at half maximum (FWHM) of the rocking curve to $\Delta\omega \approx 13$arc sec [81]. The twinning was then suppressed by the use of a rough InP(111) substrate to effectively transmit the 3D substrate structure to the Bi_2Se_3-layer [84]. Samples with different thicknesses were grown and the Hall resistance deviates from a linear behavior, thus at least two type of carriers significantly contribute to the conductivity of the material. This goes along with a significant increase in the longitudinal magnetoresistance, up to 10%/T for some samples. The conductivities, σ_i, of the individual carrier types add up and in a magnetic field and the longitudinal, σ_{xx}, and transversal, σ_{xy}, conductivities following from the Boltzmann kinetic equation are given by

$$\sigma_{xx} = \sum_{i=1}^{j} \sigma_{0,i} \frac{1}{1 + (\mu_i B)^2} , \tag{3.3}$$

$$\sigma_{xy} = \sum_{i=1}^{j} \sigma_{0,i} \frac{\mu_i B}{1 + (\mu_i B)^2} , \tag{3.4}$$

$$\sigma_{0,i} = q_i n_i \mu_i , \tag{3.5}$$

with the amount of individual carriers j, $q = -e$ for electrons and $q = +e$ for holes. The resistivity, the quantity measured in the experiment, is gained by inversion of the conductivity matrix. For the assumption of two types of carriers, $j = 2$, the result is:

$$\begin{aligned}\rho_{xx} &= \frac{\sigma_{xx}}{\sigma_{xx}^2 + \sigma_{xy}^2} = \\ &= \frac{q_1 n_1 \mu_1 \left(1 + B^2\mu_2^2\right) + q_2 n_2 \mu_2 \left(1 + B^2\mu_1^2\right)}{(q_1 n_1 \mu_1 + q_2 n_2 \mu_2)^2 + B^2 \mu_1^2 \mu_2^2 (q_1 n_1 + q_2 n_2)^2} \ , \qquad (3.6) \\ \rho_{xy} &= \frac{\sigma_{xy}}{\sigma_{xx}^2 + \sigma_{xy}^2} = \\ &= \frac{q_1 n_1 \mu_1^2 \left(1 + B^2\mu_2^2\right) + q_2 n_2 \mu_2^2 \left(1 + B^2\mu_1^2\right)}{(q_1 n_1 \mu_1 + q_2 n_2 \mu_2)^2 + B^2 \mu_1^2 \mu_2^2 (q_1 n_1 + q_2 n_2)^2} \cdot B \ . \qquad (3.7)\end{aligned}$$

A fit, using eq. 3.6 and 3.7 for a sample grown on InP(111), being in good agreement with the data, as previously disregarding the cusp near $B = 0$, is shown in fig. 3.5.

d (nm)	$V_g(V)$	$n_1(cm^{-3})$	$n_1(cm^{-2})$	$n_2(cm^{-3})$	$n_2(cm^{-2})$	$\mu_1(\frac{cm^2}{Vs})$	$\mu_2(\frac{cm^2}{Vs})$
20	0	$1.60 \cdot 10^{19}$	$3.20 \cdot 10^{13}$	$7.78 \cdot 10^{18}$	$1.56 \cdot 10^{13}$	231	933
50	0	$6.60 \cdot 10^{18}$	$3.30 \cdot 10^{13}$	$2.20 \cdot 10^{18}$	$1.10 \cdot 10^{13}$	311	1560
50	-5	$5.67 \cdot 10^{18}$	$2.84 \cdot 10^{13}$	$2.04 \cdot 10^{18}$	$1.02 \cdot 10^{13}$	316	1550
50	-10	$5.29 \cdot 10^{18}$	$2.64 \cdot 10^{13}$	$2.00 \cdot 10^{18}$	$9.99 \cdot 10^{12}$	309	1530
190	0	$1.85 \cdot 10^{18}$	$3.52 \cdot 10^{13}$	$6.11 \cdot 10^{17}$	$1.16 \cdot 10^{13}$	354	3070
290	0	$1.02 \cdot 10^{18}$	$2.95 \cdot 10^{13}$	$1.07 \cdot 10^{18}$	$3.11 \cdot 10^{13}$	411	3640

Table 3.1: Parameters used for the fit in fig. 3.5 and fig. 3.6 and other samples with the same growth configurations but different thicknesses according to the two carrier model.

The values obtained for Bi_2Se_3 samples on rough InP(111) with different layer thicknesses are listed in tab. 3.1. The total carrier density is in the range of 10^{19} cm^{-3} to 10^{18} cm^{-3}, with a minority carrier type having values down to 10^{17} cm^{-3}. The mobility for the majority type is about 200 cm^2/Vs to 400 cm^2/Vs and for the minority the values are between 1000 cm^2/Vs and 4000 cm^2/Vs. An improvement for the density by about a factor of 10 compared to layers on Si(111). Interestingly both 3D n_1 and n_2 decrease with increasing the thickness of the sample and are roughly constant in the 2D case, but

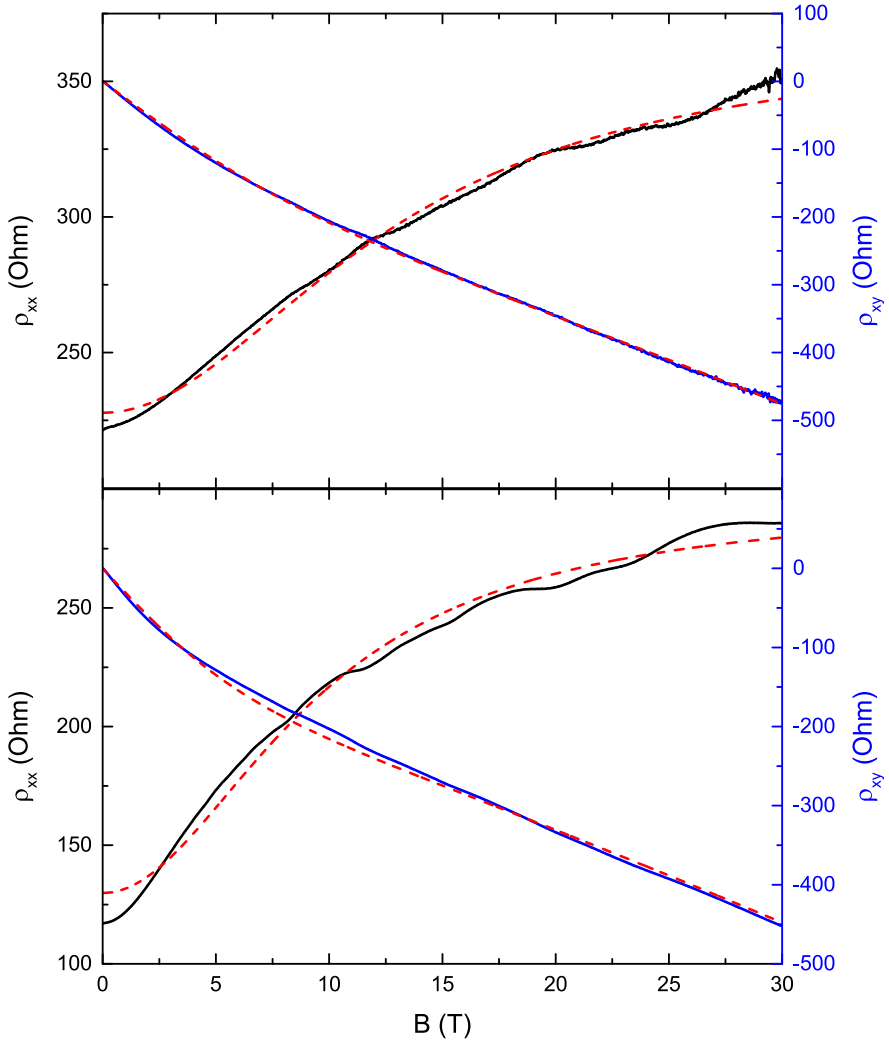

Fig. 3.5: Measurements on Hall bars at $T = 4.2K$ showing the longitudinal (black) and Hall (blue) resistivity of Bi_2Se_3-layers grown on rough InP(111) with a thickness of $d = 50$ nm (top) and $d = 190$ nm (bottom). The red dashed lines represent the fits according to the eqs. 3.6 and 3.7. The fit parameters are listed in tab. 3.1. For both layers oscillations in the resistance with a small amplitude are visible at high magnetic fields.

especially n_1 is actually too high to originate from the surface state, see section 2.1.4. This might point to a relation of the carrier density to the interface of the layer which is in all cases the same. Additionally, there are now oscillations present in the resistance at high magnetic fields, which will be discussed later. The question now arises if the minority carrier type with the higher mobility and lower density could originate from the surface state.

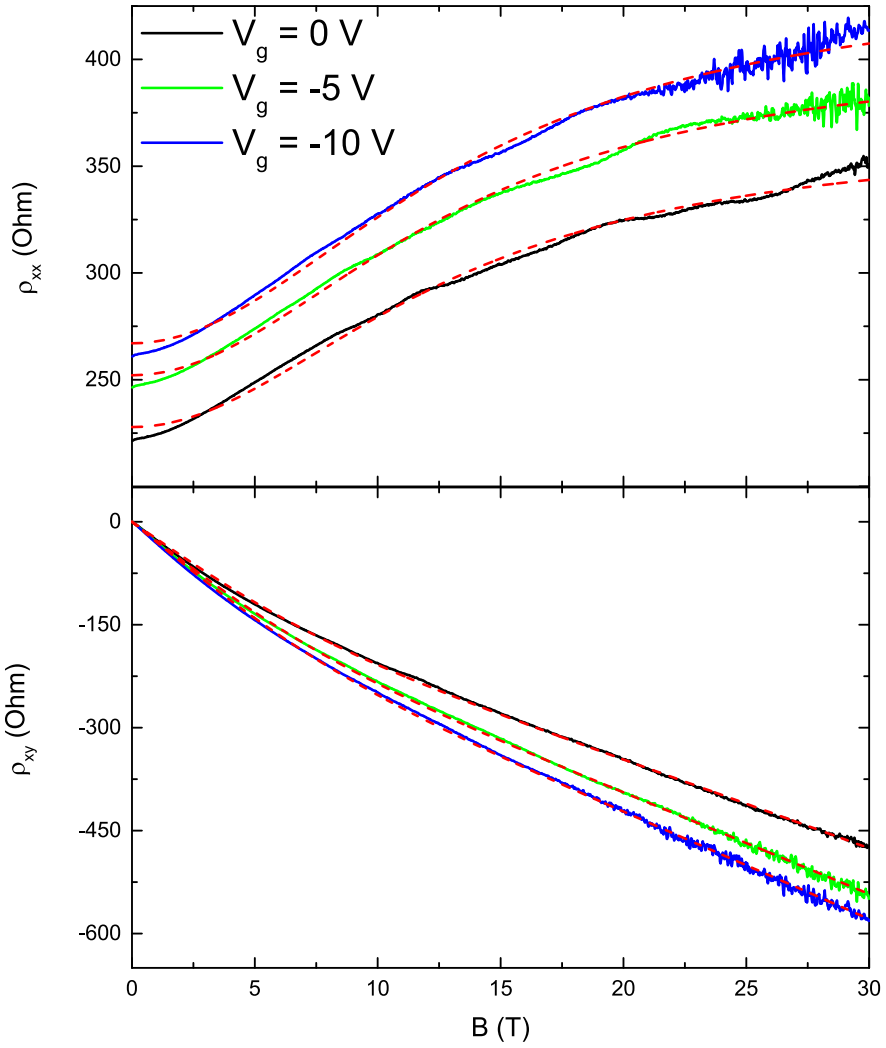

Fig. 3.6: Measurements on the same Bi_2Se_3-layer already shown in the top of fig. 3.5 at $T = 4.2$ K for different topgate voltages V_g showing the longitudinal (top) and Hall (bottom) resistivity. The red dashed lines represent the fits according to the eqs. 3.6 and 3.7.

To further analyze the two carrier types a topgate was introduced to the structure. By applying a negative voltage to the gate the n-type carrier density

can be lowered. A measurement for different gate voltages and the resulting fit parameters are shown in fig. 3.6 and tab. 3.1 respectively. As can be seen, both carrier types decrease at changing to more negative gate voltages, with the relative change being less for the minority type than for the majority type. If the minority carrier type is indeed the surface state, a screening effect could be expected, where the bulk carriers, that would be the majority carrier type, are at least partially shielded from the potential change of the gate by the surface state in proximity to the gate. This is not the case, on the contrary the majority type of carrier changes more by applying a gate voltage.
In several publications on Bi_2Se_3 and alike materials deviations of the Hall resistance from linearity are observed as well. Two and even three carrier models are used to describe the nonlinear behavior of the Hall resistance and the origin of the different carrier types is attributed to the bulk and surface [41, 43, 50], the bulk and two surfaces [55], or the bulk, the surface and an impurity band [52, 86]. The justification for these classification is given by oscillations observed in the resistance from which a carrier concentration is extracted and matched to one of the carrier types. But with four or even six unknown variables for the multiple carrier model and a fit only performed to the Hall component of the resistance and the zero field longitudinal resistance, this approach is not unambiguous. Additionally the oscillations are only small in amplitude increasing the error in the analysis further.

3.2.2 Reducing the carrier density further by alloying

To lower the carrier density Bi was partially replaced with Sb. In contrast to Bi_2Se_3 and Bi_2Te_3, Sb_2Se_3 and Sb_2Te_3 are known to be p-type and therefore it is expected that at least to some extent, the p-type doping cancels out the n-type doping of pure Bi_2Se_3, resulting in less free carriers [87–90].
Therefore several $(Bi_{1-x}Sb_x)_2Se_3$-layers with increasing Sb content x were grown and measured in transport. All samples were grown, like the previous ones, on rough InP(111) with layer thicknesses around 150 nm. Since pure Sb_2Se_3 has a different crystal structure, orthorhombic instead of rhombohedral [43], and is not predicted to be a topological insulator [14], the value of x is limited. All samples show signs of two carrier transport and indeed, by increasing x, a decrease in car-

rier concentration was observed until reaching a minimum of the carrier density for $x = 0.44$, see fig. 3.7, still being in the rhombohedral regime.

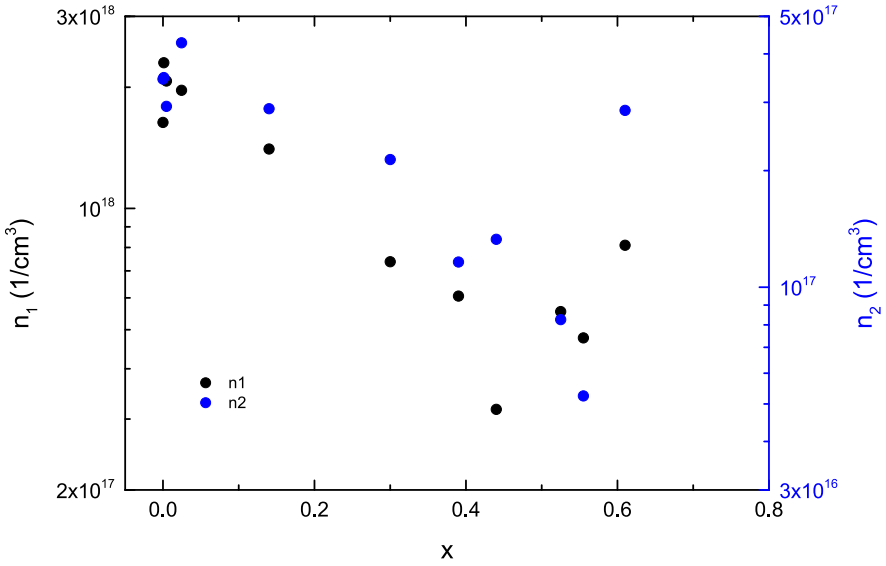

Fig. 3.7: The two types of carrier densities for different Sb-content x. The value of x has been determined by EDX-measurements. The fit parameters of the used two carrier model are in tab. A.1 in the appendix.

The carrier density is reduced in these samples down to a total carrier density of about $n = 4.5 \cdot 10^{17}$ cm^{-3} but still not enough to make the bulk insulating. By gating the sample the carrier density can be further reduced, and to make efficient gating possible, a thinner sample with $d = 50$ nm at $x = 0.44$ was grown and measured. The influence of the gate is shown in fig. 3.8. In accordance to the lower carrier density the influence of the gate is bigger than for a pure Bi_2Se_3-sample, compare for example to fig. 3.6.

By taking a closer look on the change of $\rho_{xy}(B)$ upon changing the gate voltage in fig. 3.9, it can be concluded, that the high mobility carrier transits from n-type to p-type by gating, assuming the mobilities of the two carrier types do not change dramatically. This can be seen by the slope of ρ_{xy} in fig. 3.9 upon changing the magnetic field, going from bending upwards (black and green) to bending downwards (cyan, dark yellow and navy). The dependency on the magnetic field of ρ_{xy} can be fitted with the two carrier model, but ρ_{xx} cannot. Even for the gate voltage which results in an almost linear slope of ρ_{xy}, meaning that there is only one dominant carrier type and the magnetoresistance of ρ_{xx} should be constant, ρ_{xx} still shows a considerable change with magnetic field. There are

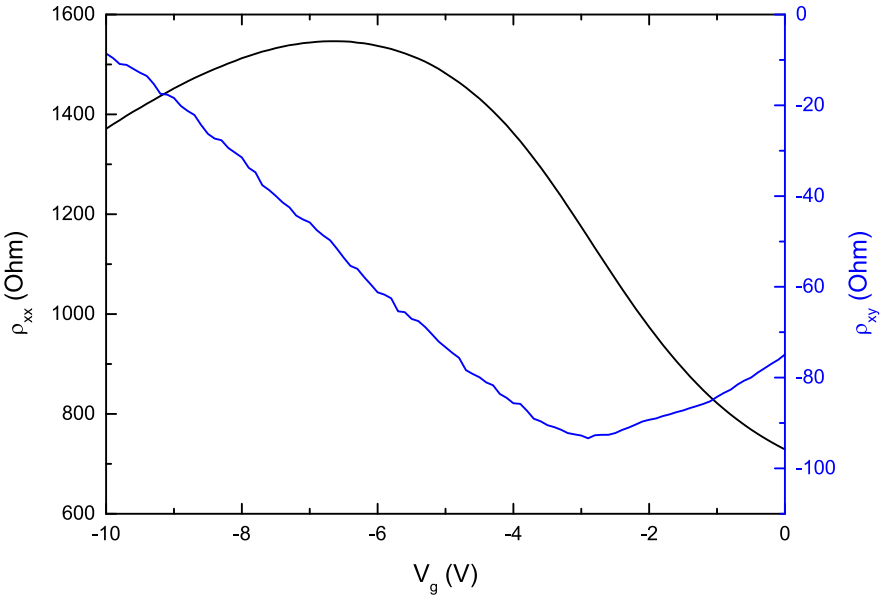

Fig. 3.8: Dependence of ρ_{xx} (black) and ρ_{xy} (blue) on the topgate voltage V_g at $B = 1$ T and $T = 4.2$ K of a 50 nm layer $(Bi_{0.56}Sb_{0.44})_2Se_3$.

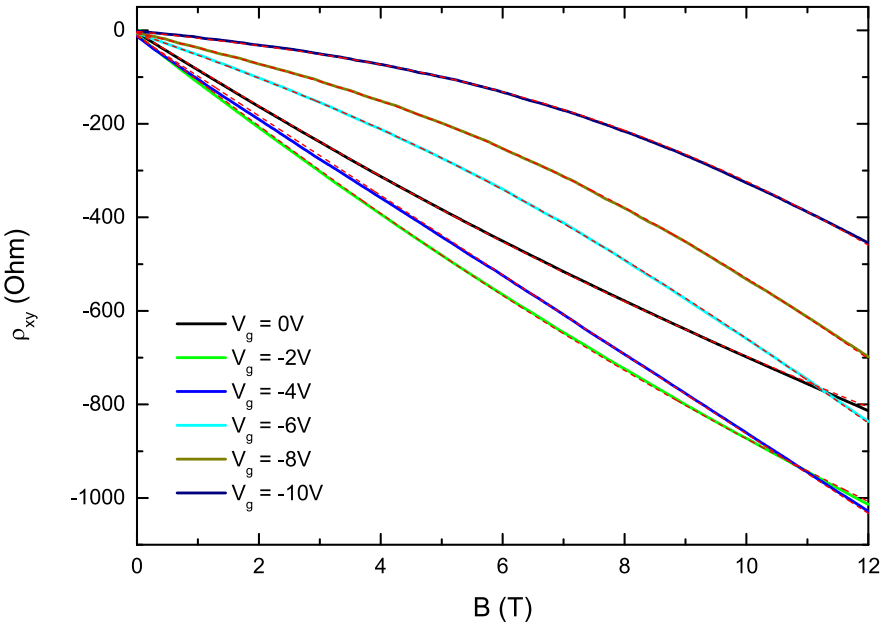

Fig. 3.9: Measurement of the Hall resistance for different gate voltages as indicated in the legend at $T = 4.2$ K. Upon lowering the gate voltage the bending of $\rho_{xy}(B)$ changes from upwards to downwards with $\rho_{xy}(B)$ at $V_g = -4$ V being linear with magnetic field.

additional contributions to the magnetoresistance not covered by a two carrier model, either additional carrier types or other effects not covered by Boltzmann

transport theory. Because of this insufficiency of the two carrier model, the parameters extracted from the fit by only focusing on ρ_{xy}, shown in fig. 3.10 come with an error.

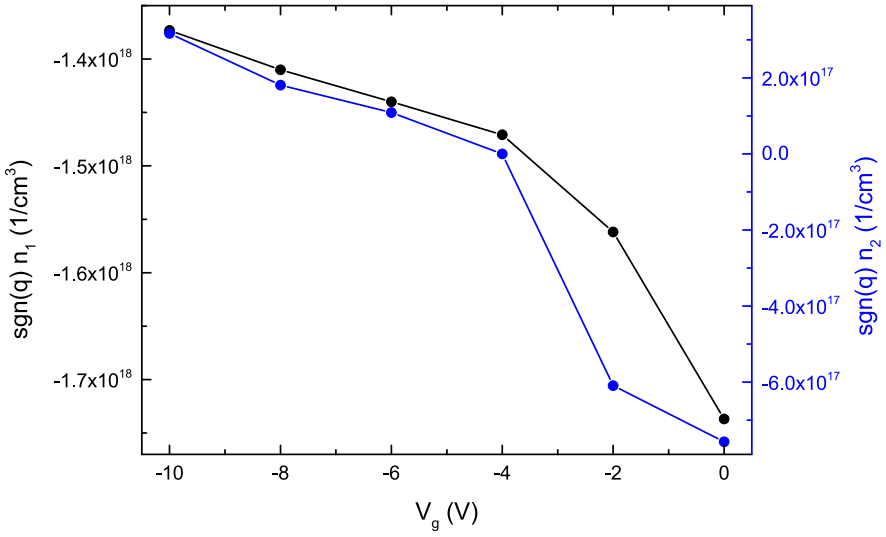

Fig. 3.10: The majority, n_1 (black), and minority, n_2 (blue), carrier concentration, extracted by a two carrier fit to ρ_{xy}, in dependence of the topgate voltage V_g is shown.

Even though the carrier density is reduced in this sample and one carrier type actually transits from n-type to p-type by gating, no additional features in the magnetoresistance were found which would indicate transport from the topological surface state.

The temperature dependence of ρ_{xx}, shown in fig. 3.11 of this sample, even though the carrier density has been reduced, still resembles the qualitative behavior for samples grown on Si(111), as shown in fig. 3.3. The decrease in resistance still is like metallic behavior and no sign of carrier freeze out is seen.

Another attempt to reduce the carrier density was the growth of $Bi_2Te_{3-x}Se_x$. This compound in principle could share the positive features of Bi_2Se_3 and Bi_2Te_3, a large band gap with a simple band structure while at the same time being less sensitive to vacancies [43, 91]. For electrical transport the theoretically ideal composition would be $Bi_2Te_2Se_1$ with an ordered layer structure for each quintuple layer: Te-Bi-Se-Bi-Te [92]. In practice no significant decrease of the carrier density was found with varying x and it was shown that the ideal ordered structure at best makes up 75% of the grown crystal [93].

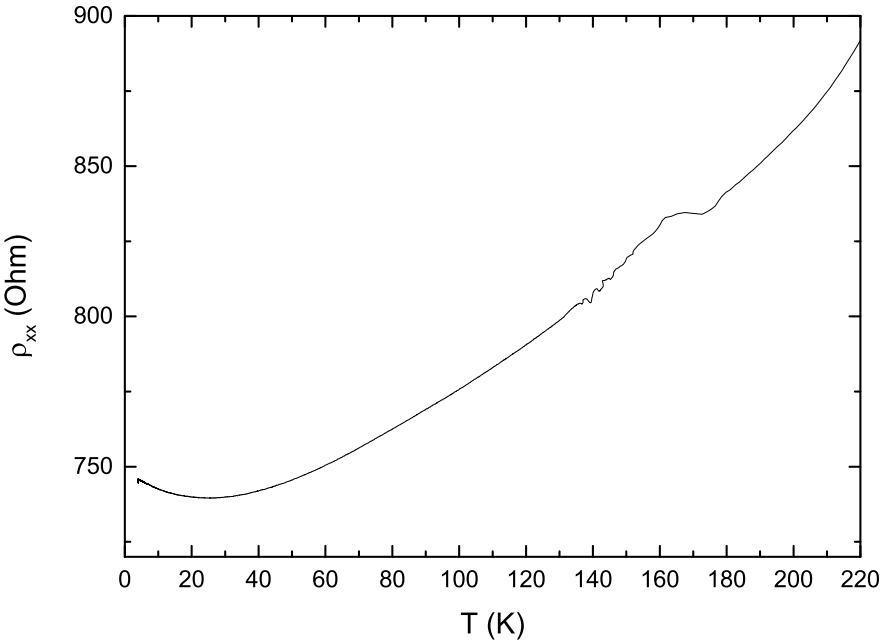

Fig. 3.11: Longitudinal resistivity of the 50 nm layer $(Bi_{0.56}Sb_{0.44})_2Se_3$ during cooling at $B = 0$ T.

3.2.3 Linear magnetoresistance

The longitudinal magnetoresistance of some samples with high Sb content or samples grown on flat InP(111) substrate deviates from the behavior predicted by the two carrier model. The two carrier model underestimates the magnitude of the magnetoresistance and when the magnetic field is high enough that the conditions $\mu_1 B > 1$ and $\mu_2 B > 1$ are fulfilled, the two carrier model predicts a saturation of the longitudinal magnetoresistance, but the resistance in these samples continues to rise in a linear way. This can be seen exemplary in fig. 3.12. An additional linear contribution, $\Delta\rho_{xx} = \beta_{LMR} \cdot |B|$, is needed to fit the experimental data.

$n_1(cm^{-3})$	$n_2(cm^{-3})$	$\mu_1(\frac{cm^2}{Vs})$	$\mu_2(\frac{cm^2}{Vs})$	$\beta_{LMR}(Ohm/T)$
$8.4 \cdot 10^{17}$	$3.4 \cdot 10^{17}$	570	2500	0
$8.3 \cdot 10^{17}$	$3.0 \cdot 10^{17}$	660	2800	11

Table 3.2: Parameters used for the fit in fig. 3.12 according to the two carrier model with and without the addition of a LMR.

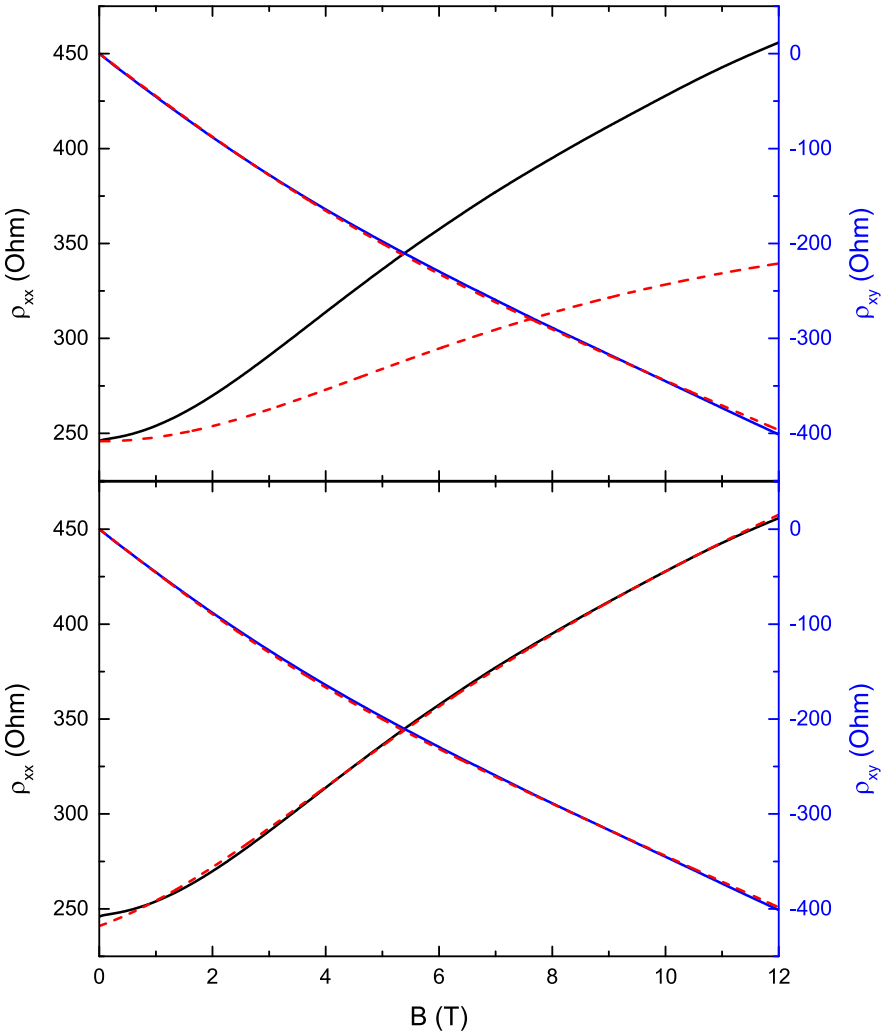

Fig. 3.12: Measurements on a Hall bar at $T = 4.2$ K showing the longitudinal (black) and Hall resistivity (blue) of a $(Bi_{0.39}Sb_{0.61})_2Se_3$-layer. In the top graph the red dashed lines represent the fits according to the two carrier model in and in the bottom one to the two carrier model with the addition of a LMR. The fitparameters are listed in tab. 3.2

There are several explanations for such a non-saturating linear magnetoresistance (LMR) in literature:

- The magnetoresistance in the extreme quantum limit, where only the lowest Landau level is occupied, which means $n < \frac{eB}{\hbar}$ for 2D and $n < \left(\frac{eB}{\hbar}\right)^{3/2}$ for 3D, was calculated to be linear by Abrikosov [94, 95]. But, since the carrier densities in these samples are high, to reach this limit a magnetic field of $B > 66$ T or $B > 7$ T, for the 2D and 3D case respectively, would be necessary. The observed linear behavior starts already at lower magnetic values, around $B = 1$ T, therefore this explanation does not apply.

- Kapitza's LMR [96] is only present in metals with open Fermi surfaces and large Fermi areas, which means large carrier densities, and is does not apply to our material.

- In the inhomogeneous semiconductor AgSe a strong LMR was observed as well [97, 98]. It can be explained by assuming different resistivities for different areas of the sample because of its inhomogeneity, as shown by simulations of a 2D random network model [99–101]. This could also apply to the grown Bi_2Se_3-layers and $(Bi_{1-x}Sb_x)_2Se_3$-layers, which with their domain structure and the grain boundaries in between can be viewed as inhomogeneous. Especially when increasing the inhomogeneity by mixing of Bi and Sb or growing on flat InP(111)-substrate.

- Recently there has been a proposal that LMR originates from the topological surface state with a linear dispersion [102]. In this proposal a high positive effective g-factor is assumed. This leads to a large Zeeman-splitting of the Landau levels which overlap at $B = 0$. The numerical results in the paper, where the authors assume a density and mobility of the surface state comparable to the values in our samples and a g-factor of $g = 10$, lead to a magnetoresistance of about 1%/T. This considers the surface state as the only conduction channel. An additional bulk conduction channel would reduce the predicted magnetoresistance further and still 1%/T is less LMR than observed in our layers.

From the mentioned explanations only the last two, LMR due to inhomogeneity or LMR due to the surface state, can be considered as realistic. While the

inhomogeneity model is already established for other materials and the measured layers could certainly be considered as inhomogeneous, the explanation relying on the surface state contains the unproven assumption of high positive g-factor, neglects the influence of bulk conductance and its numerical results give an estimate which is still too low. Therefore the existence of LMR due to inhomogeneities is considered as most likely.

The phenomenon of a non-saturating LMR in Bi_2Se_3 and alike materials has also been the subject of several publications in literature [41, 58–67] but the given explanations vary. Most studies attribute the LMR to the surface state following the explanation of the quantum limit or the linear dispersion of the surface state [58, 60–62], but it is also attributed to a reduction of bulk carriers with magnetic field [41], to a variation of the weak-antilocalization model for the surface state extending up to magnetic fields larger than 10 T [63, 65] or to the random network model [64, 66]. Especially the experiment done by Wang [66], where LMR was shown in synthesized interconnected Bi_2Te_3 nanoplates demonstrates that a high quality film is not needed to achieve LMR, rather an obvious random network of resistors already shows LMR. While not excluding other sources for the LMR, this raises doubts regarding the explanations involving the topological surface state.

3.2.4 Localization effects

At low magnetic fields, localization effects are observable in the longitudinal mangetoresistance of some layers, the already mentioned cusp around $B = 0$ (e.g. fig. 3.4). Localization is a consequence of the interference of an electron with its time reversal path, a quantum effect.
If one imagines a closed loop, an electron can travel around this loop in a clockwise or counter-clockwise manner. Because of the existence of time-reversal-symmetry, both paths acquire the same phase, which leads to a positive interference at the origin of the loop. This effectively means an increase in the probability of backscattering and therefore an increase in resistance, an effect called weak localization (WL). By applying a magnetic field the time-reversal symmetry is broken and the effect diminishes. The magnetic field leads to a decrease in resistance.
The effect, which is observed in Bi_2Se_3-samples, goes in the opposite direction,

the resistance increases by applying a magnetic field, and is called weak anti-localization (WAL). Because of the present strong spin-orbit coupling the spin of the electron is no longer conserved around the closed loop. Every time the momentum changes, the spin changes as well. For the clockwise and counter-clockwise path the momentum changes are opposite and as a result the spin change is opposite as well. Averaging over all possible scattering paths for a closed loop then leads to a negative interference, considering the fact that the spin of an electron only recovers its original state at a rotation of 4π. This is reflected in a decrease in back-scattering and consequently a decrease in resistance. Now the magnetic field destroys the negative interference and the resistance increases, as it is observed in Bi_2Se_3.

Localization effects are only noticeable if the probability of an electron returning to its origin is not negligible. Therefore they are more pronounced in systems with reduced dimensionality, like 2-DEGs. A possible origin of the WAL in Bi_2Se_3 would hence be the surface state, being a 2-DEG. Alternatively, since it is only observed in thin layers, it might also be the case that these layers are thin enough to be effectively 2D. The thickness of the sample is then smaller than the dephasing length, $d << l_\varphi$, which means that the electrons can see the surface of the layer before they loose their phase information, making the bulk a possible origin of the WAL as well.

In a magnetic field parallel to the surface, WAL is observable as well. Since a strict 2-DEG would not show localization effects in this case, the surface state, if it is the origin, has to be extended into the bulk or the bulk itself is the origin. Several studies do indeed report a finite thickness of the surface state around 3 nm [22, 103, 104].

The effect of localization on the conductivity in a magnetic field perpendicular ($\perp$) and a parallel ($\parallel$) to the surface, $\Delta\sigma_{xx}(B) = \sigma_{xx}(B) - \sigma_{xx}(0)$ were derived [105–107]:

$$\Delta\sigma_{xx}(B) = -\alpha\frac{e^2}{\pi h}\left[\ln\frac{\mathcal{B}_\perp}{B} - \psi\left(\frac{1}{2}+\frac{\mathcal{B}_\perp}{B}\right)\right], \quad \mathcal{B}_\perp = \frac{\hbar}{2e\,\ell_{tr}\ell_\varphi}, \tag{3.8}$$

$$\Delta\sigma_{xx}(B) = \alpha\frac{e^2}{\pi h}\ln\left(1+\frac{B^2}{\mathcal{B}_\parallel^2}\right), \quad \mathcal{B}_\parallel = 2\sqrt{\frac{\hbar}{e}\frac{\mathcal{B}_\perp}{\lambda^2}} = \mathcal{B}_\perp\frac{\sqrt{8\ell_{tr}\ell_\varphi}}{\lambda}, \tag{3.9}$$

where α is a constant with α = -0.5 for WAL, l_φ is the dephasing length, l_{tr} is the transport mean free path and λ is the effective thickness of the probed state either being related to the penetration length of the surface state into the bulk, independent of the thickness of the layer, or to the thickness of the layer.
In order to maintain the 2D character, λ has to be smaller than the magnetic length, $\lambda << l_H$, where $l_H = \sqrt{\frac{\hbar}{2eB}}$ is the length scale after which a difference of the phase factor of 2π is acquired. Otherwise the WAL is not constraint by the finite length λ, making the system effectively 3D again. The magnetic length already is lower than 50 nm, a typical value for the layer thickness, for a magnetic field higher than 130 mT. This makes the model inaccurate if the WAL originates from the bulk.
The localization effect vanishes when the phase difference acquired due to the magnetic field after completing a full loop is already of the order of 2π, this means when l_H is, for the perpendicular case, smaller than the dephasing length, l_H ¡ l_φ, and for the parallel case smaller than the dephasing length and the thickness, l_H ¡ $\sqrt{dl_\varphi}$.
With eqs. 3.8 and 3.9 the features in the longitudinal resistance are fitted and the parameters are extracted. The results are displayed in fig. 3.13 and tab. 3.3 and are in reasonable agreement to the experiment, with the WAL of thinner layers being better described.

Thickness (nm)	$\mathcal{B}_\perp$ (mT)	λ (nm)
15	7.1	10
30	2.8	11
50	1.6	15
70	2.4	17
120	1.1	29

Table 3.3: Parameters used for the fit of the WAL in fig.3.13.

The parameter $\mathcal{B}_\perp$ is in the range of a few mT and therefore $l_\varphi l_{tr}$ is of the order of 10^6 nm^2. Since the dephasing length l_φ should be bigger than the mean free path l_{tr}, l_φ is at least of the order of 10^3 nm, fulfilling the condition $d << l_\varphi$. The assumption that the bulk can be viewed as 2D in regard to the dephasing length is valid.
The obtained parameter λ neither matches to the penetration length of the surface

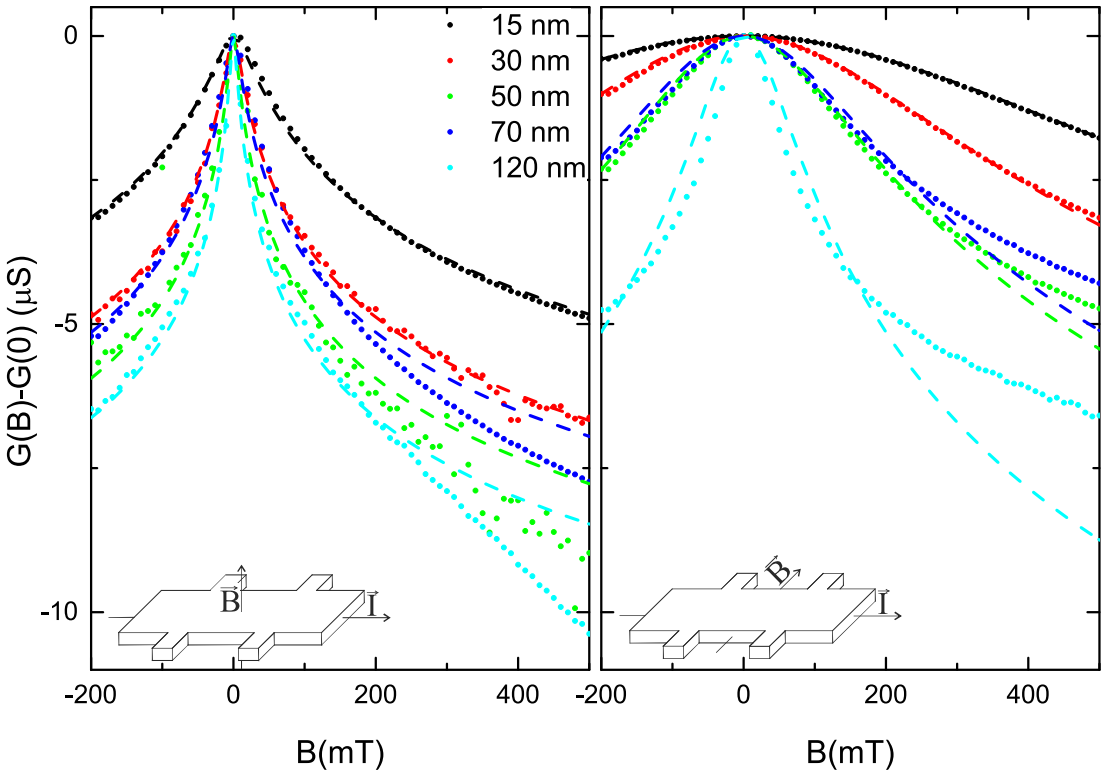

Fig. 3.13: The measured (dots) and fitted (dashed lines) WAL for Bi_2Se_3 grown on Si(111) with various thicknesses. The orientation of the magnetic field and the current is indicated in the schematics and the fit parameters are listed in tab. 3.3.

state stated in literature, being around 3 nm [103, 104, 108], nor to the actual thickness of the layer. It ranges from about 2/3 to 1/4 of the layer thickness and increases with layer thickness, making the surface state as the origin unlikely, where no dependence on the actual layer thickness is expected. Even by adding an additional term linear in magnetic field to the conductivity to adjust for other contributions using either the penetration depth of the surface state or the actual layer thickness results in an inaccurate fit, as displayed exemplary in fig. 3.14.

Thickness (nm)	$\mathcal{B}_\perp$ (mT)	λ (nm)	$\beta_\perp$ ($\mu S/T$)	$\beta_\parallel$ ($\mu S/T$)
70	3.4	3	3.7	8.5
70	2.4	70	6.4	0.1

Table 3.4: Parameters used for the fit of the WAL in fig.3.14.

If the bulk is the origin for the WAL the deviations in the fit and the discrepancy of the obtained effective thicknesses from the parallel magnetic field case compared to the actual layer thickness might be explained by the fact that the

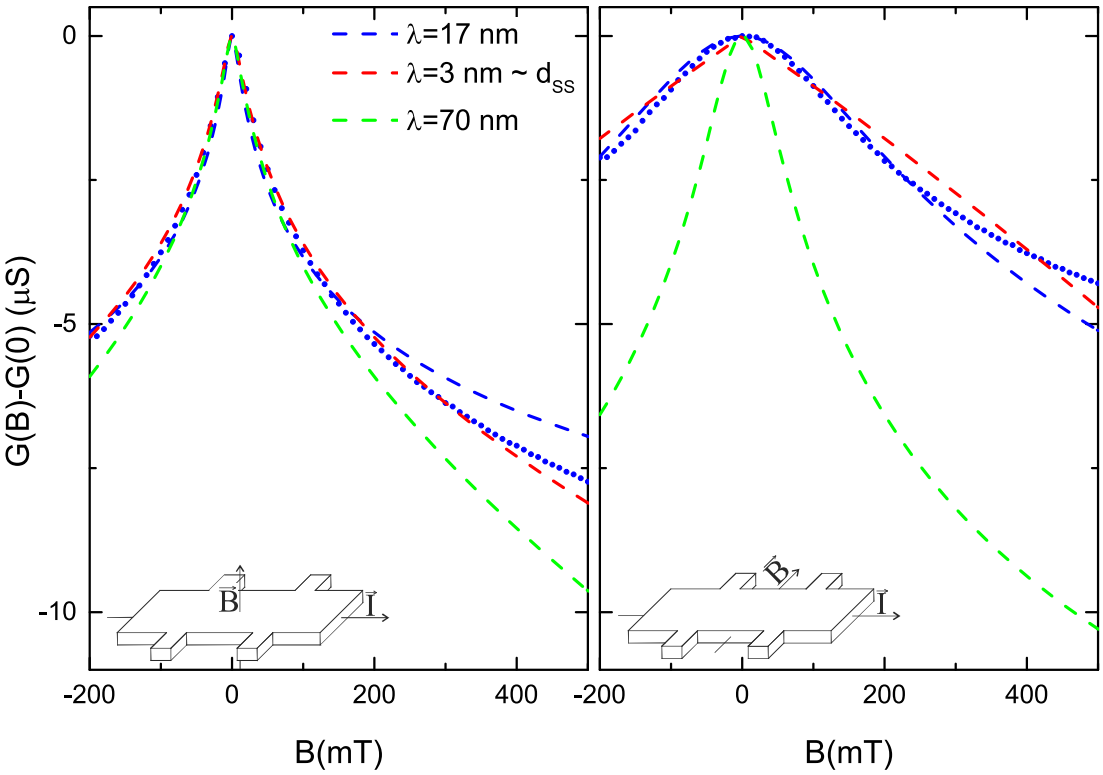

Fig. 3.14: The measured (dots) and with different parameters λ fitted (dashed lines) WAL for Bi_2Se_3, grown on Si(111) with a thickness of 70 nm. The orientation of the magnetic field and the current is indicated in the schematics and the fit parameters are listed in tab. 3.4.

stated conditions $d << l_\varphi$, for thicker samples, and especially $d << l_H$ are not entirely met.

Following this reasoning it is concluded that the surface state is not the origin of the WAL. It is rather likely explained by the bulk state which is restricted to 2D behavior at 0 field and deviates from this behavior for higher fields.

Another possibility would be that both the bulk and the topological surface state contribute to the WAL, but this is not considered in the analysis because of too many unknown variables in this model.

There are many published observations of WAL in Bi_2Se_3 [50, 59, 62, 69–73] and Bi_2Te_3 [63, 74, 75] in literature as well. The likely origin of the WAL is assigned to the surface state [50, 62, 63, 69, 74, 75] or to a mixing of bulk and surface states [59, 70–72], but it is also noted that the bulk alone could show WAL as an effectively 2D system [73]. In a publication by Kim [71] the WAL in

Bi_2Se_3 is studied for film thicknesses ranging from 3 nm to 170 μm. An obvious contribution to the resistance is seen up to a thickness of 100 nm and signatures of WAL in the resistance are present up to 3600 nm, which might just still fulfill the condition $d < l_\varphi$, making WAL signals from the bulk possible.

3.2.5 Oscillations in the resistance

For samples grown on rough InP(111), with increased crystal quality and, as determined by Hall measurements, lower carrier densities and higher mobilities there are, as already shown in fig. 3.5, at high magnetic fields oscillations visible in the magnetoresistance.
The oscillations of the resistance originate from the restrictions to the energy of the carriers in a magnetic field when $\mu B >> 1$, they form Landau levels, and are called Shubnikov-de Haas (SdH) oscillations. The energy of the Landau levels changes with the magnetic field B and as B is increased they are consecutively emptied, which causes the oscillations in the resistance, $\Delta\rho_{xx}$, given by [109]:

$$\Delta\rho_{xx} = A(B,T)\,\cos\left[2\pi\left(\frac{F}{B} + 0.5 + \gamma\right)\right]\ , \tag{3.10}$$

with the amplitude A which depends on B and T, the oscillation frequency F, determined by the extremal cross section of the Fermi area, and the Berry phase factor γ. Therefore by analyzing these in $1/B$ periodic oscillations, one can get information about the Fermi area perpendicular to the magnetic field and by extrapolation to an infinite magnetic field information about the Berry phase. Conventional 2-DEGs, with an ordinary dispersion, have a Berry phase of zero but for the topological surface state, with a linear dispersion, a Berry phase factor of 0.5 is predicted [6, 21]. Additionally by changing the angle of the external magnetic field in respect to the surface, one can conclude if the oscillations originate from a 2D state, i.e. they are only dependent on the part of the magnetic field which is perpendicular to the surface.
In fig. 3.15 a measurement on such a Bi_2Se_3-layer with a thickness of 290 nm is shown. Oscillations were seen in various samples and will be discussed exemplary for this sample. The oscillations can be seen in ρ_{xx} and, albeit very small, in ρ_{xy} (see fig. A.1 in the appendix) as well because in the two carrier model ρ_{xy} depends on the individual σ_{xx}. Problematic is the small amplitude of the oscilla-

tions because the in principle unknown background magnetoresistance influences the position of the maxima and minima in the oscillations and makes the analysis imprecise.

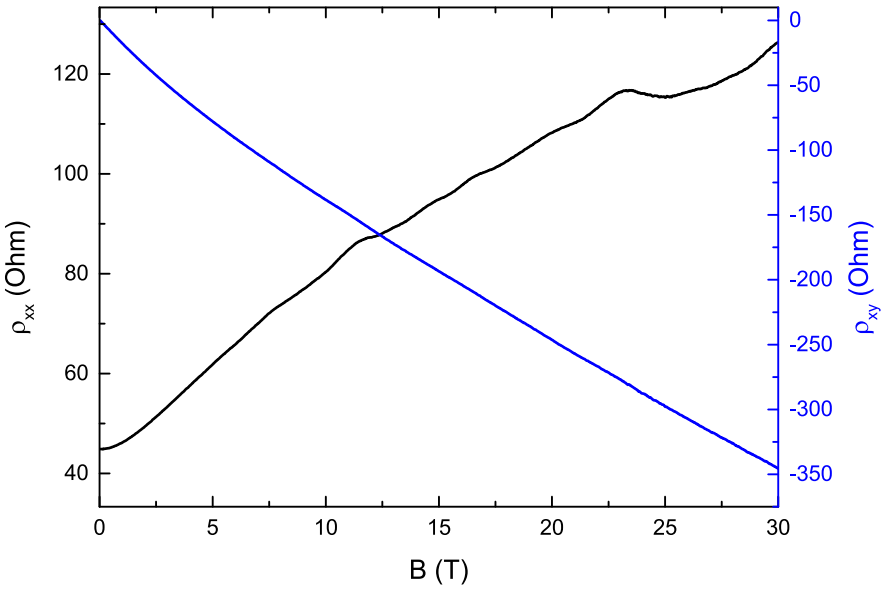

Fig. 3.15: Magnetoresitance of a Bi_2Se_3-layer with a thickness of 290 nm grown on rough InP(111) in a perpendicular magnetic field. At high magnetic fields, $B > 5$ T, oscillations are visible in ρ_{xx}.

To verify if these oscillations have their origin in a 2-DEG or in the bulk, the magnetoresistance is measured at different magnetic field angles, as displayed in fig. 3.16, where, as in the following figures, the smoothed derivative of the resistance in respect to the magnetic field is shown to enhance the visibility. The individual angles are determined by comparison of the as well measured Hall resistance to the perpendicular configuration. There are a lot of wiggles and a distinguished oscillation periodic in $1/B$ is not present. An indication that the oscillations do not have a single homogenous origin. For higher field angles the oscillations move to higher field values but they are still present in a parallel field, which cannot be easily explained by the top or bottom surface of the TI.
To get a clearer understanding if at least some of the oscillations could originate from a 2-DEG in fig. 3.17, only the perpendicular component of the magnetic field is considered. For field angles up to 39° all the oscillations nearly align in position, but for angles higher than 49° they already clearly deviate. An unambiguous attribution of the oscillations to a 2-DEG cannot be made.

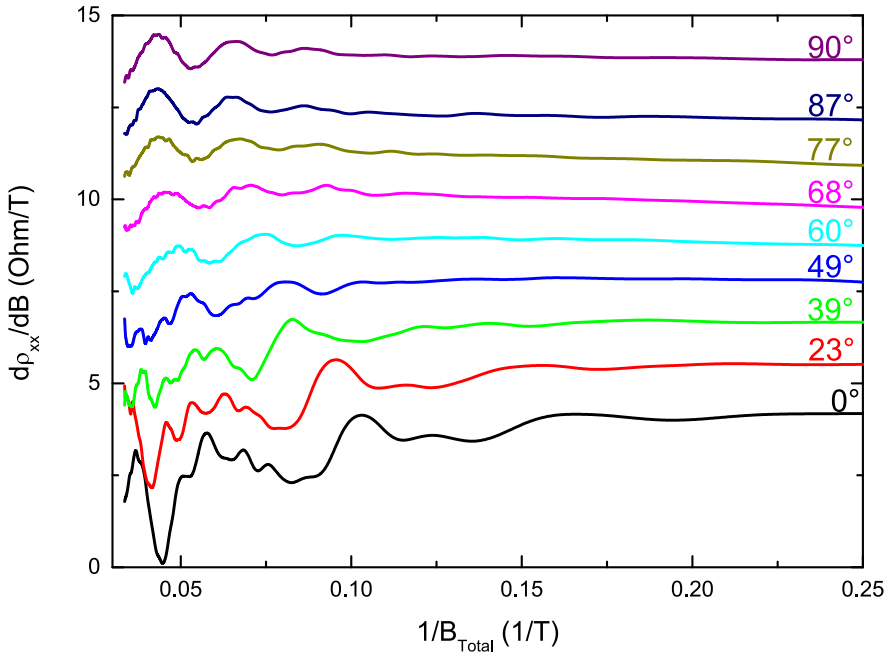

Fig. 3.16: The derivative of the magnetoresistance for different magnetic field angles, vertically shifted for clarity. At 0° the magnetic field is perpendicular to the surface and at 90° the magnetic field is parallel to the surface. Same sample as displayed in fig. 3.15.

If the oscillations indeed come from a 2-DEG the deviations in the angle dependence and the oscillations in a parallel magnetic field have to be explained. In principle the surface on the sides of the TI could cause oscillations in a parallel magnetic field, but since the ratio between the area of top and side surface is about 100:1 for the small Hall bar, on which this measurement was done, its contribution to the conductance should be very small compared to the top and bottom surface. Therefore oscillations in a parallel field with a similar amplitude than for the perpendicular field, as in fig. 3.16 are unlikely to be caused by the side surface. Only the bulk is left as the origin for the oscillations in a parallel magnetic field and consequently as the origin for at least some of the oscillations at the other field angles. A 2-DEG as the only origin is therefore excluded. The only possibilities for a contribution from a 2-DEG to the oscillations might be that only a part of the oscillations originate from it.

The bulk as the only origin of all the oscillations is the other explanation. In this case they would likely originate from pockets away from the gamma point which are likely to have a rather complex dispersion relation. This could explain the

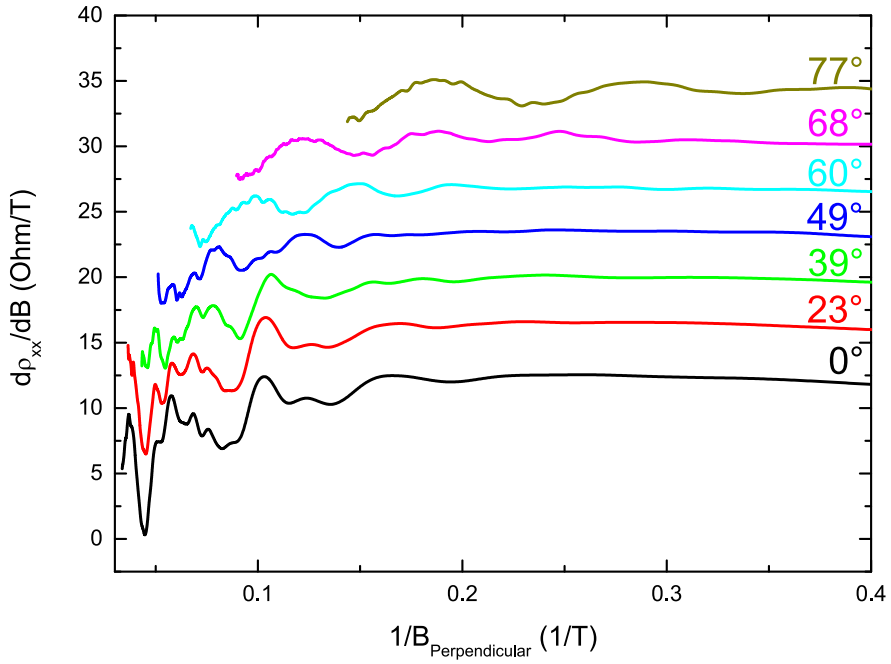

Fig. 3.17: The derivative of the resistance, vertically shifted for clarity, is displayed in respect to only the perpendicular component of the magnetic field to look for a two dimensional origin.

unusual angle dependence behavior of the oscillations which don't match to the Fermi-surface of a sphere.

To distinguish between possible different origins of the oscillations with different characteristic oscillation frequencies the Fourier transform (FT) of the data shown in fig. 3.17 is taken and displayed in fig. 3.18. For the FT only the magnetic field range where oscillations are present is considered. The result is not only a single, but several rather broad peaks, with a FWHM of about 10 T, matching the already mentioned absence of a distinguished oscillation period. No oscillation frequency with a constant value for all angles, meaning only a dependance on the perpendicular component of the magnetic field, is found. A direct relation of one of the oscillation periods to a two dimensional state can therefore not be made.

The carrier density can be obtained by its relation to the oscillation period, $\Delta\left(\frac{1}{B}\right)$. In the 3D case, the magnetic field probes the area of the extremal Fermi-surface, A_k perpendicular to it and in two dimensions only the perpendicular component of the magnetic field is seen by the Fermi-surface. The relation of A_k

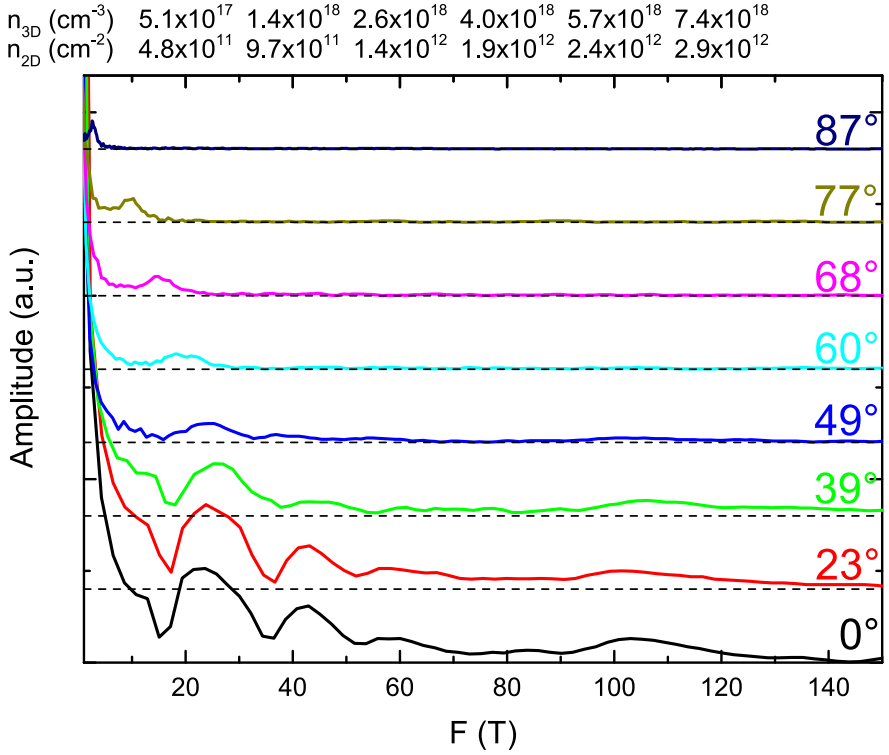

Fig. 3.18: The FT of the signal displayed in fig. 3.17 vertically shifted for clarity is displayed. On the bottom x-axis the frequency of the oscillations and on the upper x-axis the resulting two dimensional and three dimensional (non-linear) density, calculated by eq. 3.12 and 3.13 respectively, are displayed. The dashed black lines are the zero base lines for the individual signals.

to $\Delta\left(\frac{1}{B}\right)$ is:

$$A_k = \frac{2\pi e}{\hbar}\left(\Delta\left(\frac{1}{B}\right)\right)^{-1} . \tag{3.11}$$

For the 2D case this can be directly transformed into a carrier density and for the 3D case under the assumption of a spherical Fermi-surface to get at least an order of magnitude estimation. For two dimensions the result is

$$n_{2D} = g_v \cdot \left(\frac{1}{2\pi}\right)^2 \cdot A_k = g_v \cdot \left(\frac{e}{2\pi\hbar}\right)\left(\Delta\left(\frac{1}{B}\right)\right)^{-1} \tag{3.12}$$

and for three dimensions

$$n_{3D} = g_v \cdot \left(\frac{1}{2\pi}\right)^3 \cdot V_k = g_v \cdot \frac{\sqrt{2}}{3\pi^2}\left(\frac{e}{\hbar}\right)^{\frac{3}{2}}\left(\Delta\left(\frac{1}{B}\right)\right)^{-\frac{3}{2}} \tag{3.13}$$

with the degeneracy factor g_v, which usually takes the value $g_v = 2$ for the spin degeneracy. The densities in relation to the oscillation frequency for 2D, with $g_v = 1$ since the surface state is not degenerate, and for 3D, with $g_v = 2$ for spin degeneracy, can be seen in the upper x-axis of the FT in fig. 3.18. The densities where the FT has its maximum values for 0° are around:

$$\begin{aligned} n_{2D} &= \{5.7, 10, 15, 25\}\, 10^{11}\ \mathrm{cm}^{-2}, \\ n_{3D} &= \{6.5, 16, 27, 61\}\, 10^{17}\ \mathrm{cm}^{-3}. \end{aligned}$$

Where the second and third value for the densities might be the second and third harmonic from the first oscillation frequency. These values can be compared to the parameters obtained from the two carrier model fit in tab. 3.1 and the 2D value is at least an order of magnitude off and the 3D value is in the right order of magnitude.

As a further method to investigate the oscillations, the carrier density can be manipulated with a topgate, like displayed in fig. 3.19 where the oscillations are influenced by the gate voltage. Upon changing the voltage the shape and amount of the visible oscillations alters, such that a specific mapping of them by only assuming a shift is impossible. Under the assumption that the most prominent oscillations have the same origin and shift to lower magnetic field values upon lowering the gate voltage, i.e. reducing the carrier density, in fig. 3.19 an assignment was made. The minima in resistance, where the Fermi-energy lies between two Landau levels, correspond to an integer filling factor, n, and to account for the shift, the maxima in the derivative of the resistance were attributed filling factors, with values of $v = n + 0.25$. As can be seen in fig. 3.19 to achieve a linear relation of v to $1/B$, values of v had to be left out, a possibility if oscillations overlap. An overlap could also account for the change in shape and amount of the oscillations with the gate voltage. The displayed mapping is not the only possible one, but the one where the shifts due to the gate voltage and the y-axis intercept are most constant. Extrapolating the linear fit to $1/B \to 0$ results in an intercept of the y-axis between -0.08 and 0.14. This value is equivalent with the Berry phase factor, and $\gamma = 0$ lies within the error bars of this analysis, making the origin of the oscillations conventional.

The present oscillations of one Bi_2Se_3-layer were analyzed in respect to their behavior under rotation and gating and the resulting carrier density and the

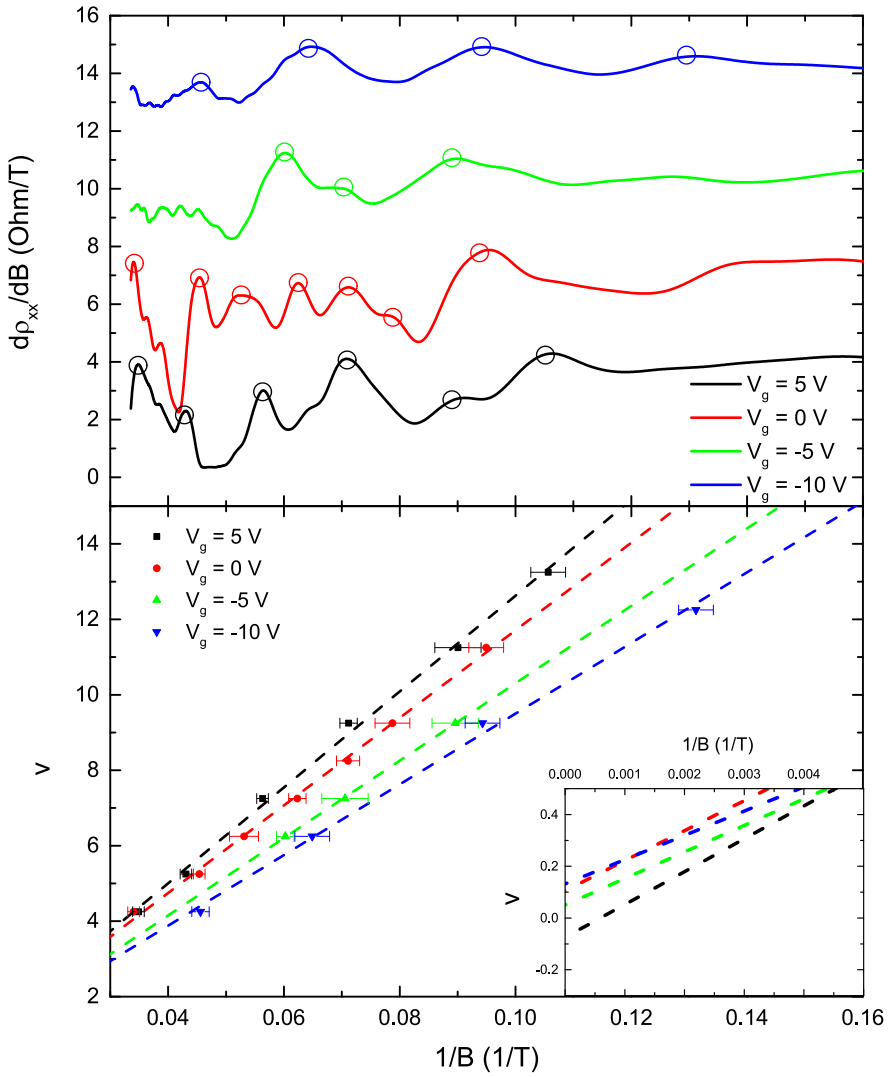

Fig. 3.19: In the top graph the derivative of the resistance in a perpendicular magnetic field is displayed for different gate voltage V_g. The circles are the read out maxima of the most prominent oscillations used for an analysis of the Berry phase. In the bottom graph the read out maxima, with error bars considering the error in the read out due to the smoothing of the data and the overlap of the oscillations, are assigned to a filling factors ν with a linear fit extrapolating to $\frac{1}{B} \to 0$ in the inset. The intercepts of the y-axis range between -0.08 and +0.14.

Berry phase was deducted. Other Bi_2Se_3-layer from the same growth series with a thickness of 20 nm, 50 nm and 190 nm show qualitatively the same results. Concluding from the results of the analysis the surface state is unlikely to be the origin of the oscillations.

SdH-oscillations in the resistance in Bi_2Se_3 and alike materials were also reported on in many publications [37–57].
Obvious signs of SdH-oscillations stemming from a 3D-state as confirmed by their magnetic field angle dependence, with oscillations still present in a magnetic field parallel to the surface, were seen in several cases [37–39]. The shape of the Fermi surface, which is concluded by the angle dependence, is an in c-direction, perpendicular to the surface, elongated ellipsoid, where the area of the cross section even follows up to an angle of about 40° an $1/\cos(\theta)$ dependence like a 2D state.
Later publications showing oscillations of similar amplitude as presented in this section, claimed the origin of their oscillations to be the topological protected surface state. To confirm the 2D origin, the magnetic field angle dependence of the oscillations was measured and an approximate alignment to only the perpendicular component of the magnetic field up to about 50°, not very different from the shown measurements, was observed in every case [40–43, 45–47, 50–52, 55]. The Berry phase factor of the oscillations was determined as well in a similar fashion as in this section and the results were about equally distributed in the range of $\gamma = 0$ to $\gamma = 0.61$ [40–42, 44, 46–52, 54, 56, 57]. One given reason for deviations from a Berry phase factor of 0.5 for a topological surface state were deviations from a linear relation of the landau level filling factor to $1/B$ due to a large g-factor [40, 45]. Another one was that actual the maxima in resistance should correspond to an integer landau level filling factor because of an enhancement of scattering from the dominant bulk carriers if the landau level of the surface is at the Fermi-energy, which leads to an increase instead of a decrease in resistance [44]. Of course these reasons in principle might apply but without further prove of their validity they remain purely speculative. Considering the large spread in the results for the Berry phase the overall accuracy and therefore the validity as a determination method for oscillations of such low amplitude is questionable.

Recently there also have been observations of an actual QHE in $BiSbTeSe_2$ [110] and $(Bi_{1-x}Sb_x)_2Te_3$ [111] films. In both cases at high magnetic fields, B ¿ 10 T, a $\nu = 1$ and $\nu =$ -1 plateau were observed in σ_{xy}. Further the appearance of a plateau-like structure for $\nu = 0$ for a certain gate voltage region, seems to support the claim that the QHE arises from two topological protected surface states, in this special case with $\nu = \nu_1 + \nu_2 =$ -1/2 + 1/2 = 0. But the $\nu =$ 0 feature could as well be explained by the very high longitudinal resistance in this gate voltage region, marking the transition to an insulator with zero conductance. Other given indications like the determined Berry phase factor of 0.5 [110] are already based on the assumption of two half-integer quantized surface states and only shows self consistency of the assumption but cannot be taken as conclusive proof for a measurement of the topological protected surface states.

In this chapter the magnetoresistance observed in Bi_2Se_3 and related layers and the occurring phenomena are described and analyzed. With some exceptions the magnetoresistance can be described by a two carrier model and the carrier density was reduced by an optimization of the growth procedure and switching to the compound $(Bi_{1-x}Sb_x)_2Se_3$, lowering the total carrier density to $4.5 \cdot 10^{17}$ cm^{-3}. The observed linear magnetoresistance, weak anti-localization and oscillations in the resistance might be explained by a topological surface state but neither in a straightforward nor compelling way. Bulk states as the cause of these phenomena are more likely.

Chapter 4

Anomalous and Quantum Anomalous Hall Effect in Topological Insulators

For about 15 years combining semiconductors with magnetism is a popular research field. No longer is only the electron charge of interest but its spin as well. For example the giant magneto resistance, where the resistance of a device depends on the relative spin-orientation of its sections to each other, is already used in commercial hard disks, but so far only in ferromagnetic metals. The benefits magnetic semiconductors can offer among others are spin injection and a change of the magnetization by electric fields and current, useful for applications in spintronic devices, for storage and processing of data. Magnetic doping of topological insulators might offer the same features and has the potential for additional ones. In 2D topological insulators only one of the two spin polarized edge states could be selected through magnetism. This would be the realization of the quantum anomalous Hall effect (QAHE), edge state transport without an external magnetic field, which was proposed for magnetic TIs [112, 113]. One can imagine the QAHE as the realization of the QHE without an external magnetic field or as the quantized version of the anomalous Hall effect (AHE).
First this chapter will describe the development of magnetism in Bi_2Se_3 and alike materials. This includes the theory for a possible exchange mechanism, responsible for the magnetic order in an insulating material, which differs from a magnetic semiconductor. Then the magnetization of the TI materials as determined

by superconducting quantum interference device (SQUID) measurements will be discussed. Moving on from there to the impact of the magnetization on transport measurements for the different magnetic dopants Cr and V and different growth parameters with focus on the AHE and at last the QAHE.

4.1 Ferromagnetism in topological insulators

In a magnet the energy of the system is significantly dependent on the relative orientation of the magnetic moments, which are usually provided by the spins from electrons of not completely filled d- or f-shells, to each other. This energy is called the exchange interaction.
Electrons are fermions thus upon exchanging them, their two particle wave function, consisting of a spatial and a spin part, has to change sign. Therefore one of the parts has to be symmetric and the other one anti-symmetric to make the total wave function antisymmetric. The energy of these two possible solutions differs and makes up the exchange interaction, favoring either a parallel or an anti-parallel spin configuration. In reality there are many magnetic moments which have to be considered and the coupling between the magnetic moments can be indirect, as for example in dilute magnetic semiconductors, making magnetism a very complex phenomenon.
In a ferromagnetic semiconductor, like for example GaMnAs, the local moments provided by the magnetic dopants are indirectly coupled by the free carriers, which is called the RKKY-interaction, and a parallel orientation of the moments is favored in energy leading to ferromagnetism.
For a TI in the ideal case the bulk of the material is insulating making this system unlike conventional magnetic semiconductors, there are no free carriers to couple the magnetic moments. Nevertheless it is possible to realize ferromagnetism in TIs by magnetic doping as is evident by the measured hysteresis of the QAHE [12].
The Van Vleck ferromagnetism was proposed as an explanation [113]. A form of this magnetism connected to the Van Vleck paramagnetism was first described by Bloembergen and Rowland for the exchange interaction of nuclear spins via intermediate electrons in insulators [114]. The already well known Van Vleck paramagnetism follows from second order perturbation theory of the energy shift

of the electron ground state $|0\rangle$ in an external magnetic field which is described by:

$$\begin{aligned}\Delta E_0 &= \mu_B \vec{B} \cdot \langle 0| \vec{L} + \mathrm{g}_0 \vec{S} |n\rangle + \frac{\mathrm{e}^2}{8\mathrm{m}_\mathrm{e}} B^2 \langle 0| \sum_k (x_k^2 + y_k^2) |0\rangle \\ &\quad + \sum_{n' \neq 0} \frac{|\langle 0| \mu_B \vec{B}(\vec{L} + g_0 \vec{S}) |n'\rangle|^2}{E_0 - E_{n'}} \ , \end{aligned} \tag{4.1}$$

where μ_B is the Bohr magneton, $\vec{L}$ is the total orbital angular momentum of the nl-subshell, $\vec{S}$ is the total spin angular momentum, $\mathrm{g}_0 \approx 2$ and x_k^2 and y_k^2 are spatial coordinates. The first term describes the common paramagnetism and is usually dominating for a non-vanishing total angular momentum. The second term describes diamagnetism and the third term Van Vleck paramagnetism, which is in the normal case quite small because of the large separation in energy between the ground state and excited states leading to a large divisor.

In an insulator an exchange interaction between two magnetic moments based on the Van Vleck paramagnetism after Bloembergen and Rowland [114] is possible. Instead of interacting with an external magnetic field, as in eq. 4.1, the wave function of an electron interacts with a magnetic moment, i.e. the wave function of the electron is non-vanishing at the position of the magnetic moment, and the Van Vleck paramagnetism gives a shift in energy. Now if the electron not only interacts with one magnetic moment but with two, the energy shift is not only given by terms depending on only one of the magnetic moments but also on terms depending on both of them. An indirect interaction between the two magnetic moments is therefore given and a certain alignment of the magnetic moments can be favored in energy. Since the Van Vleck paramagnetism is depended on the energy gap between the ground state and an excited state the strength of this interaction is depended on the gap as well.

In the case of a TI the exchange between local moments would be mediated by band electrons. After Yu *et al.* [113] the overlap of the wave function of the ground state, the valence band, and excited states, the conduction band, is enhanced because of the band inversion in a TI. This leads to a larger Van Vleck paramagnetism and in turn to a larger strength of the interaction. A stable ferromagnetic phase is realized.

In a publication by Li *et al.* [115] V-doped Sb_2Te_3 is investigated by electron

energy loss spectroscopy and a shift of the energy of the electronic core levels of V below the Curie temperature of the material is observed. This shift is interpreted as the onset of the ferromagnetic order. This result agrees with an expected decrease of energy levels of the ground states for the Van Vleck magnetism but a demonstration of the exchange mechanism is still missing. Further investigations need to be made to get a full understanding of this type of ferromagnetism in TIs.

4.2 Magnetic doping in $(Bi_{1-x}Sb_x)_2Te_3$

For Bi_2Se_3 and alike materials magnetic doping with the transition metals Fe, Mn, Cr and V was theoretically and experimentally investigated [115–125] and a realization of magnetism in TIs was achieved like in conventional semiconductors. For Cr-doped $(Bi_{1-x}Sb_x)_2Te_3$ thin films a large anomalous Hall effect was reported [126–128] and soon after that the first observation of the QAHE effect was made in this material [12]. Albeit the shown results for the QAHE were first questionable because of the sample design, done by mechanically scratching a Hall bar like structure, the symmetrization of data and the missing evidence of non-local transport the realization of the QAHE was later confirmed in Cr-doped $(Bi_{1-x}Sb_x)_2Te_3$ [129–133] and V-doped $(Bi_{1-x}Sb_x)_2Te_3$ [18, 134, 135].
Like the first reported magnetic TIs with a large anomalous hall effect the first layers by our group were Cr-doped $(Bi_{1-x}Sb_x)_2Te_3$ as well. They were grown on a Si(111) substrate and their magnetic properties were characterized by SQUID and transport measurements.

4.2.1 SQUID measurements

Cr with an electronic configuration of $[Ar]3d^54s^1$ is a transition metal with six electrons in its outer shell and substitutes Bi or Sb in the crystal. The magnetization in Cr-doped $(Bi_{1-x}Sb_x)_2Te_3$ layers of various thickness and Cr-content, which were grown by MBE, was measured by a SQUID as a function of temperature and external magnetic field. From the measured signal the contribution of the substrate, gained by a reference sample, is subtracted. This contribution has to be considered, despite the volume magnetization of the substrate being small, because it is up to 10000 times as thick as the grown layer. The result is

then normalized by the amount of Cr-atoms in the sample as determined by the sample area and the nominal growth values Cr-content and layer thickness.

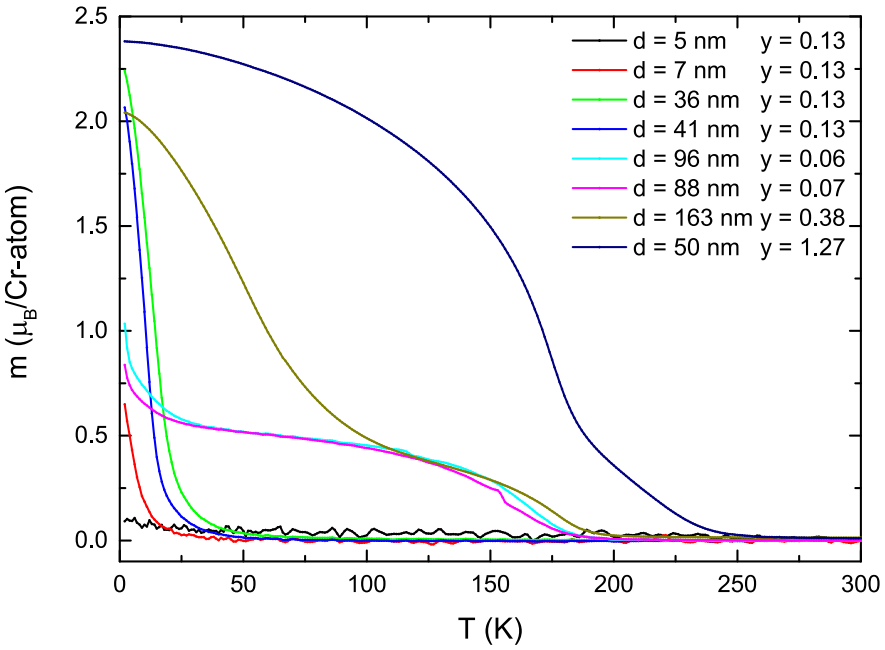

Fig. 4.1: SQUID measurement of the perpendicular-to-plane magnetization on $Cr_y(Bi_{0.2}Sb_{0.8})_{2-y}Te_3$-layers of various thickness and Cr-content in an external perpendicular magnetic field of 0.1 T during cooling of the respective layer.

During cooling all layers down to a thickness of $d = 7$ nm magnetize perpendicular-to-plane, see fig. 4.1. The value of the magnetization, m, and the curie temperature, T_C, depend on the Cr-content and the thickness of the layer. With increasing Cr-content and increasing layer thickness both m and T_C trend to higher values, with m saturating at about 2.4 μ_B/Cr-atom. The Curie temperature is found to be as high as 250 K for the highest Cr-content and as low as 5 K for $d = 7$ nm.

In a crystal lattice the orbital contribution to the magnetic moment of an atom is usually negligibly small, because the electric fields in the lattice determine the plane of the orbits and only the spin of the electrons contribute to the magnetic moment [136], 1 μ_B for each unpaired spin. If Cr indeed substitutes for Bi and Sb in the lattice and gives up three electrons as well this leaves three unpaired electrons in the outer shells of Cr to contribute to the magnetic moment, thus $m_{Cr^{3+}} = 3\ \mu_B$. Considering the possible error for the Cr-content and layer thickness, which are only given by the nominal growth values, and that not every

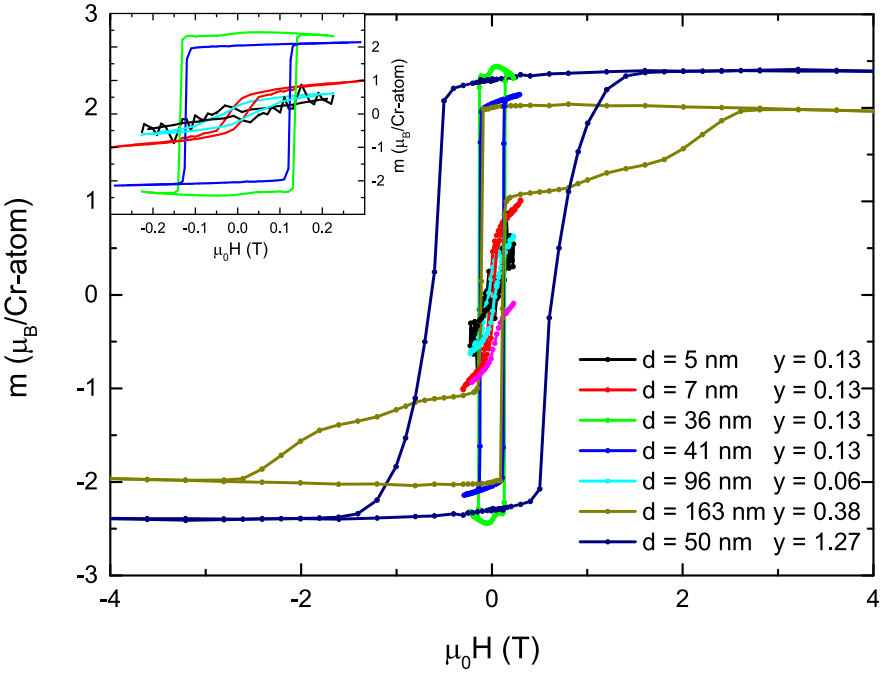

Fig. 4.2: SQUID measurement of the perpendicular-to-plane magnetization on $Cr_y(Bi_{0.2}Sb_{0.8})_{2-y}Te_3$-layers of various thickness and Cr-content at low temperatures ($T = 4.0$ K or $T = 2.0$ K) in an external perpendicular magnetic field. To enhance the visibility of the hysteresis the data which was only acquired for one sweep direction is reflected on the origin in the figure. In the inset a zoom-in is shown to illustrate the hysteresis for layers with small coercive fields.

Cr-atom necessarily contributes to the magnetism the expected and experimental values for the magnetization are in reasonable agreement.

In a magnetic field sweep perpendicular-to-plane the layers show ferromagnetic behavior, a hysteresis in magnetization is visible, as shown in fig. 4.2. Again with increasing Cr-content and the thickness of the layer m as well as the coercive field H_C trend to higher values with m saturating at about 2.4 μ_B/Cr-atom, in agreement with the cooling curves. For the thinnest layers the magnetization weakens. At $d = 7$ nm, the switching of the magnetization broadens and the value of m is lower and at $d = 5$ nm a hysteresis is no longer visible.

Signs of additional magnetic phases are seen in samples with high Cr-content y. For the dark yellow curve with $y = 0.38$ this is clearly seen in the magnetic field sweep which shows an additional broad change in magnetization. The navy curve with $y = 1.27$ shows only one feature for the change in magnetization but compared to layers with lower Cr-content it is extremely broad.

In the parallel-to-plane configuration the magnetization during cooling is an order of magnitude lower and there is no visible hysteresis in the magnetization curve, as can be seen in fig. 4.3 and fig. 4.4.

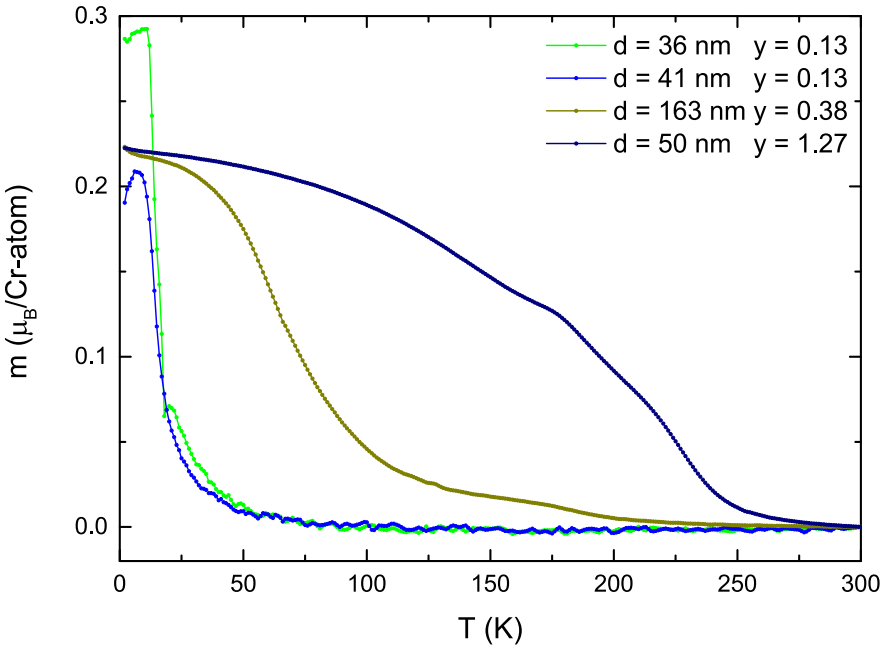

Fig. 4.3: SQUID measurement of the parallel-to-plane magnetization on $Cr_y(Bi_{0.2}Sb_{0.8})_{2-y}Te_3$-layers of various thickness and Cr-content in an external parallel magnetic field of 0.1 T during cooling.

For fields higher than the microscopic coercivity of the material, $\mu_0 H_k = 1.1$ T, the magnetization reaches the same saturation value of 2.4 μ_B/Cr-atom as in the perpendicular configuration. This is the case because then the energy of the interaction of the magnetic moments with a parallel external magnetic field exceeds the anisotropy energy, K, meaning the energy is now minimal if the direction of the magnetization is parallel to the magnetic field. Assuming an uniaxial magnetocrystalline anisotropy, K can be estimated by setting it equal to the energy of the generated magnetic field [136]:

$$K = \frac{1}{2}\mu_0 H_k M, \tag{4.2}$$

with the saturation magnetization $M = m/V_{Cr} \approx 1.9 \cdot 10^6$ A/m, the anisotropy energy is $K \approx 1.3 \cdot 10^6$ J/m^3.

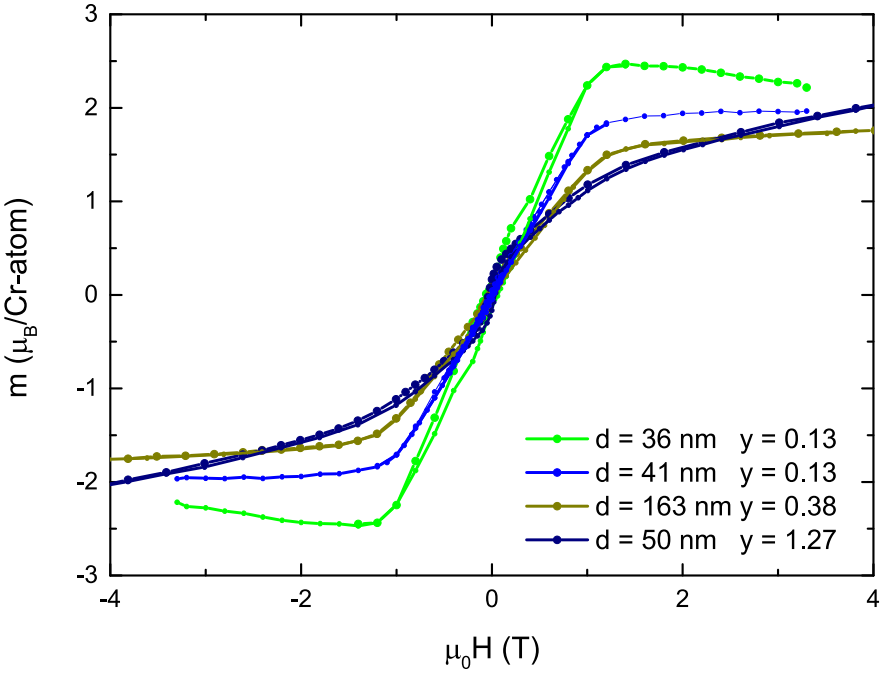

Fig. 4.4: SQUID measurement of the parallel-to-plane magnetization on $Cr_y(Bi_{0.2}Sb_{0.8})_{2-y}Te_3$-layers of various thickness and Cr-content at low temperatures ($T = 4.0$ K or $T = 2.0$ K) in an external parallel magnetic field. To pronounce the visibility of the hysteresis, or respectively the absence of it, the data which was only acquired for one sweep direction is reflected on the origin in the figure.

The perpendicular-to-plane magnetization of the layers is confirmed by SQUID-measurements for layers as thin as 7 nm. For the doping concentration of $y = 0.13$ the results show a single ferromagnetic phase with a sharp switching of the magnetization at the coercive field, which gets broadened upon reducing the layer thickness. Therefore layers with the still reasonable doping concentration $y = 0.13$ will be further studied in transport.

4.2.2 Anomalous hall effect and superparamagnetism

Now the layers are probed by transport measurements in a perpendicular magnetic field. The goal is to realize a high resistance for the anomalous Hall effect, $R_{AHE} = \rho_{xy}(H = 0)$, and simultaneously a low longitudinal resistivity to eventually reach the QAHE-regime, single edge channel transport with a quantized Hall effect of $R_{AHE} = \mathrm{R_K}$, with $\mathrm{R_K} = \mathrm{h/e^2} = 25812.807$ Ohm being the von Klitzing constant, and $\rho_{xx} = 0$.

Samples with a composition of $Cr_{0.13}(Bi_{0.2}Sb_{0.8})_{1.87}Te_3$, being close to the reported charge neutral point [126], were fabricated into Hall bars with a topgate and measured at $T = 4.2$ K. The layers have various thicknesses and were grown at two different substrate temperatures with $T_{Sub} = 300°C$ and $T_{Sub} = 180°C$.

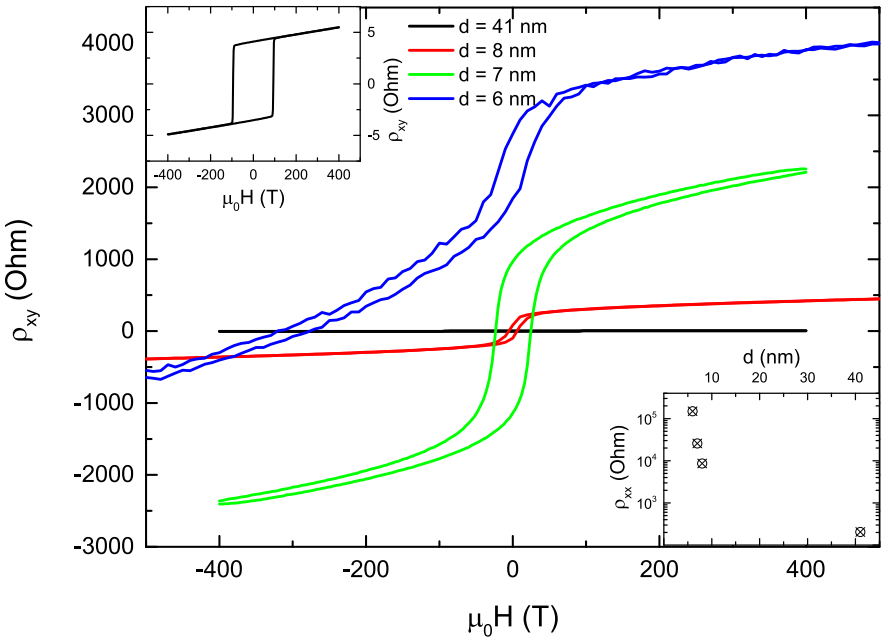

Fig. 4.5: ρ_{xy} during a magnetic field sweep for $Cr_{0.13}(Bi_{0.2}Sb_{0.8})_{1.87}Te_3$-layers of various thickness grown at $T_{Sub} = 300°C$ at $T = 4.2$ K. In the inset on the upper left side ρ_{xy} for $d = 41$ nm and in the inset on the lower right the value of ρ_{xx} for the different thicknesses is shown.

In fig. 4.5 a measurement of ρ_{xy} for different layer thicknesses in dependence on the external magnetic field is shown. At a certain field value ρ_{xy} changes sign and a hysteresis is visible. The transport measurements agree with the already shown SQUID measurements. The sign change of ρ_{xy}, for thin layers between 10 mT and 30 mT, coincides with the coercive field determined by SQUID. By reducing the thickness of the grown layers ρ_{xy} increases and ρ_{xx}, which is shown with a logarithmic scale in the inset, even more so.

The trend of increasing resistivity is also reflected in the temperature dependence of ρ_{xx} in fig. 4.6. For a thickness of $d = 5$ nm the layer becomes insulating around $T = 110$ K and for the slightly thicker samples with $d = 6$ nm and $d = 7$ nm it can be seen that an exponential increase of ρ_{xx}, also starts to develop at temperatures below 10 K. For $d = 6$ nm the high resistivity already causes an offset

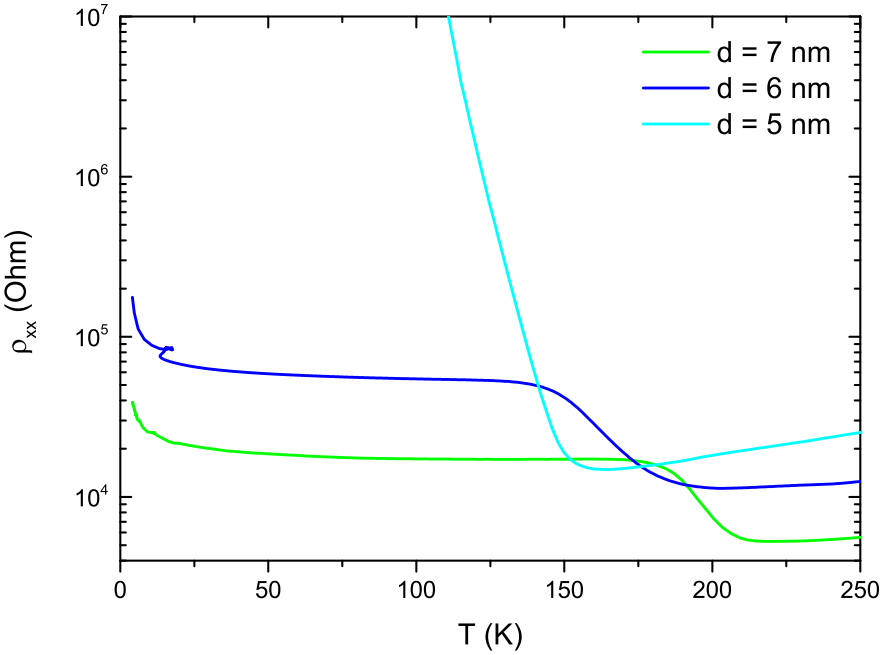

Fig. 4.6: Temperature dependence of ρ_{xx} for $Cr_{0.13}(Bi_{0.2}Sb_{0.8})_{0.87}Te_3$-layers of different thickness grown at $T_{Sub} = 300°C$.

in the hall measurement, as it can be seen in fig. 4.5, and the amplitude of the anomalous hall resistance no longer significantly increases.

At both chosen growth temperatures the values of ρ_{xx}, ρ_{xy} and H_c are quite similar but a difference is seen in the dependence on the topgate voltage shown exemplary for two samples in fig. 4.7. For a growth temperature of $T_{Sub} = 300°C$ a maximum in ρ_{xy} is observed and for $T_{Sub} = 180°C$ ρ_{xy} rises continuously upon increasing the gate voltage. The presence of a maximum indicates, that at high growth temperatures the layer is closer to charge neutrality and that it can be reached by gating.

The magnitude of ρ_{xy} strongly depends on the temperature as well. As it can be seen exemplary in fig. 4.8 ρ_{xy} approximately doubles upon decreasing the temperature from 4.2 K to 1.6 K.

In the presented measurements a clear trend is observed that upon reducing the thickness or the temperature of the samples, ρ_{xy} as well as ρ_{xx} increases, demonstrated in fig. 4.9. The increase in ρ_{xx} is problematic because for very small thicknesses the samples are insulating at low temperatures, e.g. the layer with $d = 7$ nm and $T_{Sub} = 300°C$ is insulating at $T = 30$ mK. As a consequence layers with a too high ρ_{xx}, $\rho_{xx}(T = 4.2\text{ K}) > 20$ kOhm, are considered unsuitable

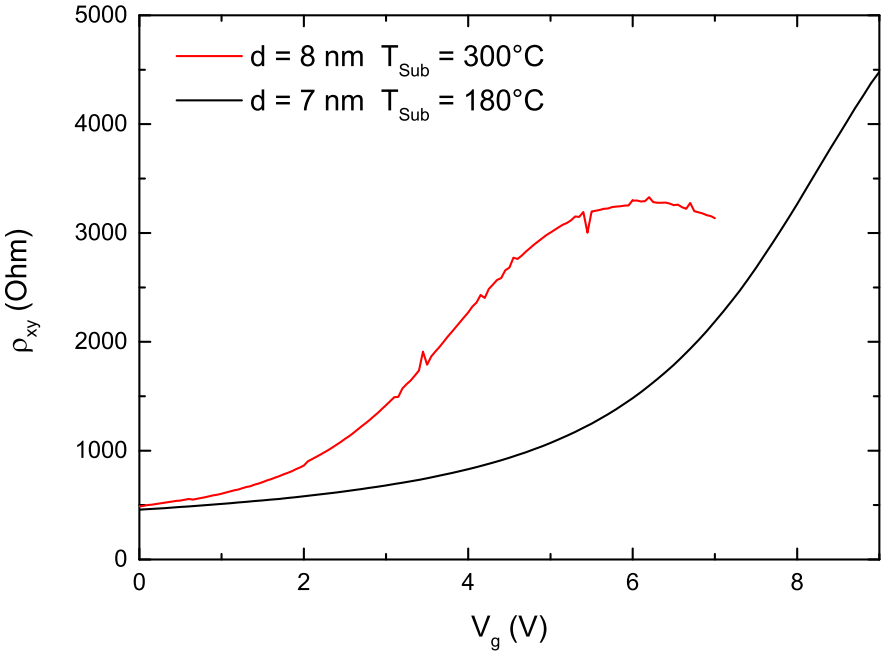

Fig. 4.7: Gate dependence of ρ_{xy} for two $Cr_{0.13}(Bi_{0.2}Sb_{0.8})_{0.87}Te_3$-layers of different growth temperatures at $T = 4.2$ K and $\mu_0 H = 500$ mT to ensure stable magnetization.

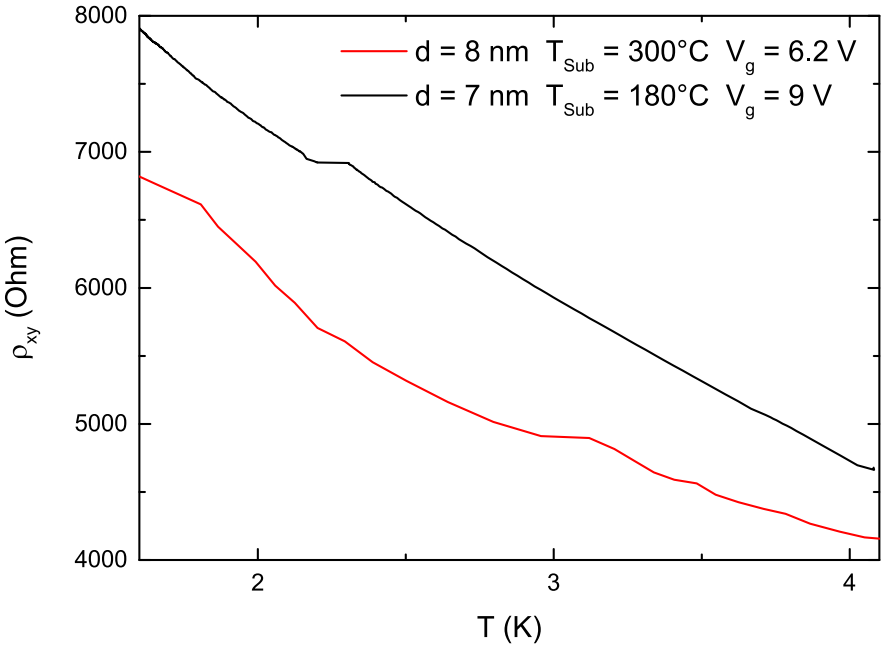

Fig. 4.8: ρ_{xy} for $Cr_{0.13}(Bi_{0.2}Sb_{0.8})_{0.87}Te_3$-layers upon lowering the temperature from 4.2 K to 1.6 K. Prior to the measurement the gate voltage was set to maximize ρ_{xy} and the magnetic field set to 500 mT to ensure stable magnetization.

for electric transport but a high ρ_{xy} is still aspired. Therefore the sample with $d = 7$ nm and $T_{Sub} = 180°C$ is selected for further measurements.

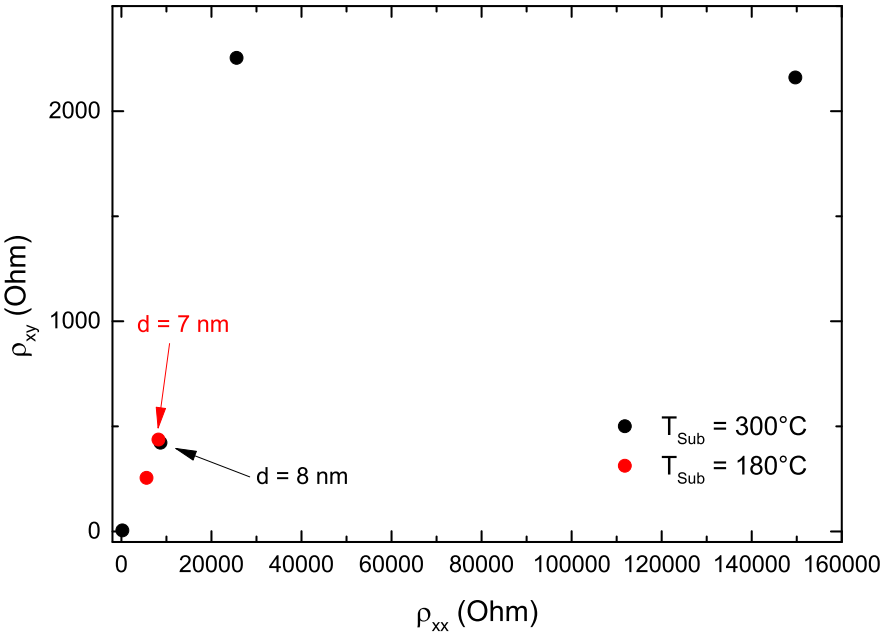

Fig. 4.9: ρ_{xy} mapped to ρ_{xx} at $T = 4.2$ K for the two different substrate temperatures and different thicknesses.

Taking a closer look at the switching events of the magnetization reveals that the magnetism in this layer, as well as in the previously discussed ones, is even at low temperatures not stable. At a constant external magnetic field, several mT away from the coercive field, the anomalous hall resistance decreases over time, as can be seen in fig. 4.10 for a temperature of $T = 1.6$ K, well below half of T_C. The anomalous hall effect actually even decreases noticeable at an external field of $H = 0$ at a time scale of minutes. A decrease of ρ_{xy} is also observed in thicker samples shown in fig. A.5 in the appendix.

Such a magnetization which is not stable in time is called superparamagnetism and manifests in small ferromagnetic particles. The energy barrier separating the two directions of the magnetization is of the order of $k_B T$ and random switching between the two states is possible. Consequently a previously magnetized state will relax at $H = 0$ to a net magnetization of zero. The exponential time dependence of the magnetization of a superparamagnet in zero field is given by [136]:

$$M(t) = M(0) \cdot \exp\left(-\frac{t}{\tau}\right) , \tag{4.3}$$

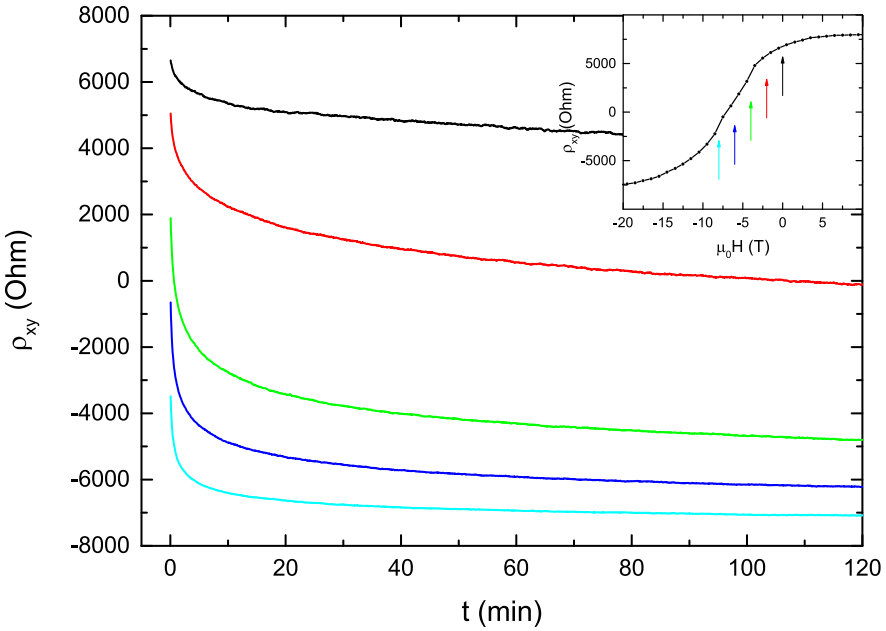

Fig. 4.10: Measurement over time at different constant magnetic fields and $T = 1.6$ K. The magnetization of the sample for each measurement was prepared by sweeping from positive saturation to the magnetic field indicated by the arrow of the corresponding color in the inset. The black curve shows the decay of ρ_{xy} at zero external field.

with the decay constant τ.

An explanation of this behavior would be the existence of small Cr-clusters as magnetic particles in the material, which has already been reported for related materials like $CrS_{1-x}Se_x$ and CrS_xTe_{1-x} [137, 137]. Assuming that the superparamgnetism in the $Cr_{0.13}(Bi_{0.2}Sb_{0.8})_{1.87}Te_3$-layers is caused by such clusters their volume, V_c, is related to τ by the Néel-Arrhenius equation[138]:

$$\tau = \tau_0 \cdot \exp\left(\frac{KV_c}{k_B T}\right) , \tag{4.4}$$

with the attempt time τ_0 being typically around 10^{-10} s and the anisotropy energy $K \approx 1.3 \cdot 10^6$ J/m^3 of this material, approximately known from the SQUID-measurements.

Under the assumption that the anomalous hall resistance is directly proportional to the magnetization, $R_{AHE} \propto M$, the measured time dependence should be possible to fit with eq. 4.3. As it turns out it is not, because of the exponential dependence of τ on V_c in eq. 4.4. Small variations in V_c, which are most

likely present, result in huge changes of the decay time and to fit $R_{AHE}(t)$ a distribution of the decay time, $P(\tau)$, instead of a single value of τ, has to be assumed. This results in:

$$R_{AHE}(t) = R_{AHE}(0) \int_0^\infty P(\tau) \cdot \exp\left(-\frac{t}{\tau}\right) d\tau. \tag{4.5}$$

With this equation the measured decay of R_{AHE} at zero external magnetic field is fitted and the to $P(\tau)$ corresponding volume distribution, $P(V_c)$ of the Cr-clusters is calculated using the relation from eq. 4.4. The result is shown in fig. 4.11. The distribution of the particle sizes is comprised of two peaks, a broad

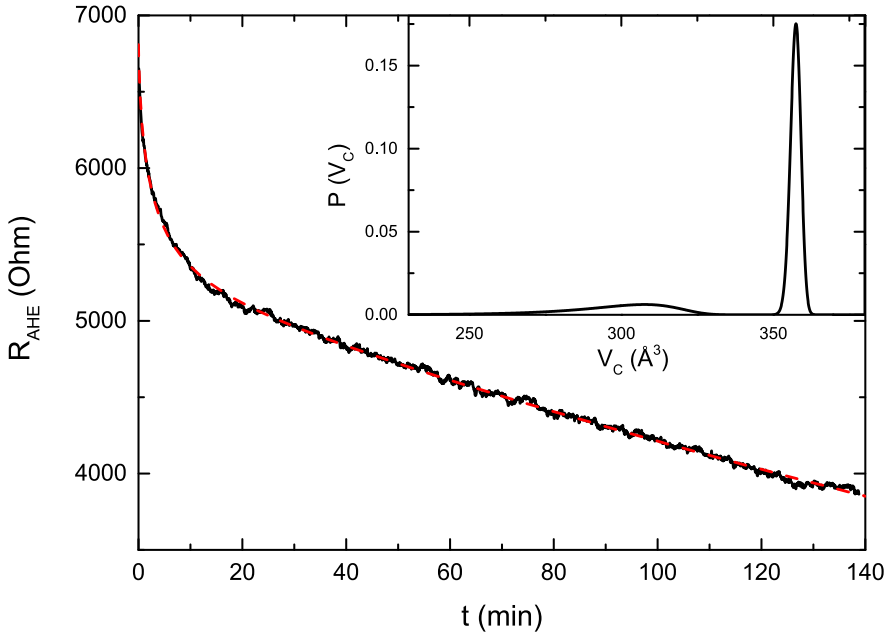

Fig. 4.11: Measurement of R_{AHE} over time at $\mu_0 H = 0$ T and $T = 1.6$ K. The magnetization of the sample was prepared by sweeping from positive saturation to 0 T. The measured data is shown in black and the fit as a red dashed line. In the inset the volume distribution corresponding to the fit is shown.

one around 420 Å^3 and a narrow one around 490 Å^3. While the result can only be viewed as an estimation it indicates that the magnetization, or at least a part of it originates from small magnetic inclusions. The determined particle size is relatively small and could not be resolved by other measurement techniques, e.g. in TEM measurements. A possible location for the formation of such clusters would the numerous grain boundaries in this material.

The layer with $d = 7$ nm and $T_{Sub} = 180°C$ was cooled down further to a temperature of $T = 30$ mK in a dilution refrigerator to gain further insight into the anomalous hall effect of $Cr_{0.13}(Bi_{0.2}Sb_{0.8})_{1.87}Te_3$. The intention is to freeze out the remaining bulk carriers and to stabilize the magnetism and get a larger R_{AHE}. For lower temperatures ρ_{xx} continues to rise and for the base temperature of the dilution fridge, $T = 30$ mK, the sample is no longer an ohmic conductor, as can be seen in the nonlinear IV-curve in fig. 4.12. For two-terminal voltages below

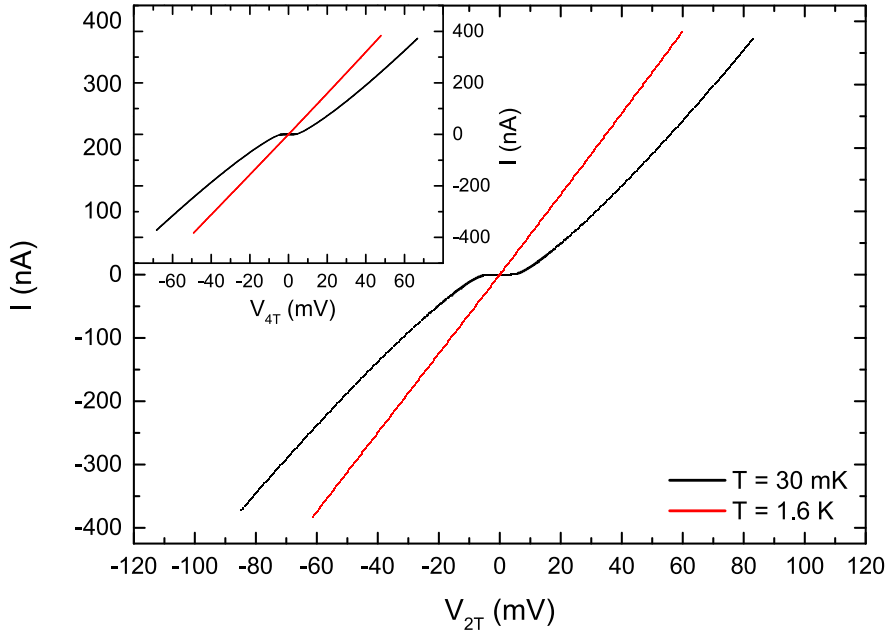

Fig. 4.12: IV curve of the $Cr_{0.13}(Bi_{0.2}Sb_{0.8})_{1.87}Te_3$-sample with $d = 7$ nm for temperatures of 1.6 K and 30 mK. The main graph shows the current in dependence on the two-terminal voltage V_{2T}, measured at the contacts where the current is injected into the hall bar. The inset shows the current in dependence on the four-terminal voltage drop V_{4T} measured between two adjacent contacts on the hall bar. At fridge base temperature both curves show non-linear behavior.

10 mV the sample behaves like an insulator, within measurement accuracy zero current is flowing. Upon going to higher voltages the slope of the IV-curve increases, a current starts to flow and for voltages higher than 40 mV the IV-curve is approximately linear. This behavior resembles variable range hopping, which describes low temperature conductance in strongly disordered systems with localized charge carriers. The localized carriers need a certain activation energy to move to the next free state, which results in the insulating behavior at low voltages.

Measurements of quantities like ρ_{xx} and ρ_{xy} are, because of the non-linear behavior, no longer well defined in such a system, but to get at least some useful results the transport experiments were carried out at atypical high bias voltages $V_{Bias} = 100$ mV where the IV-curve is linear. This certainly leads to a significant increase in the electron temperature. The carrier density in the sample was then manipulated to move it towards the charge neutral point and the largest ρ_{xy} by applying a positive voltage to the topgate. Both ρ_{xx} and ρ_{xy} continuously increase by increasing the gate voltage, see fig. 4.13. The sample is in the p-doped regime and a crossover from p-type to n-type cannot be achieved in the available gate range.

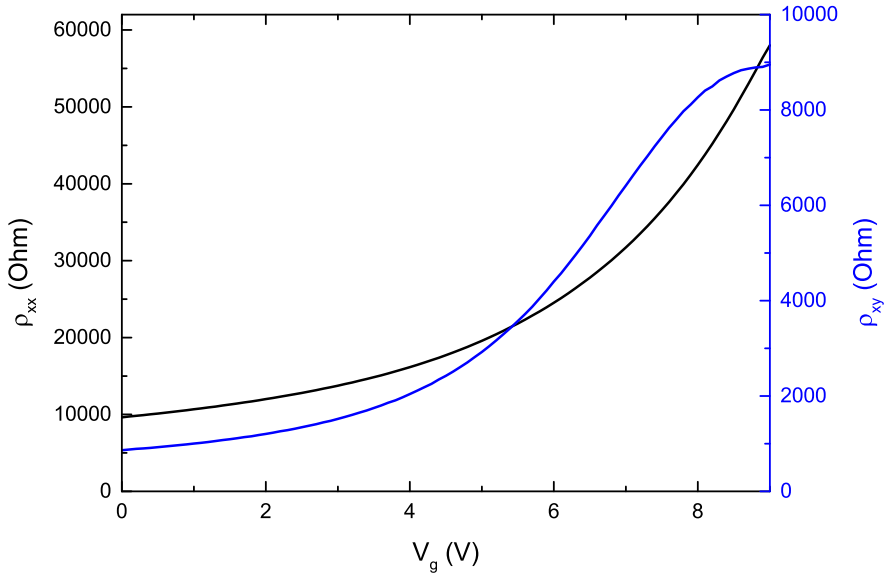

Fig. 4.13: Measurement of the gate voltage dependence of ρ_{xx} and ρ_{xy} on the $d = 7$ nm layer at $T = 30$ mK and $\mu_0 H = 1$ T with a high bias voltage of $V_{Bias} = 100$ mV.

The magnetic field sweep was then carried out for the highest gate voltage the insulator of the gate can sustain, $V_g = 9$ V. As can be seen in fig. 4.14 the anomalous hall effect is present and reaches a value of about 9 kOhm and no signs of quantization are seen.

Because this sample showed insulating behavior another layer with $d = 8$ nm and $T_{Sub} = 300°C$ which also showed a reasonable ρ_{xx} and large ρ_{xy}, see fig. 4.9, was measured as well and it remains conducting with a linear IV-curve up to $T = 30$ mK. It exhibits a high $\rho_{xx} \approx 40$ kOhm and $R_{AHE} \approx 11$ kOhm, see fig. A.6 in the appendix, but also is far off the quantized values.

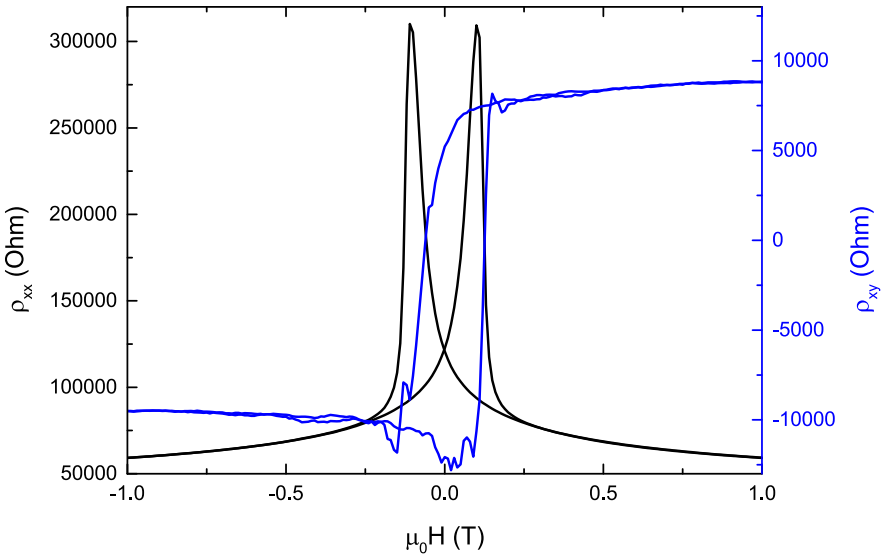

Fig. 4.14: Measurement of the magnetic field dependence of ρ_{xx} and ρ_{xy} on the $d = 7$ nm layer at $T = 30$ mK and $V_g = 9$ V with a high bias voltage of $V_{Bias} = 100$ mV.

The signature of superparamagnetism, a decreasing magnetization over time, is still observed at $T = 30$ mK. At fields which are more than 10 mT away from the switching field the magnetization changes over time as displayed in fig. 4.15, but no longer at $H = 0$. This agrees with the exponential dependence on the temperature given in eq. 4.4.

Thin Cr-doped $(Bi_{0.2}Sb_{0.8})_2Te_3$-layers were measured in electric transport at low temperatures. A large anomalous hall effect is realized by reducing the thickness of the layers to only several nanometers. Reducing the thickness also increases the longitudinal resistance and for thin samples and low temperatures insulating behavior is observed. A quantization of the hall resistance, like in [12], with a vanishing longitudinal resistance could not be realized. Additionally the magnetization of the samples is not stable and shows signs of superparamagnetism, a change of magnetization over time at constant external magnetic fields. This points to the formation of small Cr-clusters in the layers, making the magnetism non-uniform, and the layer composition inhomogeneous. The assumption of an inhomogeneous layer is also supported by the non-ohmic behavior at low temperatures resembling the characteristics of a disordered system.

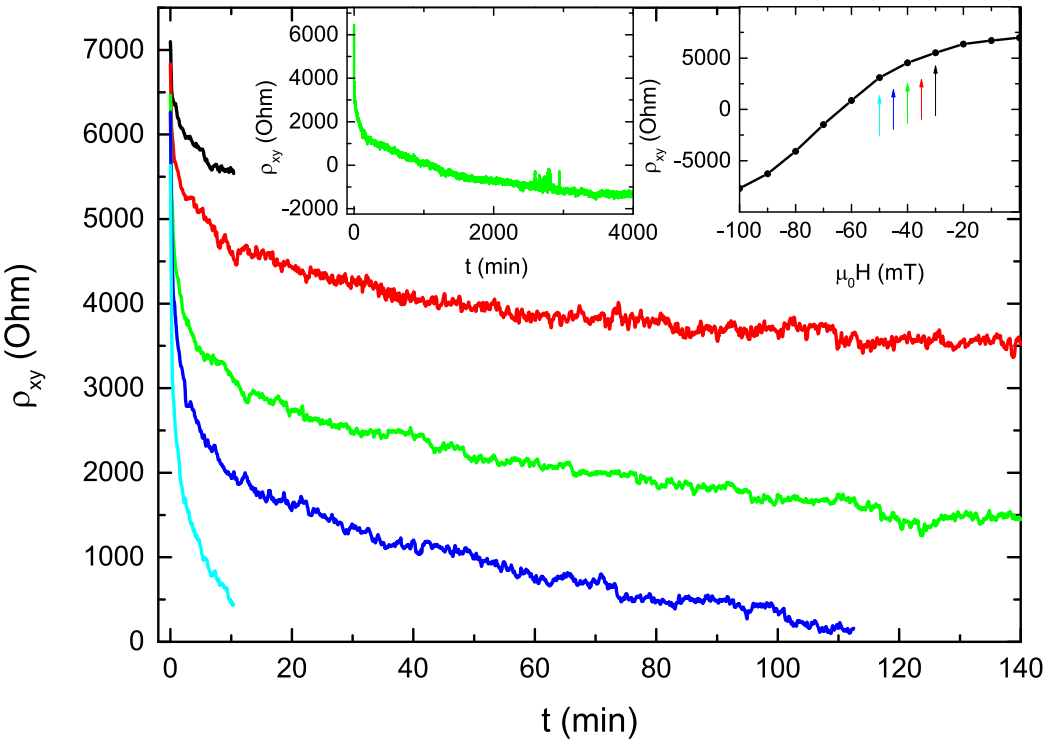

Fig. 4.15: Measurement over time at different constant magnetic fields and $T = 30$ mK. The magnetization of the sample for each measurement was prepared by sweeping from positive saturation to the magnetic field indicated by the arrow of the corresponding color in the inset in the upper right corner. The second inset shows the measurement at $\mu_0 H = -40$ mT at a larger time scale, with ρ_{xy} changing its sign.

In conclusion the investigated MBE-grown Cr-doped $(Bi_{0.2}Sb_{0.8})_2Te_3$-layers are not suitable as a system for the realization of the QAHE.

4.3 Increasing the anomalous hall effect

Soon after the realization of the QAHE [12] it was shown that there is a superior alternative to Cr for magnetic doping which exhibits the QAHE as well [134, 135]: Vanadium. V does offer two distinct advantages over Cr. First V-doped layers show higher values of T_C and H_c, the magnetism in these layers is more robust. Second the electronic configuration of V, $[Ar]3d^34s^2$, resembles Bi and Sb more closely, each having 5 electrons in their outer shell, meaning V should only act as a magnetic and not as an electronic dopant. This gives a higher level of control over the carrier concentration, a critical parameter to realize the QAHE.

For MBE-growth V is a challenging material because a very high temperature, $T \approx 1200°C$, is needed to achieve a reasonable vapor pressure. The V cell has to be heated up to its limit to get the desired amount of dopants and the heat, which it radiates, significantly alters the substrate temperature at the front surface. The growth conditions for thin samples with a layer thickness of $d \approx 9$ nm were optimized consecutively in respect to substrate temperature, V-content and Bi to Sb ratio with the priority to reach a large R_{AHE} and also a low ρ_{xx}. An additional 10 nm thick capping layer of insulating Te was introduced for protection against the environment.

First layers were grown with substrate temperatures in the range from $T_{Sub} = 300°C$ to $T_{Sub} = 130°C$. This temperature is measured at the back of the substrate and, because of the heat radiating from the V-cell, differs from the higher temperature at the front by an undetermined amount. The layers were grown under the same flux ratios for a nominal composition of $V_y(Bi_{0.44}Sb_{0.56})_{2-y}Te_3$ with the exception of the V-content with nominal values of $y = 0.10$ for $T_{Sub} > 190°C$ and $y = 0.15$ for $T_{Sub} \leq 190°C$. The actual layer compositions nevertheless differ due to the varying influence of the substrate temperature on the desorption coefficients of V, Bi and Sb. The measurement results for the anomalous hall effect at $T = 4.2$ K are displayed in fig. 4.16.

For $T_{Sub} \geq 230°C$, R_{AHE} and $\mu_0 H_c$ of the measured samples are smaller than 100 Ohm and 10 mT respectively. By lowering the substrate temperature further to $T_{Sub} = 190°C$ and below, both R_{AHE} and H_c increase by an order of magnitude. Even considering variations in the sample composition, low growth temperatures seem to be essential to realize a large R_{AHE} and a robust magnetization. A consequence of the lowered growth temperatures, compared to $T_{Sub} = 300°C$ for the optimal growth of Bi_2Se_3 [81], is a degradation in crystal quality.

In parallel to the optimization of the substrate temperature during growth the influence of the V-content on the magnetization and the anomalous Hall effect was investigated. At a substrate temperature of $T_{Sub} = 230°C$ and a constant Bi to Sb ratio samples with different nominal V-content were fabricated. In fig. 4.17 the Hall resistance measured at $T = 4.2$ K is displayed and it can be seen that the conditions for a sharp switching event and a large R_{AHE} are best fulfilled for $0.10 < y < 0.33$. Since a smaller amount of V is favorable for a homogenous sample composition, the V-content in the subsequent samples was picked in the

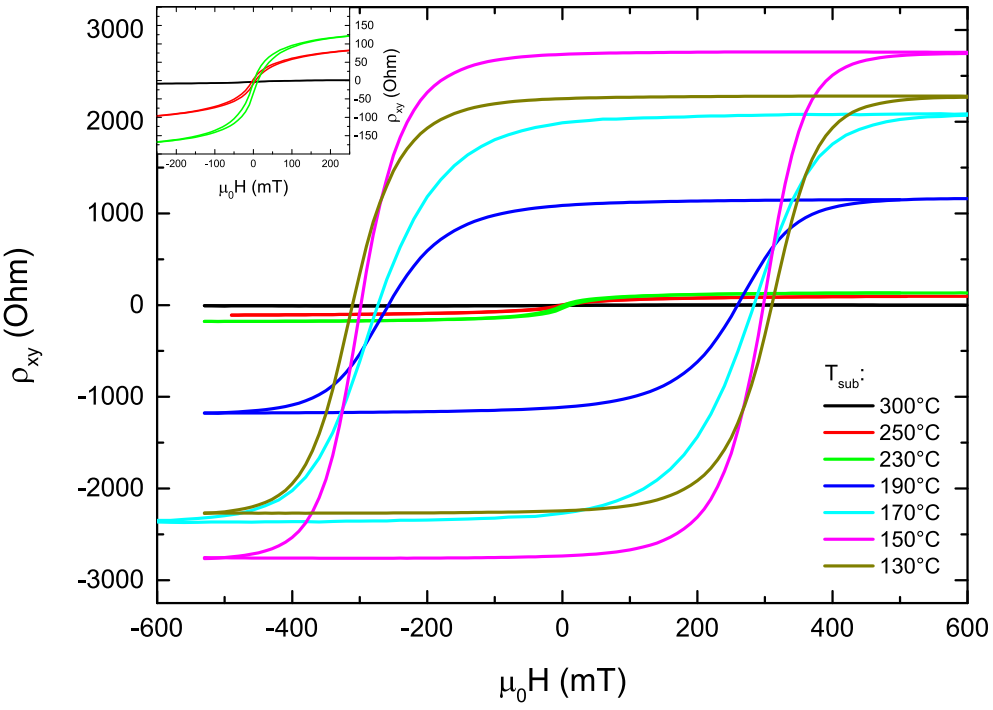

Fig. 4.16: Measurement of the anomalous hall effect at $T = 4.2$ K for V-doped $(Bi_{0.44}Sb_{0.56})_2Te_3$-layers (nominal composition) grown at different substrate temperatures T_{Sub}.

lower part of this regime at a nominal value of $y = 0.15$.

The last parameter which was optimized is the Bi to Sb ratio, which turns out to have a big influence on R_{AHE} as well as on H_c. The optimization was done at $T_{Sub} = 190°C$, which was, at that time, the substrate temperature with the highest measured R_{AHE}. For this step the actual composition of the $V_{0.1}(Bi_{1-x}Sb_x)_{1.9}Te_3$-layers was determined after growth by the lateral lattice constant gained from XRD measurements and by energy-dispersive X-ray spectroscopy on thicker layers [139]. Seven layers with different Sb-concentrations x in the range of $0.56 \leq x \leq 0.95$ and one layer grown on a InP(111) substrate instead of Si(111) were measured at $T = 4.2$ K. All layers except the one with $x = 0.95$ were measured as well in one of two different dilution refrigerator setups, at their respective fridge base temperatures of 15 mK and 50 mK. For the analysis of the results the difference in the base temperatures is of no consequence.

The dependence of ρ_{xy} and ρ_{xx} on the gate voltage and perpendicular external magnetic field was taken for all samples. In the gate dependence a maximum in both ρ_{xy} and ρ_{xx} is seen for $x \leq 0.86$. It is concluded that the layers are near the

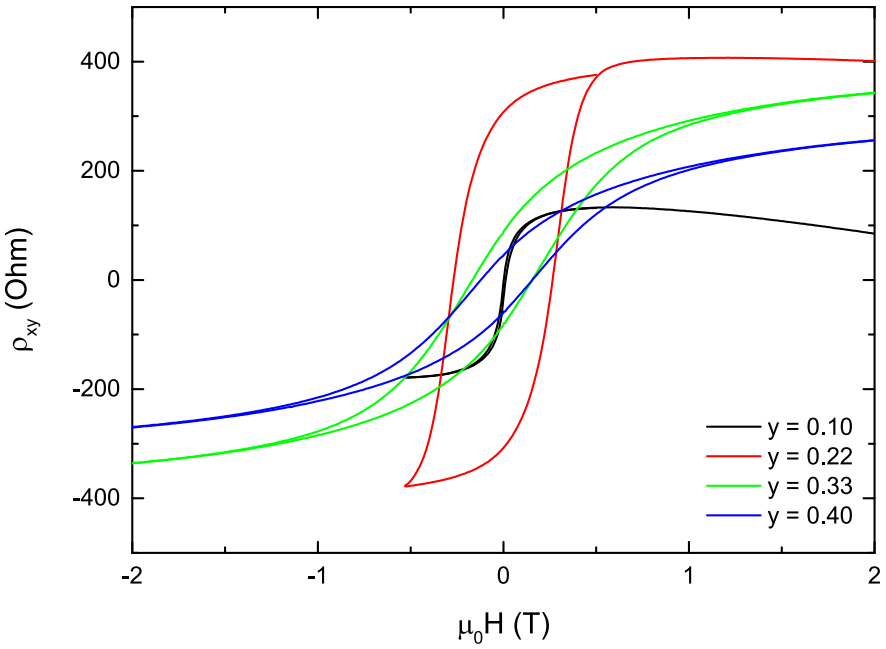

Fig. 4.17: Measurement of the anomalous hall effect at $T = 4.2$ K for $V_y(Bi_{0.44}Sb_{0.56})_{2-y}Te_3$-layers (nominal composition). For $y = 0.22$ the sample was not completely magnetized in the negative direction, therefore the hysteresis curve is asymmetric. The conclusions are still valid.

charge neutral point and can be tuned to it by the topgate. The magnetic field sweeps were done at the gate voltage, $V_g = V_0$, with the maximal anomalous hall resistance $R_{AHE,max}$. If a maximum of R_{AHE} was not reached inside the available gate range the measurement was conducted at a gate voltage of $V_g = 9$ V. For better visibility the values of $R_{AHE,max}$, V_0 and H_c are extracted from the measurements and their dependence on x is shown in fig. 4.18 and fig. 4.19. The actual measurements for a changing external magnetic field are shown in fig. 4.20 and fig. 4.21. The gate voltage V_0 is for every measured composition positive, corresponding to a depletion of p-type carriers, and increases with increasing Sb-content until at $x \geq 0.86$ it is in proximity to or is higher than the breakdown voltage of the dielectric, i.e. R_{AHE} cannot be maximized. In fig. 4.18 a maximum in the investigated region for $R_{AHE,max}$ at $x = 0.79$, both at $T = 4.2$ K and at millikelvin temperatures, is visible.

The QAHE is achieved for $x = 0.79$ at $T = 15$ mK, $H = 0$ and $V_g = V_0$, as can be seen in fig. 4.21 and 4.22, and the measured values of ρ_{xx} and ρ_{xy} are 0.005 R_K and 0.9996 R_K respectively, very close to the literature value for quantization.

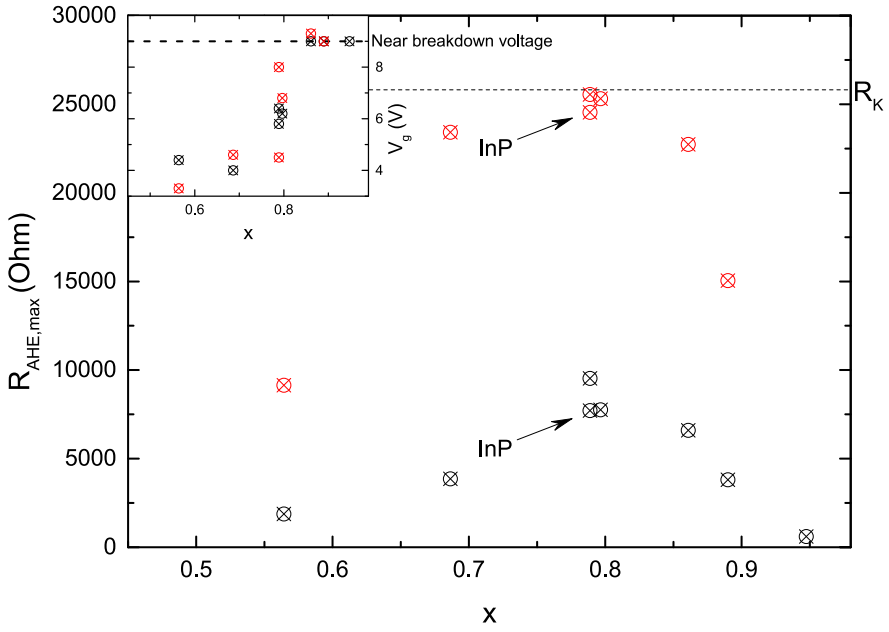

Fig. 4.18: The anomalous hall effect at $T = 4.2$ K (black) and fridge base temperature (red) for $V_{0.1}(Bi_{1-x}Sb_x)_{1.9}Te_3$-layers grown at $T_{Sub} = 190°C$ on Si(111) and one layer on InP(111). The gate voltage at which the measurement was conducted is shown in the inset. The gate voltage at which R_{AHE} is maximal varies slightly for $T = 4.2$ K to millikelvin temperatures.

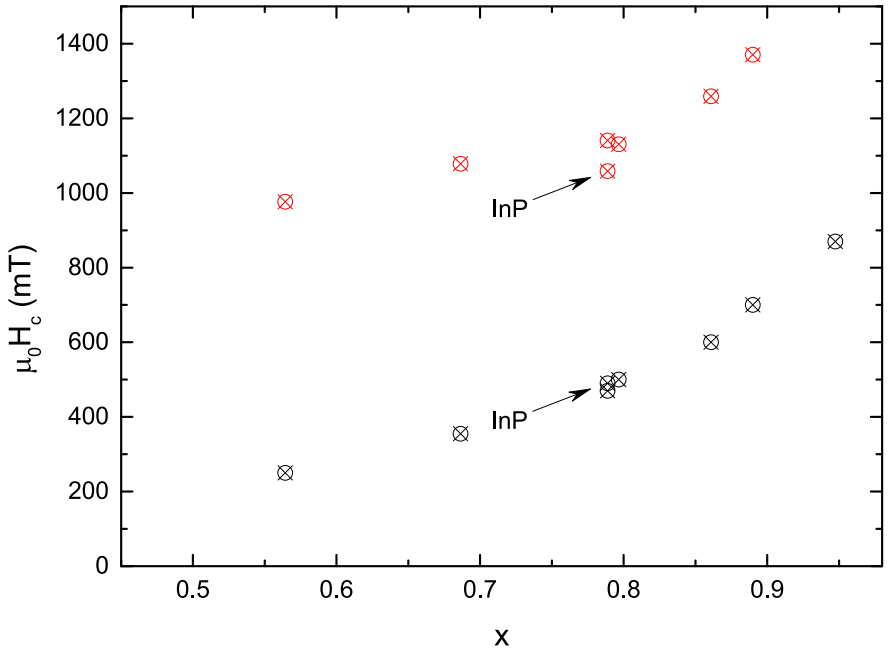

Fig. 4.19: The coercive field at $T = 4.2$ K (black) and fridge base temperature (red) for $V_{0.1}(Bi_{1-x}Sb_x)_{1.9}Te_3$-layers grown at $T_{Sub} = 190°C$ on Si(111) and one layer on InP(111).

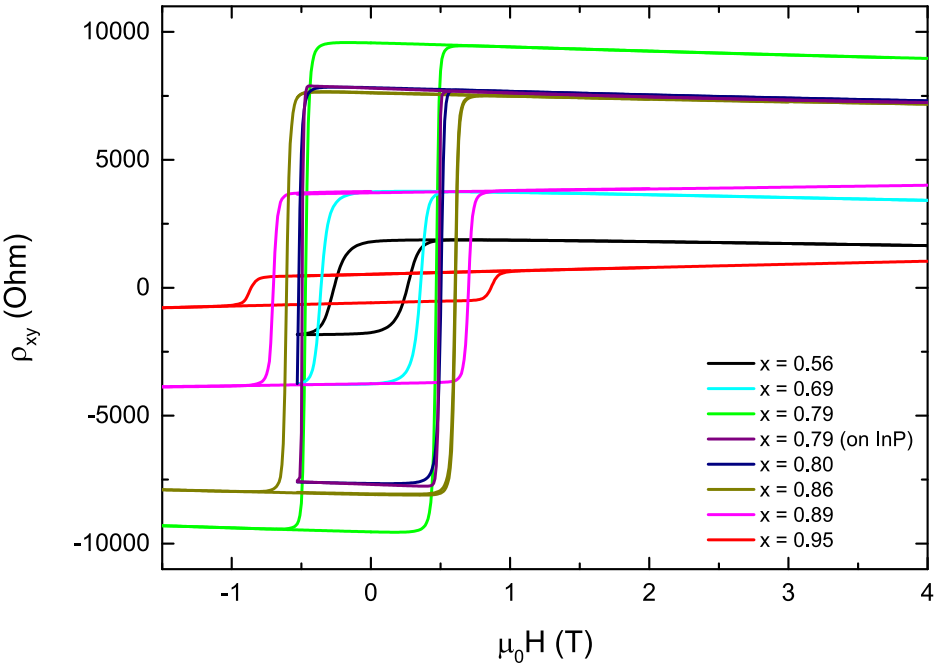

Fig. 4.20: Measurement of the anomalous hall effect at $T = 4.2$ K for $V_{0.1}(Bi_{1-x}Sb_x)_{1.9}Te_3$-layers grown at $T_{Sub} = 190°C$. The measurements were conducted at the gate voltage shown in the inset of fig. 4.18.

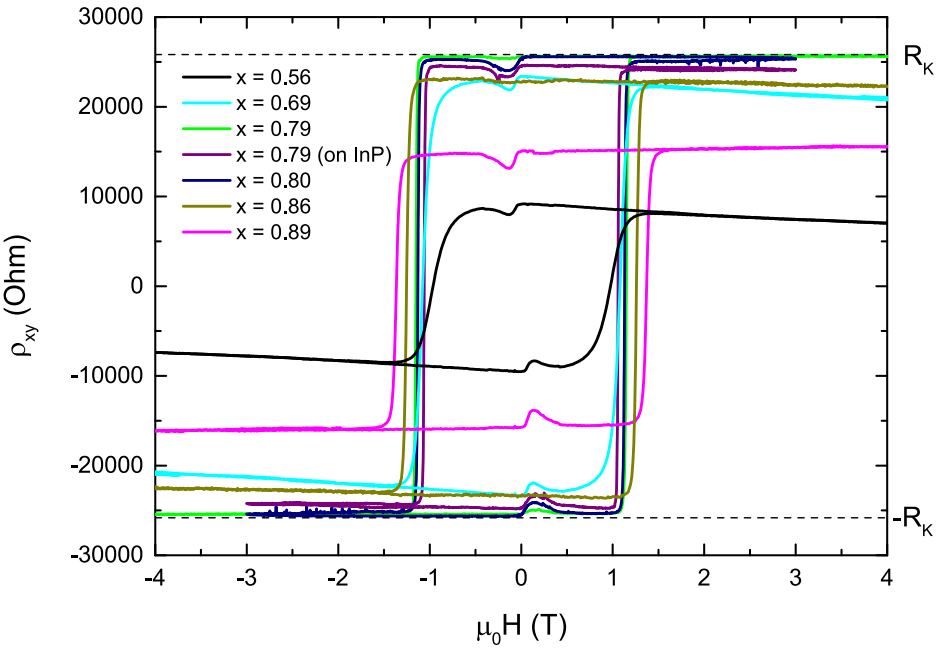

Fig. 4.21: Measurement of the anomalous hall effect at fridge base temperature for $V_{0.1}(Bi_{1-x}Sb_x)_{1.9}Te_3$-layers grown at $T_{Sub} = 190°C$. The measurements were conducted at the gate voltage shown in the inset of fig. 4.18. The dashed lines represent the von Klitzing constant, R_K and -R_K.

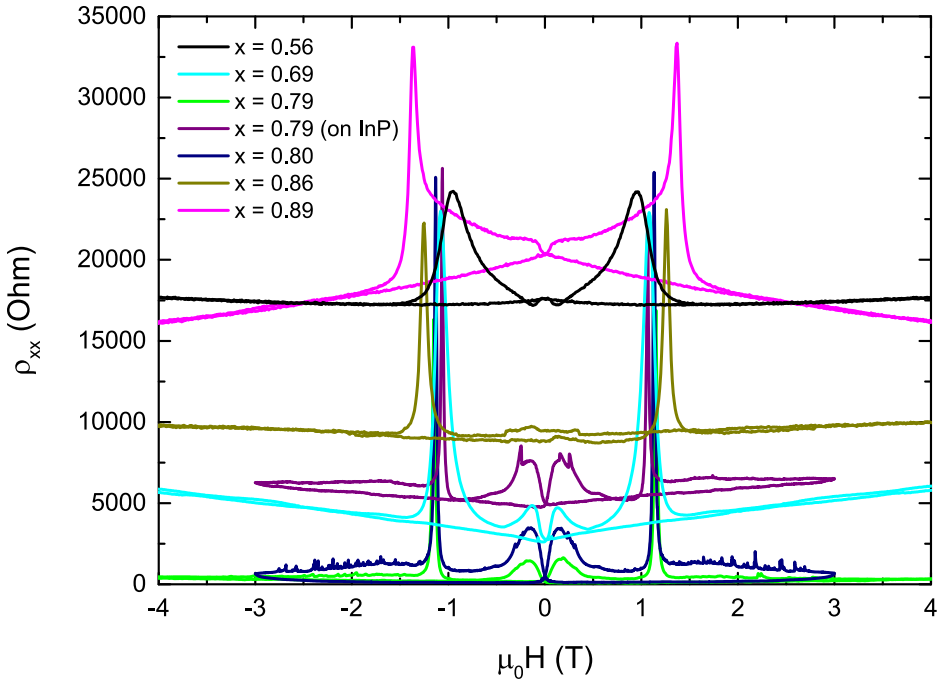

Fig. 4.22: Measurement of the longitudinal resistance at fridge base temperature for $V_{0.1}(Bi_{1-x}Sb_x)_{1.9}Te_3$-layers grown at T_{Sub} = 190°C. The measurements were conducted at the gate voltage shown in the inset of fig. 4.18.

Since the measurement is done by applying an ac bias voltage the small deviations can be explained by the capacitive coupling of the cryostat leads to the ground. The composition is actually close to the one of the investigated Cr-doped samples, but the result, a larger R_{AHE} and a lower ρ_{xx} at a larger layer thickness, show the advantage of V-doping over Cr-doping.

The Bi to Sb ratio for which the QAHE can be achieved is rather narrow as for samples with higher or lower values of x, ρ_{xy} no longer reaches quantization at millikelvin temperatures with $\rho_{xy} = 0.91$ R_K and $\rho_{xy} = 0.88$ R_K for $x = 0.69$ and $x = 0.86$ respectively. The layer grown on InP(111) with $x = 0.79$ is close to the quantized conditions as well with $\rho_{xy} = 0.95$ R_K indicating that the QAHE is not strongly dependent on the substrate condition.

Interestingly the value of H_c depends on the Sb content in the layers as well. It can be seen in fig. 4.19 that the coercive field increases with x in the probed range. This indicates a relation between Sb and the magnetism in the layer, Sb enhances the exchange interaction. By increasing the Sb-content the band gap of the compound decreases, the Dirac-point moves to higher energies and the carrier

concentration changes from n-type to p-type [90]. If the smaller band gap leads to an enhancement of the Van Vleck ferromagnetism, the change in the amount of carriers, albeit localized at millikelvin temperatures, increases the exchange interaction, the movement of the Dirac-point, the difference in the atomic orbitals of Bi and Sb or an entirely different reason is the cause for the relation is unknown at this point.

4.4 The quantum anomalous hall effect

After the discovery of the QHE the question arose if a quantized conductance and edge channel transport can be achieved without the necessity of an external magnetic field [140], the QAHE. Recently the QAHE has been proposed in 2D ferromagnetic metals [141], in $Hg_{1-y}Mn_yTe$ quantum wells [112], in graphene with Rashba and exchange effects [142] and in ferromagnetic TI materials like magnetically doped Bi_2Se_3, Bi_2Te_3 and Sb_2Te_3 [113, 143]. In Cr- and V-doped $(Bi_{1-x}Sb_x)_2Te_3$ it was realized [18, 129–135].

In their proposal for the QAHE in Bi_2Se_3 and related materials Yu *et al.* [113] describe a mechanism based on a 2D ferromagnetic TI. The studied TI materials belong in principle to the class of 3D TIs, but it has been shown that by reducing the thickness to less than 6 nm, the wave functions of the surface states overlap and a hybridization gap opens [103, 104, 108]. Only edge states remain and the 3D TI becomes a 2D TI. In the 2D TI the two edge channels, one for each spin direction, flow clockwise and counterclockwise respectively, this is called the quantum spin Hall effect (QSHE). By introducing the exchange field of a ferromagnetic system the inversion of one of the two spin species is lifted and only a single spin-polarized edge channel remains. The QAHE is realized.
An alternative proposal by Nomura and Nagaosa [143] is based on magnetic 3D TIs. In their paper the effect of the exchange interaction on one surface state is studied. The exchange interaction opens a gap for the surface states and they localize. As long as the Fermi energy is in the gap the Hall conductivity of the surface state quantizes with $\sigma_{xy} = \pm e^2/(2h)$. For two surface states this would result in a total Hall conductivity of $\sigma_{xy} = \pm e^2/h$.

In the last section the optimization process towards the QAHE is described and now further results from measurements on $V_y(Bi_{1-x}Sb_x)_{2-y}Te_3$ from the sample closest to quantization, with $d = 9$ nm, $y = 0.1$, $x = 0.79$ and $T_{Sub} = 190°C$ during growth will be shown and discussed. Parts of this section are published [18]. Measurements were conducted on the large and small Hall bar and show qualitatively the same results. The same measurements were also done on another sample with $x = 0.80$, being fabricated otherwise in the same way, shown in fig. A.7 to fig. A.10 in the appendix, and confirm the presented results.
After cooling the sample to $T = 15$ mK and saturating the magnetization in a large enough negative magnetic field the dependence on the gate voltage of the resistance was measured, at a small external magnetic field to guarantee stable magnetization, and is displayed in fig. 4.23. For gate voltages in the range of $V_g = 8$ V to $V_g = 1$ V ρ_{xx} and ρ_{xy} are quite stable and near the expected values for quantization 0 and -R_K respectively. It is concluded that in this region charge neutrality is achieved and only a single edge channel contributes to the transport. The center of this gate voltage region, $V_0 = 4.5$ V is chosen as the gate voltage for further measurements in the QAHE-regime. For negative gate voltages the resistivities move off from their quantized values presumably because of the availability of additional conductance channels.

A magnetic field sweep was done at V_0, as shown in fig. 4.24, and the switching of ρ_{xy} from -R_K to +R_K at $\mu_0 H_c \approx 1.1$ T due to a reversal in the magnetization can be seen. The magnetic switching is accompanied by a large longitudinal resistivity because in this region the edge channel transport breaks down. Just after crossing $\mu_0 H = 0$ there is a noticeable bump in the resistivities which will be discussed later. Both the resistivities and conductivities are at their expected quantized value almost independent of the external magnetic field. At $\mu_0 H \gtrsim 0$, just before the bump, the values of the resistivities and conductivities are $\rho_{xx} = 0.005$ R_K, $\rho_{xy} = 0.9996$ R_K, $\sigma_{xx} = 0.005$ e^2/h and $\sigma_{xy} = 1.0003$ e^2/h. The small deviations to the quantized values can be explained by the capacitive coupling of the cryostat leads to the ground for the ac-measurement with a frequency of 13 Hz. Quantization at zero external magnetic field is achieved.

So far it is shown that the values for the resistivities and conductivities quantize, but a conclusive proof for the chiral edge channel nature of the electrical transport is missing. This proof can be given by non-local measurements. In a

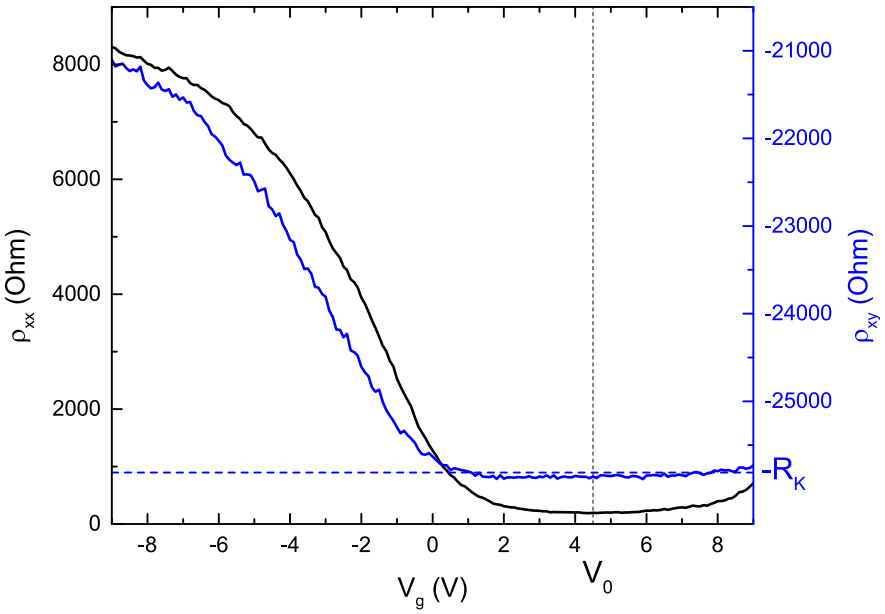

Fig. 4.23: Measurement of the gate voltage dependence of ρ_{xx} (black) and ρ_{xy} (blue) on the described layer at $T = 15$ mK and $\mu_0 H = -0.2$ T. Quantization conditions are achieved in a range from $V_g = 8$ V to $V_g = 1$ V and $V_0 = 4.5$ V is chosen for further measurements in the QAHE-regime.

non-local measurement it can be shown that the actual current path in the sample differs from the, for diffusive transport, expected one. In the measurement in fig. 4.25 a current, I_{16} is flowing from contact 1, where a voltage is applied, to contact 6, which is grounded, and a voltage is measured between the contacts 1 and 6, U_{16} and between 4 and 6, U_{46}. Then the resistances are calculated with $R_{16,16} = U_{16}/I_{16}$ and $R_{46,16} = U_{46}/I_{16}$. The position of the Hall bar contacts is indicated in the schematic drawing in the upper left corner of fig. 4.25.

For a chiral edge channel with non-dissipative transport there are in principle only two possible results for this measurement. If the current flows clockwise in the Hall bar the potential at contacts 2, 3, 4 and 5 is equal to the potential at contact 1 and therefore $U_{46} = U_{16}$ and $R_{46,16} = R_{16,16}$. If the current flows counterclockwise the potential at the contacts 2, 3, 4 and 5 is equal to the potential at contact 6 and therefore $U_{46} = 0$ and $R_{46,16} = 0$.

If the edge channel transport does not dominate the transport the potential at contact 4 depends on the sample geometry and the relation between hall and longitudinal conductivity and neither $R_{46,16} = R_{16,16}$ nor $R_{46,16} = 0$ can be achieved. The shown measurement in fig. 4.25 clearly supports the picture of edge channel

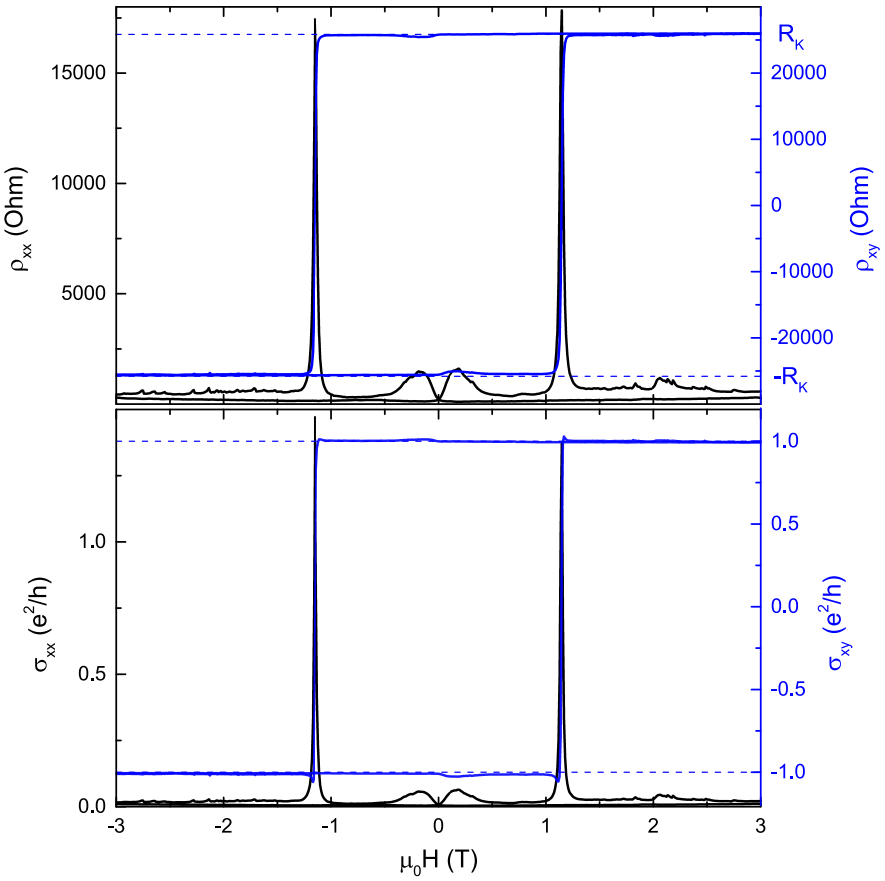

Fig. 4.24: Magnetic field sweep at $T = 15$ mK and V_0. Hall (blue) and longitudinal (black) resistivity as well as conductivity are shown to demonstrate the accuracy and stability of the quantization of the QAHE in this layer. At about 1.1 T the magnetization of the sample changes.

transport. In the left part of the figure the current flows first counterclockwise, $R_{46,16} = 0$, best fulfilled at $\mu_0 H \lesssim 0$, and upon increasing the magnetic field the magnetization switches and the current flow switches its direction as well to clockwise, $R_{46,16} = R_{16,16}$. Upon decreasing the magnetic field in the right part of the figure the magnetization and current flow switch back to their previous states. For perfect edge channel transport the two terminal resistance should in principle be always at the quantized value, $R_{16,16} = \mathrm{R_K}$, but for the used Hall bar the contact resistance and the not gated part cause deviations.

After proving the existence of the edge states the already mentioned bump in the magnetoresistance after crossing zero external field will be discussed. In the upper part of fig. 4.26 a minor hysteresis loop is shown. The magnetic field is swept

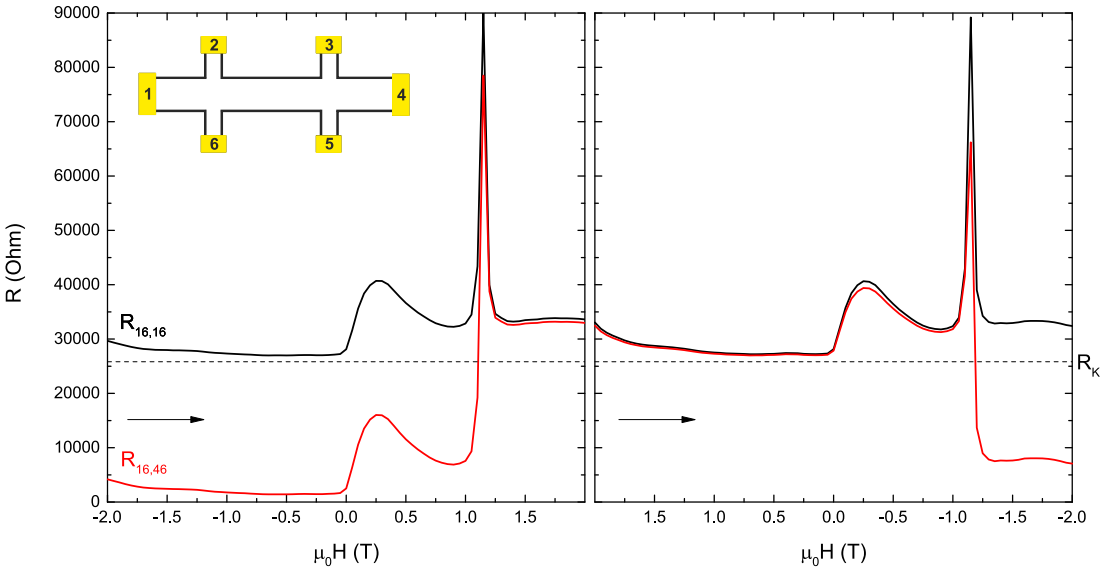

Fig. 4.25: Measurement of a two-terminal and a non-local resistance, $R_{16,16}$ (black) and $R_{16,46}$ (red), on the sample at $T = 15$ mK and V_0. The position of the contacts on the Hall bar is shown by the schematic drawing in the upper left corner of the left figure. For both figures the magnetic field is swept in direction of the x-axis, as indicated by the arrows.

up from negative saturation until the bump is completely resolved at $\mu_0 H \approx 0.8$ T and then back to negative saturation again. In both directions the bump is present proving its hysteretic nature. For the internal magnetic field in the sample, $B = \mu_0 H + M$, the crossing of $H = 0$ holds no special meaning and therefore should not cause any features. This indicates that the sample cannot be viewed as a single macrospin-like ferromagnet and rather has components which are not or only weakly coupled to the rest of the sample which is responsible for the main switching event.

In the lower part of the figure the evolution with temperature of the feature is shown. It is still present at $T = 530$ mK, where the sample is already way off quantization but no longer present at $T \approx 1$ K, still far away from the Curie temperature of the layer, $T_C = 26$ K, as determined by a SQUID-measurement. This indicates that the feature is neither caused by the edge channel transport nor has the same origin as the main magnetization. In the inset a time dependence of the hall resistivity is shown. This data was taken by sweeping the magnetic field at $T = 15$ mK from negative saturation to the point indicated by the black circle in the lower part of fig. 4.26 at $\mu_0 H = 0.12$ T. It can be seen that the feature is

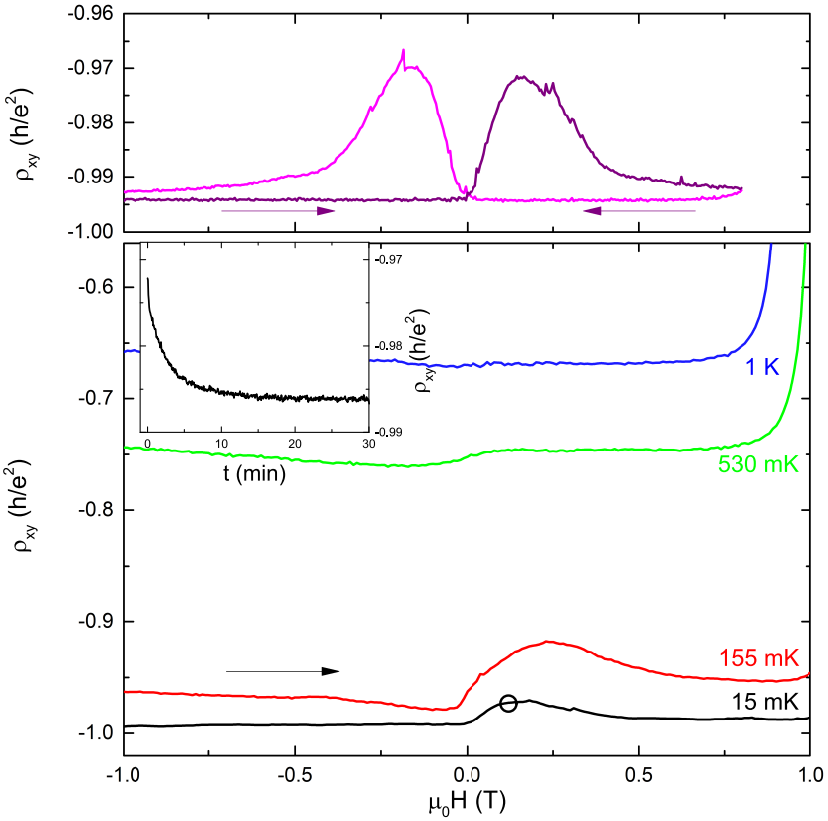

Fig. 4.26: Measurements of the feature after crossing zero external magnetic field. In the top part the hysteretic nature of the feature is shown by sweeping the field at $T = 15$ mK from negative saturation to a point just after the zero field feature and then back again. In the lower part of the figure the feature is measured for different temperatures as indicated in the graph. In the inset of this figure the evolution in time of ρ_{xy} after sweeping the external magnetic field only to the point indicated by the black circle at $T = 15$ mK is shown.

not stable in time but evolves over a time scale of minutes. It relaxes back in the direction of quantization but only partially, i.e. not completely to the baseline of this measurement. This overall behavior points to a superparamagnetic nature of this feature developing below 1 K. The zero field feature is visible as well on samples with different Sb-content at millikelvin temperatures and can be seen in fig. 4.21.

It should be noted that a feature after crossing zero external magnetic field was also, albeit not discussed, observed in other publications. A bump is clearly visible for ρ_{xx} in fig. 2b of [130] and fig. 1b of [131] and can indeed also be seen in ρ_{xy} in [131], even though the amplitude of the feature is small in this case.

A time dependence of the hall resistivity was already observed in a previous section on Cr-doped layers and was attributed to superparamagnetism as well. That the same behavior emerges in these similar layers seems to be not unlikely. The zero field feature is not the only unusual one observed in this sample. In fig. 4.27 another one is presented. After switching the magnetization one can observe spikes in the magnetoresistance. The reason why these spikes are not present in the other shown measurements is that in this specific measurement the magnetic field was swept very slow and continuously, with 20 mT/min, and the magnetoresistance is measured while sweeping the magnetic field. In contrast for all other measurements a short amount of time was waited for the magnetic field to settle before acquiring a measurement point. These spikes apparently only appear immediately after changing the magnetic field and are attributed to a sudden change in the magnetization in small parts of the sample, which are not magnetically stable. These in turn generate stochastic jumps in the hall and in the longitudinal resistivity. The field value at which they appear is random, but the region does reproduce in repeated measurements and only at large enough fields $\mu_0 H \gtrsim 3$ T the spikes in the magnetoresistance stop to appear. After changing the sweep direction and going back in field they are not present.

The measurement in fig. 4.28, here for a different sample also in the QAHE regime, supports the interpretation of a magnetic origin. In this case the magnetization was saturated for negative fields only up to a certain amount, from just after the main switching event at -1.3 T to the maximum magnetic field of the magnet at -16 T. It can be clearly seen that the appearance of the spikes depends on the previous saturation field. From none at a saturation field of -1.3 T the amount increases till -3.0 T and for -16 T the amount does not increase anymore. The higher the absolute value of the saturation field the denser the spikes get. This is consistent with a magnetic origin of the spikes. If the negative saturation field is not high enough the unstable magnetic parts still are in their configuration for a positive magnetization and will not switch and cause spikes upon increasing the field.

Another peculiar feature can be observed upon warming the sample. Before warming the sample up it was prepared by saturating at a positive field and then performing the measurement at $\mu_0 H = 0.5$ T to avoid influence of the feature at zero field. Afterward it was cooled again. In fig. 4.29 the resulting temperature

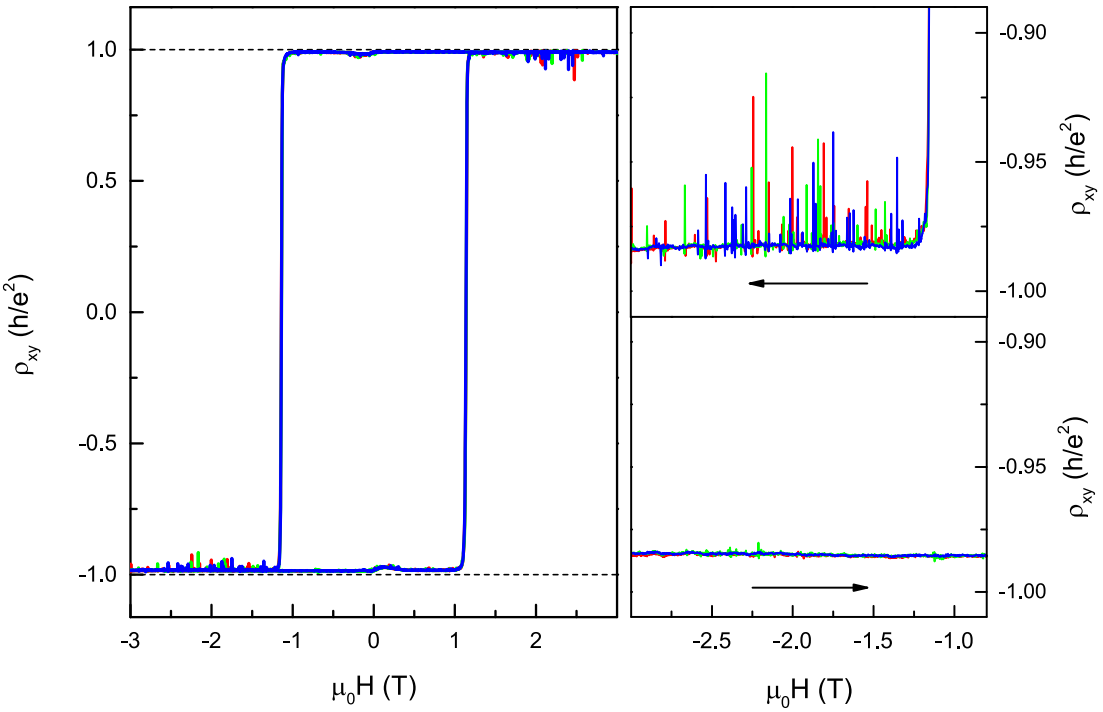

Fig. 4.27: In the left part of the figure several magnetic field sweeps under identical conditions, $T = 15$ mK and $V_g = V_0$ are shown and spikes in ρ_{xy} are visible. In the upper right and lower right part a zoom-in for the different sweep directions as indicated by the arrow is shown. After switching the magnetization spikes appear which are not present when going back in magnetic field. The exact magnetic fields at which spikes appear seem to be random as they differ for each measurement.

dependence of ρ_{xy} is shown. The cooling curve shows a continuous increase of ρ_{xy} until about $T = 50$ mK where the quantized value is reached. The warming curve on the other hand looks completely different. Already at temperatures below 50 mK ρ_{xy} drops considerably to a lower value. The sudden jump in ρ_{xy} repeats during the warming and it is observed that it often coincides with a previous change of the heater power seen in the warming rate of the fridge displayed in the upper part of fig. 4.29. The correlation between changes in the warming rate causing jumps in ρ_{xy} is not one to one perfect, between 0.1 K and 0.2 K there is a change in warming rate without a jump, but is too strong to be a coincidence. This again suggests an unstable magnetic state, where this time the instability is caused by a temperature change. The larger the rate of the temperature change the larger the instability which reflects in ρ_{xy}.

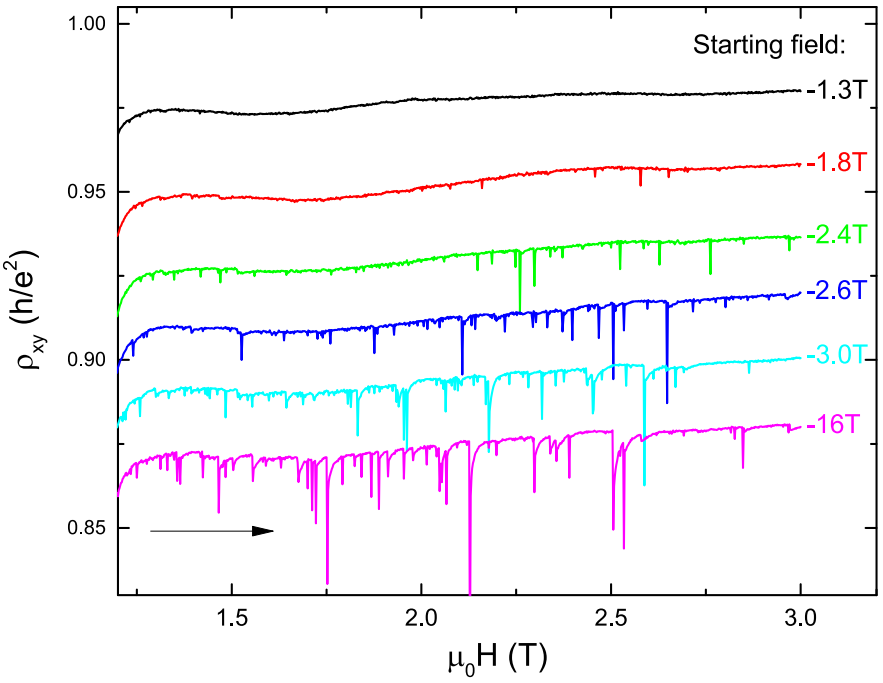

Fig. 4.28: This measurement was taken for another sample, with the only difference to the previous one being $x = 0.80$, at $T = 15$ mK and $V_g = V_0^{'}$. Gate voltage and magnetic field dependence look qualitatively the same as the ones shown (see fig. A.7 and fig. A.8 in the appendix). Again as in the previous figure the external magnetic field dependence after the switching event is shown. For each of the measurements the field was previously only saturated up to the indicated magnetic field. For clarity the curves are vertically shifted.

Overall quantized edge channel transport and the realization of the QAHE is proven and exemplary shown for one sample, but still there remain unresolved issues regarding the magnetization of the layer. Several features in the magnetoresistance like the zero field feature, spikes in the magnetoresistance and jumps of the magnetoresistance during warming are shown and discussed. These are interpreted as signs of magnetic instability and superparamagnetism.

In this chapter magnetic doping in the topological insulator material $(Bi_{1-x}Sb_x)_2Te_3$ is investigated, with the purpose of realizing the QAHE. The perpendicular-to-plane ferromagnetism at low temperatures in layers doped with the transition metal Cr is confirmed by SQUID measurements with even thin layers showing a perpendicular-to-plane magnetization. In electrical transport experiments on these layers the anomalous Hall effect was measured and a

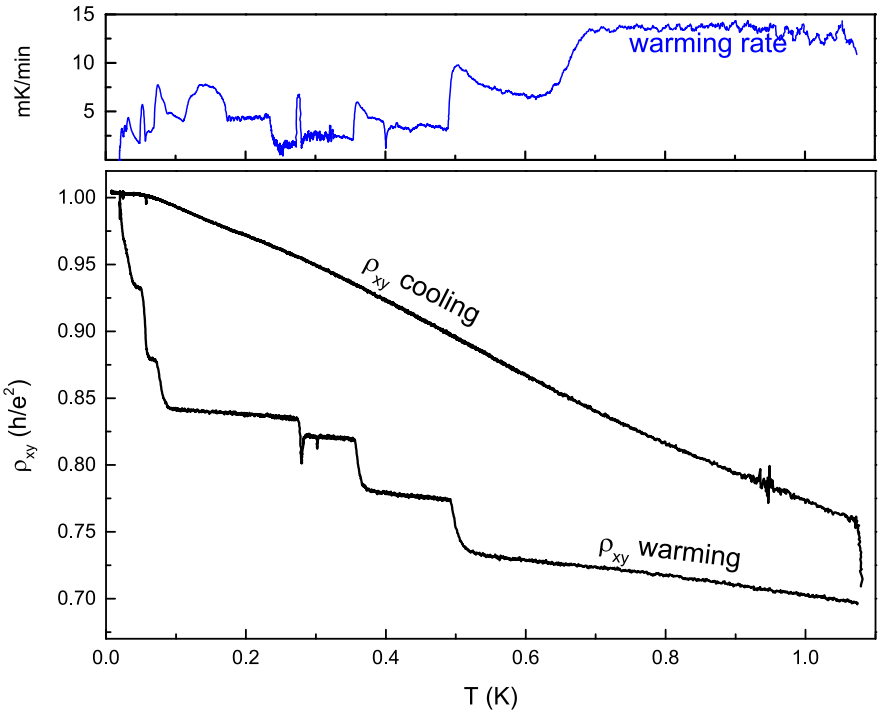

Fig. 4.29: In the lower part of the figure the temperature dependence of ρ_{xy} during cooling and warming at V_0 and $\mu_0 H = 0.5$ T is displayed. The upper part shows the rate of the temperature change of the fridge during warming. It can be seen that the sudden drops in ρ_{xy} coincide with changes of the warming rate.

large value for R_{AHE}, a prerequisite for the QAHE, was achieved for thin layers at low temperatures, but only in combination with a large ρ_{xx}. Even insulating behavior and variable range hoping like transport were observed for very thin layers. The largest achieved values of R_{AHE} are still far from quantization.
Additionally the magnetization of the layers was studied by monitoring R_{AHE}. It was observed, that the magnetization is not stable in time. Even at temperatures as low as 1.6 K and at constant zero external magnetic field the value of R_{AHE} which is assumed to be proportional to M relaxates over time. This is a characteristic of superparamagnetism, an effect caused by small ferromagnetic particles which still can change their magnetization spontaneously. The average particle size is determined by the time dependence of the anomalous hall resistance.
For a more systematic study Cr was replaced with V, which from its electronic configuration resembles Bi and Sb more closely. The observed magnetism is more stable with coercive fields up to about 1 T. After optimizing the fabrication in

regards to substrate temperature, V-content and most importantly Sb-content, the QAHE was realized and studied at millikelvin temperatures. A quite surprising result regarding the far from perfect crystal quality of the layer and the absence of the QSHE or distinctive surface state transport in non-magnetic layers.
The quantization to the literature values is accurate considering the inherent measurements errors and the edge channel nature of the transport is shown by non-local measurements. Even in these layers in the QAHE regime signs of magnetic instability were found, a feature after crossing zero external magnetic field, spikes after the switching event and jumps in the resistance upon warming the sample. The zero field feature also shows a dependence on time connecting it to the in the Cr-doped layers observed superparamagnetism.

The QAHE in TIs is an interesting system combining magnetism with spin polarized edge channel transport. The possibilities offered by such a system can now be studied in the V-doped $(Bi_{0.21}Sb_{0.79})_2Te_3$ layers.
One of these is the potential to be the host of a Majorana bound state [144], useful for quantum computing. If the QAHE is coupled to a conventional superconductor trough the proximity effect a chiral topological superconductor which carries a single Majorana zero mode is generated.
Additionally the possibility to realize a switch of the magnetization by a current might be given in the QAHE regime. A different magnetization of the material in lateral direction could be realized by etching the layer in different regions by different amounts, thus creating different coercive fields. The spin torque by the spin polarized current through the edge channel could then be able to switch the different regions to the same magnetization direction.
It was shown that the QAHE can also be realized in multi-layer systems of $(Bi_{1-x}Sb_x)_2Te_3$ [145], e.g. a non-magnetic layer sandwiched between two magnetic layers. If one can manage to get two distinct coercive fields for the two magnetic layers a separate switching of them is possible and a configuration where they are anti-parallel magnetized can be realized. In such a configuration for a 3D system a true zero Hall plateau should emerge and the detection of the quantized topological magneto-electric effect, where an electric field generates a magnetization in the same direction [146], is proposed [147].

Chapter 5

Axionic Screening in the Scaling of the Quantum Anomalous Hall Effect

Besides the various exotic properties of TIs which were to some extent investigated in the previous chapters there is another one which connects an external magnetic field to the magnetic polarization in a 3D TI with $\vec{M} = \alpha\vec{E}$ [146, 148], $\alpha = \frac{e^2}{h}$ being the fine structure constant: the so called topological magneto-electrical effect (TME). An exciting consequence of this effect is the predicted existence of a magnetic monopole in a TI, where an electrical charge near the surface induces an image magnetic monopole [13]. The field theory for the TME can be described by adding an additional term to the electromagnetic Lagrangian $\mathcal{L}$ [146]:

$$\Delta\mathcal{L} = \theta\frac{\alpha}{4\pi^2}\vec{E}\cdot\vec{B}\ , \tag{5.1}$$

with $\theta = \pi$ in the case of a 3D TI.

The term in eq. 5.1 has an analogon in axion electrodynamics [149, 150]. The axion being a hypothetical elementary particle originally proposed as a resolution to the absence of violation of charge parity symmetry in strong interactions [151]. So far there are indications for its existence [152, 153] but it still remains to be proven. The equivalence of the term in eq. 5.1 leads to the expectation of the existence of axions in 3D TIs which cause the TME. Recently this has been investigated through Faraday and Kerr rotation [154–156], but the interpretation

remains difficult because both TI surfaces are being observed simultaneously. Due to the axionic term at the TI boundary the single Dirac cone surface state does not violate gauge symmetry upon minimal coupling to an electromagnetic field [157, 158]. For the, in the previously chapter studied, ferromagnetic TIs the magnetic dopants induce a gap and a half integer quantized Hall conductivity, $\sigma_{xy} = \pm\frac{e^2}{2h}$ should be observable for each of the individual surface states while the Fermi energy is in the bulk gap. An observation of the QAHE in a 3D TI can thus be regarded as the realization of an "axion insulator". But, because the conductivities of the two parallel surface states add up, it is not directly observable in a transport experiment. Still there is a way to detect this unique behavior by studying the scaling behavior of the longitudinal and traversal conductivities [143].
In this chapter, results of measurements on TIs in the QAHE-regime at dilution fridge temperatures are presented, the scaling behavior is analyzed and compared to other published results. The content of this chapter is published in [159].

5.1 Scaling in the quantum anomalous hall effect

In previously shown figures, such as in the lower part of fig. 4.24, it can be seen that the edge transport in the QAHE-layers switches from $n = +1$ to $n = -1$ upon reversing the magnetization, accompanied by a peak in σ_{xx}. In the transition region where the edge channel transport changes σ_{xx} and σ_{xy} are in fact not independent of each other and their scaling behavior can be described by a flow diagram relating σ_{xx} to σ_{xy}. This behavior has already been extensively studied for the integer QHE [160–164].
In the QHE each plateau transition is described by a semicircle connecting the stable fixed points $(\sigma_{xy}, \sigma_{xx}) = (n\ e^2/h, 0)$ to each other [165–167] with the center of the semicircle being $(\sigma_{xy}, \sigma_{xx}) = ((n - 1/2)\ e^2/h, 0)$ and the radius $e^2/(2h)$. The series is finally terminated by the transition to an insulator, from $n = 1$ to $n = 0$, still following the relation described by the semicircle [168]. It should be noted that for each point on one of these ideal semicircles, excluding $(\sigma_{xy}, \sigma_{xx}) = (n\ e^2/h, 0)$, ρ_{xy} is actually at its quantized value, $\rho_{xy} = 1/n\ R_K$.
The first experimental study of the flow diagram in the QAHE was done by

Checkelsky *et al.* [129] and the obtained relation follows the semicircle from $(\sigma_{xy}, \sigma_{xx}) = (\pm e^2/h, 0)$ to $(0, 0)$. The conclusion is, as the authors point out, that the flow diagram of the observed QAHE is the same as for the QHE in an ordinary 2-DEG. Indeed when extracting the conductivities from magnetic field sweeps shown in other publications on the QAHE, for V-doped and Cr-doped $(Bi_{1-x}Sb_x)_2Te_3$, these systems show qualitatively the same flow diagram. This can be directly seen by the high peak value of $\rho_{xx} > h/e^2$ at $\rho_{xy} = 0$. Some examples of such a high peak value of the longitudinal resistivity in the literature are magnetic field sweeps with $\rho_{xx} = 2.2\ h/e^2$ in Fig. 2 of [12], $\rho_{xx} = 2.1\ h/e^2$ in Fig. 2 of [129], $\rho_{xx} = 1.7\ h/e^2$ in Fig. 1 of [134], $\rho_{xx} = 1.6\ h/e^2$ in Fig. 4 of [135], or even as high as $\rho_{xx} = 34\ h/e^2$ in Fig. 1 of [132]. The lowest peak values of the longitudinal resistivity is seen in Fig. 1 of [131] with $\rho_{xx} = 1.1\ h/e^2$ which, with a thickness of 10 nm, is measured on the thickest layer of the listed experiments, but as well the ordinary flow diagram is observed [131]. The, albeit small, indication of a thickness dependence in the literature fits quite well to the results which will be presented here. In contrast to these results for the surface state of a magnetic 3D TI a different flow diagram was proposed by Nomura and Nagaosa [143], similar to the behavior proposed for the Dirac system graphene [169]. The transition of a single surface state from $\sigma_{xy} = +e^2/(2h)$ to $\sigma_{xy} = -e^2/(2h)$, corresponding to the half-integer quantization $\sigma_{xy} = (n' + 1/2)\ e^2/h$ with $n' = 0$ and $n' = -1$, is studied. Again a semicircle like flow diagram is obtained but here the center is $(\sigma_{xy}, \sigma_{xx}) = (0, 0)$ with a radius of $e^2/(2h)$. If one considers now two parallel conducting surface states, e.g. top and bottom of a 3D TI, the conductivities add up and one gets a semicircle connecting the point $(\sigma_{xy}, \sigma_{xx}) = (e^2/h, 0)$ to $(\sigma_{xy}, \sigma_{xx}) = (-e^2/h, 0)$ with the center still being $(\sigma_{xy}, \sigma_{xx}) = (0, 0)$ and a radius of e^2/h.

Indeed this kind of flow diagram is observed for the first time in the previously described $V_{0.1}(Bi_{1-x}Sb_x)_{1.9}Te_3$-layers in this thesis, confirming that the QAHE stems from a 3D TI and therefore the presence of the axion term in the screening physics [143]. In fig. 5.1 the flow diagram of several V-doped layers of different Sb-content x, extracted from the magnetic field dependence, is displayed and it can clearly be seen that the relation of σ_{xx} to σ_{xy} follows the red dashed line, the semicircle representing two parallel conducting surface states. This is also reflected in ρ_{xx} in fig. 4.22 where the curves, which are at least close to

quantization, always have a maximum value below $\frac{h}{e^2}$ during the transition.

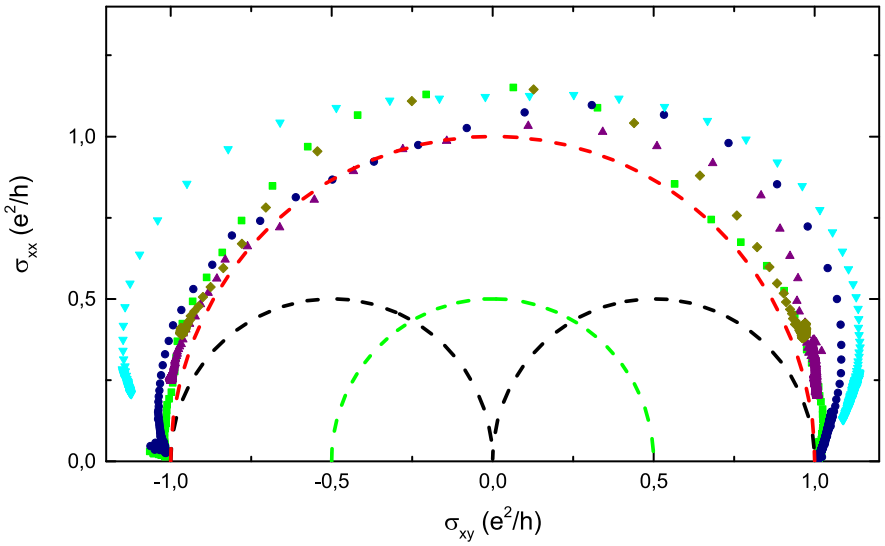

Fig. 5.1: The flow diagram mapping σ_{xx} to σ_{xy} of layers with $d \approx 9$ nm from the external magnetic field measurement with the Sb-content $0.69 \leq x \leq 0.89$ (see fig. 4.21 and fig. 4.22) is shown. The black dashed line represents the flow diagram of the iQHE, the green dashed line the predicted flow diagram of a single topological surface state and the red dashed line two parallel conducting topological surface states. The color code of the measurement data is the same as in the external magnetic field measurement in fig. 4.21.

In principle any parameter which affects the plateau transition, like temperature, gate voltage and external magnetic field, could have been used to investigate the scaling behavior. For the presented results the flow diagram is studied by changing the external magnetic field because it provides the largest coverage of the phase space while keeping the bulk insulating.

5.2 Influence of the layer thickness

Now a possible explanation for the two different scaling behaviors shall be explored, the thickness of the studied samples.
In publications the QAHE was measured on 5 nm $Cr_{0.15}(Bi_{0.1}Sb_{0.9})_{1.85}Te_3$ [12], 8 nm $Cr_{0.22}(Bi_{0.2}Sb_{0.8})_{1.78}Te_3$ [129], 5 nm $Cr_{0.23}(Bi_{0.4}Sb_{0.6})_{1.77}Te_3$ [132], 4 nm $V_{0.11}(Bi_{0.29}Sb_{0.71})_{1.89}Te_3$ [134], 4 nm V-doped $(Bi,Sb)_2Te_3$ [135] and 10 nm of $(Cr_{0.12}Bi_{0.26}Sb_{0.62})_2Te_3$ [131]. With the 10 nm layer being the thickest and, as already mentioned, also having the lowest longitudinal peak resistance. The here

presented results are on 9 nm thick layers, being thicker than most of the other stated layers. While the individual given results for the layer thickness probably vary slightly with the method by which they were determined, especially since the layers have a certain roughness for example from rotational twins [83], the difference in layer thickness is conspicuous. Furthermore the transition to the 2D case is determined to be at 6 nm [103, 104, 108] setting the published results, except of [129, 131], apart from the here presented ones. It might be the case that the thin layers fall in the category of 2D TIs and the presented 9 nm thick layers still belong to the class of 3D TIs.
To confirm the hypothesis, that indeed the layer thickness is significant, thinner layers were examined. Layers of 8 nm $V_{0.1}(Bi_{1-x}Sb_x)_{1.9}Te_3$ and 6 nm were grown and processed in the same way as the previous layers and measured as well at dilution fridge temperatures and at their respectively optimized gate voltage. The resulting hysteresis curves of ρ_{xy} and ρ_{xx} are shown in fig. 5.2 and inset.

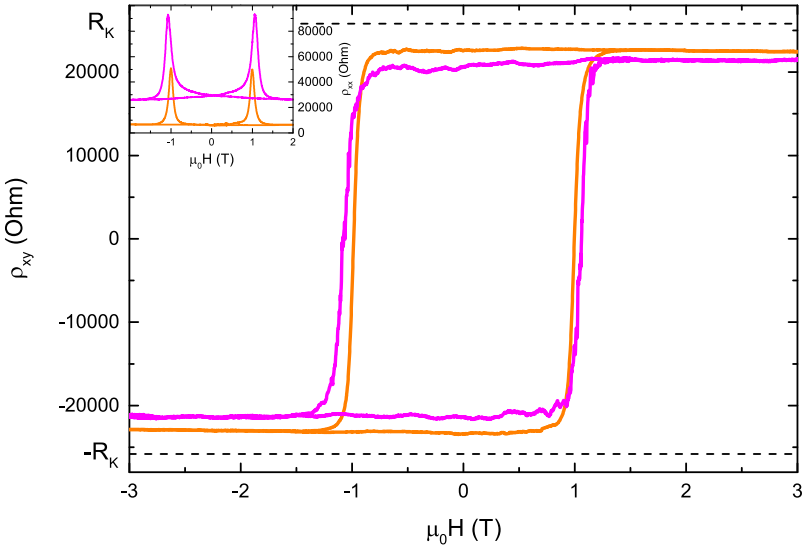

Fig. 5.2: QAHE in thinner magnetic TI layers. The measurements are on a layer with $x = 0.78$ and $d = 8$ nm (orange) and another layer with $x = 0.79$ and $d = 6$ nm (dary yellow). Both show a high anomalous Hall effect near the quantized value.

While the results indicate that there still is some fabrication optimization missing to achieve perfect quantization they are close enough to demonstrate the scaling behavior. In fig. 5.3 the flow diagram of the thin samples, and a thicker one of

similar composition for comparison, is plotted and indeed a change of the scaling towards the iQHE, with decreasing layer thickness, is observed. The 8 nm layer already shows a dip at $\sigma_{xy} = 0$ and for the 6 nm layer it gets more obvious and the flow diagram qualitatively follows the one for the iQHE represented by the black dashed lines. The axionic scaling of the 3D case transitions to the ordinary iQHE upon decreasing the thickness and therefore making the system more 2D-like. This confirms the crucial role of the layer thickness.

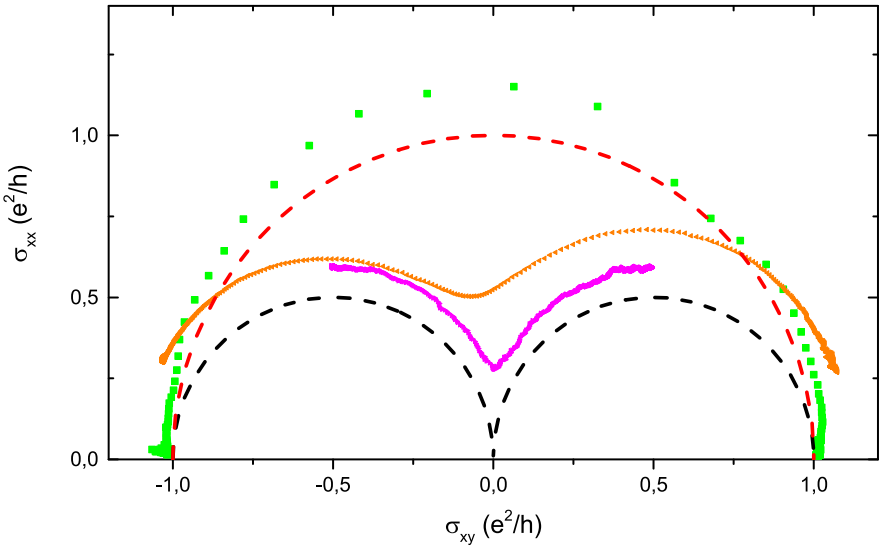

Fig. 5.3: Flow diagram of the transition of the QAHE for three different layers with $d = 9$ nm, $d = 8$ nm and $d = 6$ nm and similar composition. The black dashed line represents the flow diagram of the iQHE and the red dashed line two parallel conducting topological surface states.

5.3 Influence of the capping layer

Another aspect which has an influence on the scaling behavior is the existence or absence of a capping layer as protection against ambient conditions. So far the influence of the capping layer is unclear with the QAHE being reported for capped [129, 131, 134] as well as for uncapped layers [12, 130, 132]. During this work the QAHE has also been observed in the previously shown capped layers, but uncapped layers exhibit the QAHE as well. In fig. 5.4 a magnetic field sweep at dilution fridge temperatures and optimized gate voltage on uncapped $V_y(Bi_{1-x}Sb_x)_{2-x}Te_3$ layers is shown. Aside from the Te cap the layers were

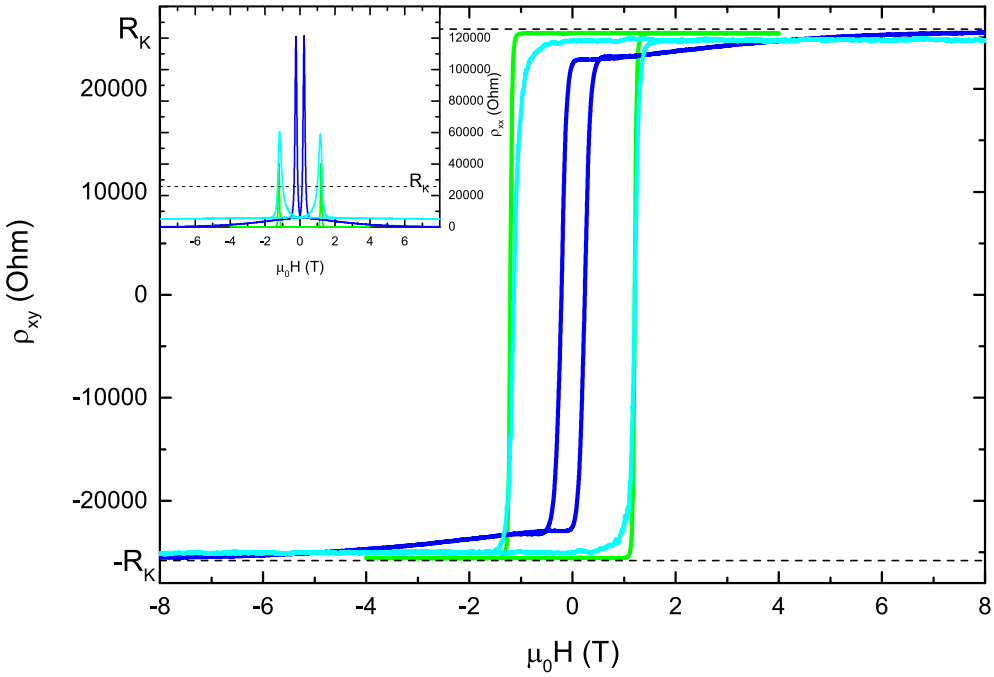

Fig. 5.4: Magnetic field sweep showing ρ_{xy} and ρ_{xx} in the inset of three uncapped V-doped layers at their optimized gate voltage and dilution fridge temperatures. The individual layers are: $V_{0.1}(Bi_{0.23}Sb_{0.77})_{1.9}Te_3$ with $d = 10$ nm (green), $V_{0.1}(Bi_{0.26}Sb_{0.74})_{1.9}Te_3$ with $d = 9$ nm (cyan), $V_{0.05}(Bi_{0.27}Sb_{0.73})_{1.95}Te_3$ with $d = 10$ nm (blue). The green curve is close to perfect quantization at zero field and the cyan one for the sample with less V quantizes at high magnetic fields.

fabricated and processed in the same way as capped layers and exhibit the QAHE as well.

For these uncapped samples the peak value of ρ_{xx} during the transition is above h/e^2. A first indication of a difference to the otherwise equivalent capped layers. This difference becomes more obvious when looking at the flow diagram, obtained from the shown magnetic field sweeps of these three layers, displayed in fig. 5.5. In

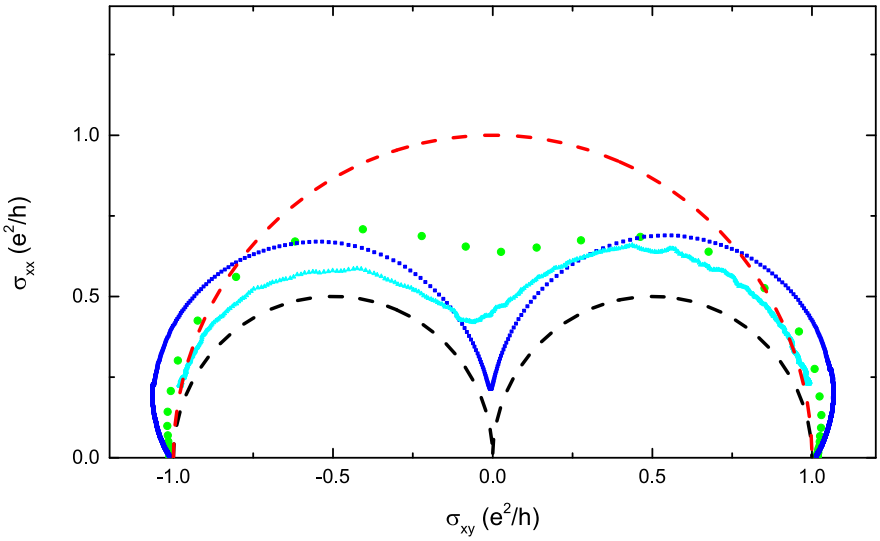

Fig. 5.5: Flow diagram of the transition of the QAHE for three uncapped layers from the magnetic field sweep shown in fig. 5.4 with the same color code. The black dashed line represents the flow diagram of the iQHE and the red dashed line two parallel conducting topological surface states.

the figure it can be clearly seen that the uncapped layers do not show the axionic 3D scaling but do qualitatively follow the 2D-like scaling behavior, represented by the black dashed line. The effect is most prominent for the blue curve which stems from a layer which also shows almost perfect quantization, albeit only at higher magnetic fields. It follows that the scaling behavior of uncapped samples is the same as for thinner capped samples. A likely explanation is a degradation in the topmost layers due to exposure of the, in this case unprotected, surface to ambient conditions and the lithography process, suggesting that uncapped samples have a dead layer at their surface, and thus are effectively thinner than their nominal values. Therefore this is a demonstration of the necessity of capping and protecting these kind of layers.

At last it should be pointed out that the predicted opening of the hybridization gap and therefore the transition from 3D to 2D behavior at 6 nm is not

necessarily in contradiction to the observed results. While most of the layers showing the 2D scaling behavior are at or below this threshold it can clearly be seen as well in layers of nominally 8 nm [129] or 10 nm [131] thickness as well. Considering that magnetically doped $(Bi,Sb)_2Te_3$ layers have a considerable roughness it may be that the percolation path of the edge channel through the sample contains thinner parts which could explain an onset of this behavior in nominally thicker samples.

By studying the scaling behavior relating σ_{xx} to σ_{xy} during the transition from one plateau to the other a previously not observed behavior is seen. From this scaling it is concluded that the QAHE in the capped 9 nm thick V-doped $(Bi,Sb)_2Te_3$ layers originates from the two topological surface states of the magnetic 3D TI with each surface contributing the half-integer quantization of $\sigma_{xy} = \frac{1}{2}e^2/h$ to the total Hall conductivity. As it is pointed out this result is fundamentally different from previously published measurements [1] and is therefore the first observation of the QAHE resulting from the axion term characterizing the electrodynamic response of a magnetic 3D TI.

[1] The external field dependence shown in Fig. 1 of a magnetic TI layer close to quantization by Kandala *et al.* has a peak value of $\rho_{xx} < e^2/h$ [133], but the implications of this behavior are neither discussed nor further investigated.

Chapter 6

Summary

This thesis presents results on investigations on 3D topological insulators. Materials of the so called second generation, Bi_2Se_3, $(Bi_{1-x}Sb_x)_2Se_3$ and $Bi_2(Te_{1-x}Se_x)_3$, and the magnetic topological insulators, $Cr_y(Bi_{1-x}Sb_x)_{2-y}Te_3$ and $V_y(Bi_{1-x}Sb_x)_{2-y}Te_3$, were studied. The goal of this work was to find evidence of the surface state in transport experiments and study the topological state. In this relatively new research field the main problem is the high unintentional doping despite a relatively large energy gap of up to 300 meV.

In the beginning of this work the focus was on reducing the bulk contribution in pure Bi_2Se_3, i.e. reducing the bulk carrier density as determined by magnetoresistance measurements at cryogenic temperatures. To achieve this, several adjustments to the fabrication of the layers were done, like growing under high Se-flux, the use of a nearly lattice matched substrate and growth on a rough substrate. These improvements resulted in a reduced carrier density by about a factor of ten, $2.1 \cdot 10^{18}$ cm^{-3} n-type, and an increase in the carrier mobility. Along with the reduction of the carrier density the Hall resistance started to show deviations from linearity and is described by a two carrier model. An unambiguous assignment of one of the carrier types to the surface state cannot be made.
For a further reduction alloying was tested with the materials $(Bi_{1-x}Sb_x)_2Se_3$ and $Bi_2(Te_{1-x}Se_x)_3$. For $Bi_2(Te_{1-x}Se_x)_3$ no significant improvements were accomplished, but for $(Bi_{1-x}Sb_x)_2Se_3$ a lower carrier density was achieved with $n_{total} = 4.5 \cdot 10^{17}$ cm^{-3} at $x = 0.44$.

Despite the advancements the bulk contribution to the transport is still dominating. Nevertheless several features in the magnetoresistance were found: linear magnetoresistance, weak anti-localization and Shubnikov-de Hass oscillations. These phenomenons were analyzed in respect to their possible origin. All of them might be explained as the consequence of a surface state but neither in a straightforward nor very compelling way. Overall the bulk as the origin of all these features is more likely.
Therefore no definite sign of a contribution of the surface state was found in the studied non-magnetic materials. Despite this progress it is fair to assume that for transport studies Bi_2Se_3 and the related materials remain far behind the already established topological insulator HgTe.

In contrast the magnetic doped versions are excellently suited for these studies. The effects of magnetic doping, namely with Cr and V, were investigated in $(Bi_{1-x}Sb_x)_2Te_3$. It is shown by SQUID measurements that even in thin layers a perpendicular-to-plane ferromagnetism is present. This offers the possibility to combine the topological surface state with magnetism making this material a promising host for the quantum anomalous Hall effect.
In Cr-doped layers a large anomalous Hall resistance was measured, but always accompanied by a large longitudinal resistivity.
The by far better alternative is V-doping which gives more promising results. After the successful optimization of the layer fabrication, with the Sb-content being most crucial, the quantum anomalous Hall effect is realized. Exact quantization of the Hall resistance was measured and the existence of an edge channel is proven by non-local measurements. This result is somewhat surprising since neither the quantum spin Hall effect, nor the quantum Hall effect, at moderate magnetic fields, is observed in the non-magnetic materials.
Even though the layers show a ferromagnetic signature in magnetic field sweeps, for instance measurements of the Hall effect display a hysteresis curve, the magnetism in these layers is not completely stable. This is most prominent in the Cr-doped layers where clear signs of superparamagnetism are observed. At zero external magnetic field and temperatures as low as 1.6 K the magnetization relaxes to zero over time, and even at millikelvin temperatures a decline in the Hall resistance is seen. In the V-doped layers signs of magnetic instability are,

even in the quantum anomalous Hall state, observed as well. They are not as distinctive but nevertheless present. This demonstrates that the magnetism in these materials is neither perfect nor fully understood.
Another observed characteristic relates to the yet unknown origin of the quantum anomalous Hall effect, which so far is only observed in thin layers, 4 nm to 10 nm thick. Either the two surfaces of the topological insulator are so close in the thin layers that they hybridize and the system becomes effectively a 2D topological insulator with an edge channel or the system is thick enough to remain 3D with two separated surface states and the small thickness is only needed to suppress other conductance channels. In the latter case the fact that for the Hall resistance the $n = \pm 1$ plateau is observed, despite being comprised of two surfaces, has to be related to half-integer quantization of the topological surface states. Intriguingly on this matter the presented results differ to the otherwise published data in literature. The flow diagram of the quantum anomalous Hall effect, describing the relation of σ_{xx} to σ_{xy} during the transition from one plateau to the other, obtained from published data from different groups resembles the behavior of the integer quantum Hall effect. The layers presented in this thesis deviate and exhibit a flow diagram which matches the predicted one for two topological surface states. This fundamental difference might be explained by the quantum anomalous Hall effect originating in the former case from a 2D state and in the latter from two separate surface states of a 3D topological insulator. A view supported by further measurements on thinner layers and on uncapped layers which transition to the ordinary flow diagram of the integer quantum Hall effect. Thus, for the first time, a clear observation of the "axion insulator" is established.

The quantum anomalous Hall effect in magnetically doped topological insulators provides a promising system for further investigations. Majorana bound states are predicted when combining superconductivity with the quantum anomalous Hall effect, useful for quantum computing. In trilayer systems, comprised of two magnetic layers with a non-magnetic layer in between, it might be possible to achieve two different coercive fields for the magnetic layers. For opposite magnetization a zero Hall plateau should emerge and the existence of the topological magneto-electric effect is predicted. Different coercive fields in lateral direction might enable a switching of the magnetization by driving a current in

the spin polarized edge channels, a foundation for the realization of spintronic devices.

In conclusion in non-magnetic Bi_2Se_3 and related materials no distinct sign of a surface state was found in transport. The bulk contribution to the transport dominates and after the extensive studies in this thesis and by other groups it is questionable if a realization of this material as a topological insulator is feasible. In contrast the results of this thesis on the magnetically doped systems are most promising. It was possible to localize the remaining bulk carriers at dilution fridge temperature, the quantum anomalous Hall effect is realized and for the first time transport in an "axion insulator" is observed. Thereby clear evidence of the surface is obtained and further options for fundamental research are given.

Chapter 7

Zusammenfassung

In dieser Dissertation werden die Ergebnisse von Experimenten an 3D topologischen Isolatoren dargestellt. Untersucht wurden Materialien der sogenannten zweiten Generation, Bi_2Se_3, $(Bi_{1-x}Sb_x)_2Se_3$ und $Bi_2(Te_{1-x}Se_x)_3$, sowie die magnetischen topologischen Isolatoren, $Cr_y(Bi_{1-x}Sb_x)_{2-y}Te_3$ und $V_y(Bi_{1-x}Sb_x)_{2-y}Te_3$. Das Ziel dieser Arbeit war, den Oberflächenzustand in Transportexperimenten nachzuweisen und diesen topologischen Zustand zu analysieren. Das Hauptproblem in diesem relativ neuen Forschungsgebiet besteht in einer hohen ungewollten Dotierung, welche trotz einer relativ großen Energielücke von bis zu 300 meV vorhanden ist.

Zu Beginn der Arbeit lag der Fokus auf der Reduktion des Volumenanteils am elektrischen Transport in reinem Bi_2Se_3, d.h. auf der Verkleinerung der Volumen-Ladungsträgerdichte, die mittels des Magnetowiderstands bei tiefen Temperaturen bestimmt wurde. Um die Reduktion des Volumenanteils zu erreichen, wurden mehrere Änderungen an der Herstellung der Schichten vorgenommen, wie das Wachstum unter hohem Se-Fluss, die Nutzung eines Substrats mit nahezu gleichen Gitterkonstanten und das Wachstum auf einem rauen Substrat. Diese Verbesserungen führten zu einer Verkleinerung der Ladungsträgerdichte um einen Faktor von circa zehn, $2.1 \cdot 10^{18}$ cm^{-3} n-typ, und einer Erhöhung der Mobilität der Ladungsträger. Einhergehend mit der Verkleinerung der Ladungsträgerdichte fängt der Hall-Widerstand an, eine Abweichung vom linearen Verhalten zu zeigen und wird im zwei Ladungsträger-Modell beschrieben. Eine eindeutige Zuordnung einer der Ladungsträgerarten

zum Oberflächenzustand konnte nicht festgestellt werden.
Zur weiteren Reduktion wurden Legierungen mit den Materialien $(Bi_{1-x}Sb_x)_2Se_3$ und $Bi_2(Te_{1-x}Se_x)_3$ getestet. Während für $Bi_2(Te_{1-x}Se_x)_3$ keine signifikante Verbesserung festgestellt wurde, wurde für $(Bi_{1-x}Sb_x)_2Se_3$ eine geringere Ladungsträgerdichte mit $n_{total} = 4.5 \cdot 10^{17}$ cm^{-3} für $x = 0.44$ erzielt.
Der Volumenanteil am elektrischen Transport ist trotz der Verbesserungen weiterhin vorherrschend. Es wurden dennoch verschiedene Besonderheiten im Magnetowiderstand gefunden: linearer Mangetowiderstand, schwache Anti-Lokalisierung und Shubnikov-de Hass Oszillationen. Diese Phänomene wurden auf ihre mögliche Herkunft analysiert. Sie könnten alle aus dem Oberflächenzustand resultieren, allerdings nicht unmittelbar oder auf sehr überzeugende Weise. Insgesamt ist das Volumen als Ursache für alle diese Merkmale wahrscheinlicher. Letztlich wurde kein eindeutiges Zeichen eines Beitrags des Oberflächenzustands zum elektrischen Transport in den untersuchten nicht magnetischen Materialien gefunden. Daher kann man trotz dieser Fortschritte annehmen, dass für Transportuntersuchungen Bi_2Se_3 und verwandte Materialien weit hinter dem bereits etablierten topologischen Isolator HgTe zurückbleiben.

Die magnetisch dotierten Versionen dieser Materialien sind im Gegensatz dazu für diese Untersuchungen hervorragend geeignet. Die Wirkung der magnetischen Dotierung mit Cr und V wurde in $(Bi_{1-x}Sb_x)_2Te_3$ untersucht. Es wurde in SQUID Messungen beobachtet, dass sogar in dünnen Schichten Ferromagnetismus mit einer Ausrichtung senkrecht zur Oberfläche vorhanden ist. Dies bietet die Möglichkeit, den topologischen Oberflächenzustand mit Magnetismus zu kombinieren, was dieses Material zu einem vielversprechenden Kandidaten für den Quanten-anomalen-Hall-Effekt macht.
In Cr-dotierten Schichten wurde ein großer anomaler Hallwiderstand gemessen, jedoch immer in Kombination mit einem ebenfalls großen Längswiderstand.
Die bei weitem bessere Alternative sind V-dotierte Schichten, die vielversprechendere Resultate zeigen. Nach der erfolgreichen Optimierung der Herstellung, mit dem Sb-Gehalt als wichtigstem Parameter, wurde der Quanten-anomale-Hall-Effekt nachgewiesen. Die exakte Quantisierung des Hallwiderstands wurde gemessen und die Existenz des Randkanals mittels nicht-lokaler Messungen gezeigt. Dieses Ergebnis ist einigermaßen überraschend, da bisher weder der

Quanten-Spin-Hall-Effekt noch der Quanten-Hall-Effekt, bei moderaten magnetischen Feldern, in den nicht magnetischen Materialien beobachtet wurden.
Obwohl die Schichten im Magnetfeld ferromagnetische Charakteristika zeigen, wie zum Beispiel eine Hysterese im Hall-Effekt, ist dieser Magnetismus nicht komplett stabil. Dies zeigt sich am deutlichsten in Cr-dotierten Schichten, bei denen klare Anzeichen von Superparamagnetismus beobachtet wurden. Bei einem externen magnetischen Feld von null und Temperaturen von bis zu 1.6 K geht die Magnetisierung mit der Zeit gegen null und selbst bei millikelvin Temperaturen wurde ein Abfall des Hallwiderstands gemessen. In V-dotierten Schichten wurden ebenfalls Zeichen von magnetischer Instabilität, sogar im Quanten-anomalen-Hall-Zustand, beobachtet. Sie sind nicht so ausgeprägt aber dennoch vorhanden. Dies zeigt, dass der Magnetismus in diesen Materialien weder perfekt noch vollständig verstanden ist.
Ein weiteres beobachtetes Merkmal bezieht sich auf den noch ungeklärten Ursprung des Quanten-anomalen-Hall-Effekts, der bisher nur in 4 nm bis 10 nm dünnen Schichten gemessen werden konnte. Entweder befinden sich die beiden Oberflächen des dünnen topologischen Isolators so nahe beieinander, dass sie hybridisieren und das System effektiv 2D mit einem Randkanal wird, oder das System ist dick genug, um 3D mit zwei getrennten Obflächenzuständen zu bleiben, und die dünne Schichtdicke wird lediglich benötigt um andere Leitungskanäle zu unterdrücken. In letzterem Fall muss die Tatsache, dass für den Hallwiderstand, obwohl er aus zwei Oberflächen besteht, Plateaus mit $n = \pm 1$ beobachtet werden mit der halbzahligen Quantisierung des topologischen Oberflächenzustands zusammenhängen. Interessanterweise unterscheiden sich diesbezüglich die hier gezeigten Ergebnisse von sonstigen publizierten Daten in der Literatur. Das Flussdiagramm des Quanten-anomalen-Hall-Effekts, welches die Beziehung von σ_{xx} zu σ_{xy} während des Übergangs von einem Plateau zum anderen beschreibt, gleicht bei veröffentlichten Daten anderer Gruppen dem Verhalten des ganzzahligen Quanten-Hall-Effekt. Die in dieser Dissertation untersuchten Schichten unterscheiden sich davon und das Flussdiagramm stimmt mit dem für zwei topologische Oberflächenzustände vorhergesagten überein. Dieser fundamentale Unterschied könnte dadurch erklärt werden, dass der Quanten-anomale-Hall-Effekt im ersten Fall von einem 2D Zustand ausgeht und im letzteren von den zwei getrennten Oberflächenzuständen eines 3D

topologischen Isolators. Diese Interpretation wird durch weitere Messungen an dünneren Schichten und ungedeckelten Schichten, welche zum gewöhnlichen Flussdiagramm des ganzzahligen Quanten-Hall-Effekts übergehen, gestützt. Damit wurde zum ersten Mal ein eindeutiger Nachweis des "Axion Isolators" erbracht.

Der Quanten-anomale-Hall-Effekt in magnetisch dotierten topologischen Isolatoren stellt ein vielversprechendes System für weitere Untersuchungen dar. Die Existenz des Majorana Zustands ist für die Kombination des Quanten-anomalen-Hall-Effekts mit Supraleitung vorhergesagt. Dies könnte Anwendung in Quantencomputern finden. In dreilagigen Systemen, die aus zwei magnetischen Schichten mit einer dazwischenliegenden nicht magnetischen Schicht zusammengesetzt sind, sollte es möglich sein, zwei unterschiedliche Koerzitivfeldstärken für die magnetischen Schichten zu erreichen. Für eine entgegengesetzte Magnetisierung sollte dann das nullte Hall Plateau auftreten und die Existenz des topologischen magnetoelektrische Effekt ist vorhergesagt. Durch unterschiedliche Koerzitivfeldstärken in lateraler Richtung könnte eine Änderung der Magnetisierung durch einen Stromfluss in den spinpolarisierten Randkanälen erreicht werden, was eine Grundlage für die Realisierung von spintronik Bauteilen darstellt.

Als Fazit dieser Arbeit wurde zum Einen in nicht magnetischen Bi_2Se_3 und verwandten Materialien kein eindeutiges Zeichen eines Oberflächenzustands im elektrischen Transport gefunden. Der Anteil des Volumens an der Leitfähigkeit dominiert und nach ausführlichen Untersuchungen in dieser Arbeit und von anderen Gruppen ist es fraglich, ob die Nutzung dieser Materialien als topologische Isolatoren sinnvoll ist. Im Gegensatz dazu sind die Ergebnisse dieser Arbeit für magnetisch dotierte Schichten sehr vielversprechend. Die verbleibenden Ladungsträger des Volumens konnten im Mischkryostaten lokalisiert werden, der Quanten-anomale-Hall-Effekt wurde realisiert und erstmalig der Transport in einem "axion Isolator" beobachtet. Damit gelang ein klarer Nachweis des Oberflächenzustands und es ergeben sich weitere Optionen für die Grundlagenforschung.

Appendix A

A.1 Fit parameteres

x	d (nm)	$n_1(cm^{-3})$	$\mu_1(\frac{cm^2}{Vs})$	$n_2(cm^{-3})$	$\mu_2(\frac{cm^2}{Vs})$
0	102	$1.64 \cdot 10^{18}$	510	$3.44 \cdot 10^{17}$	3080
0.001	104	$2.30 \cdot 10^{18}$	497	$3.48 \cdot 10^{17}$	2420
0.0045	105	$2.07 \cdot 10^{18}$	406	$2.93 \cdot 10^{17}$	2200
0.0245	104	$1.97 \cdot 10^{18}$	541	$4.27 \cdot 10^{17}$	2560
0.14	117	$1.40 \cdot 10^{18}$	419	$2.89 \cdot 10^{17}$	1840
0.3	139	$7.37 \cdot 10^{17}$	535	$2.14 \cdot 10^{17}$	2560
0.39	152	$6.06 \cdot 10^{17}$	428	$1.16 \cdot 10^{17}$	2800
0.44	160	$3.17 \cdot 10^{17}$	597	$1.33 \cdot 10^{17}$	2960
0.525	170	$5.54 \cdot 10^{17}$	427	$8.25 \cdot 10^{16}$	1660
0.555	180	$4.77 \cdot 10^{17}$	400	$5.24 \cdot 10^{16}$	2060
0.61	190	$8.10 \cdot 10^{17}$	701	$2.86 \cdot 10^{17}$	2690

Table A.1: Parameters used to fit the magnetoresistance of $(Bi_{1-x}Sb_x)_2Se_3$-layers grown on InP(111) to the two carrier model at $T = 4.2$ K. The obtained densities are plotted in fig. 3.7.

d (nm)	$n(cm^{-3})$	$\mu(\frac{cm^2}{Vs})$
15	2.11E19	205
30	9.66E18	400
50	8.08E18	458
70	8.89E18	241
120	1.02E19	459

Table A.2: Parameters extracted from the hall measurements for Bi_2Se_3-layers grown on Si(111) of different thickness at $T = 4.2$ K.

A.2 Oscillations in the resistance

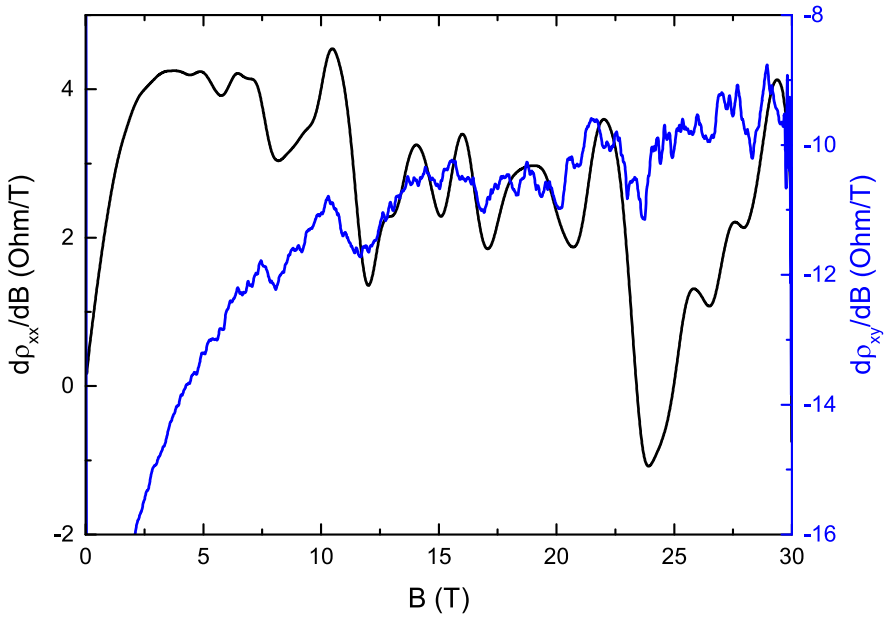

Fig. A.1: Derivative of the magnetoresitance shown in fig. 3.15. Taking the derivative pronounces the oscillations of ρ_{xx} and reveals the oscillations of ρ_{xy}. This demonstrates the dependence of ρ_{xy} on the individual conductivities in the two carrier model.

Measurements on thinner samples, with $d = 20$ nm, 50 nm and 190 nm at $T = 4.2$ K show the same results as in the main text. The oscillations align to the perpendicular magnetic field up to an angle of about 45°.

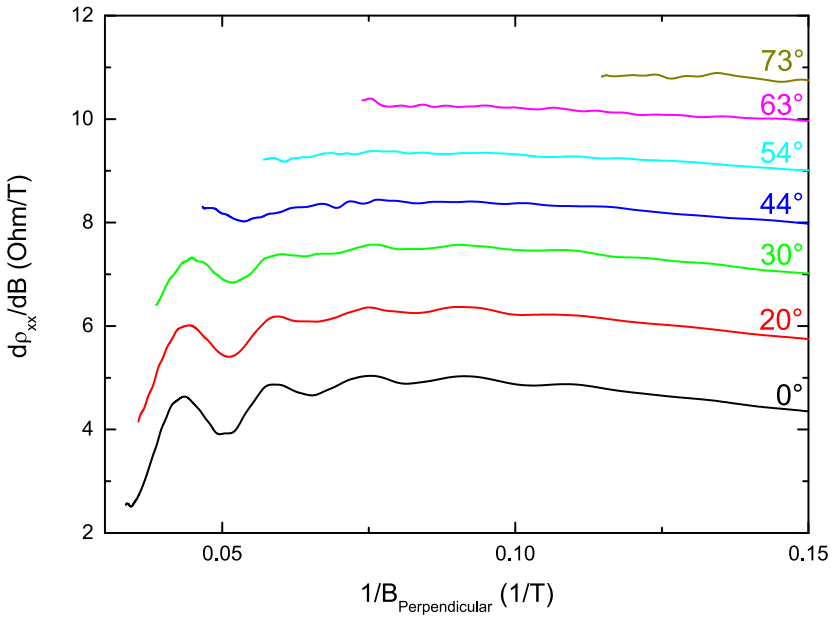

Fig. A.2: The derivative of the magnetoresistance for different magnetic field angles, vertically shifted for clarity. At 0° the magnetic field is perpendicular to the surface and at 90° the magnetic field is parallel to the surface. Measured on Bi_2Se_3 with $d = 20$ nm grown on InP(111).

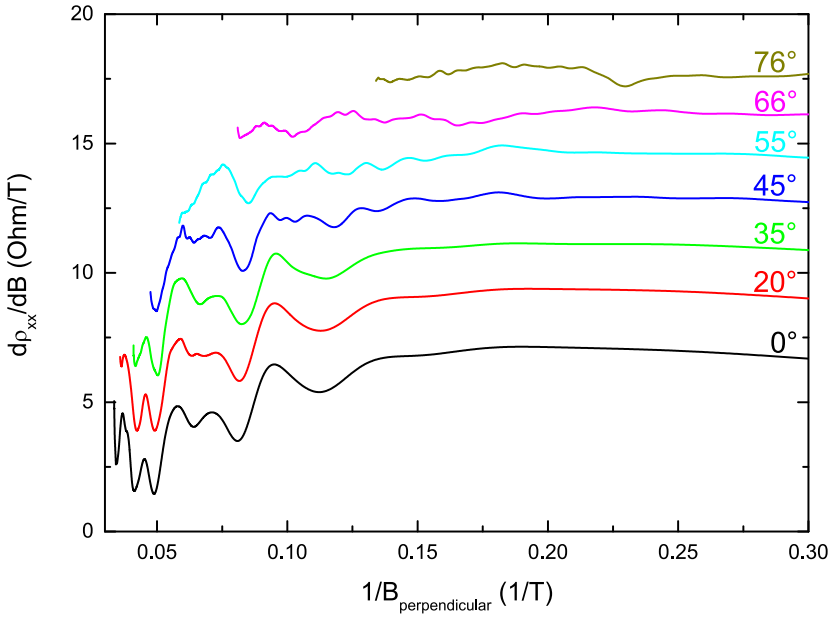

Fig. A.3: The derivative of the magnetoresistance for different magnetic field angles, vertically shifted for clarity. At 0° the magnetic field is perpendicular to the surface and at 90° the magnetic field is parallel to the surface. Measured on Bi_2Se_3 with $d = 50$ nm grown on InP(111).

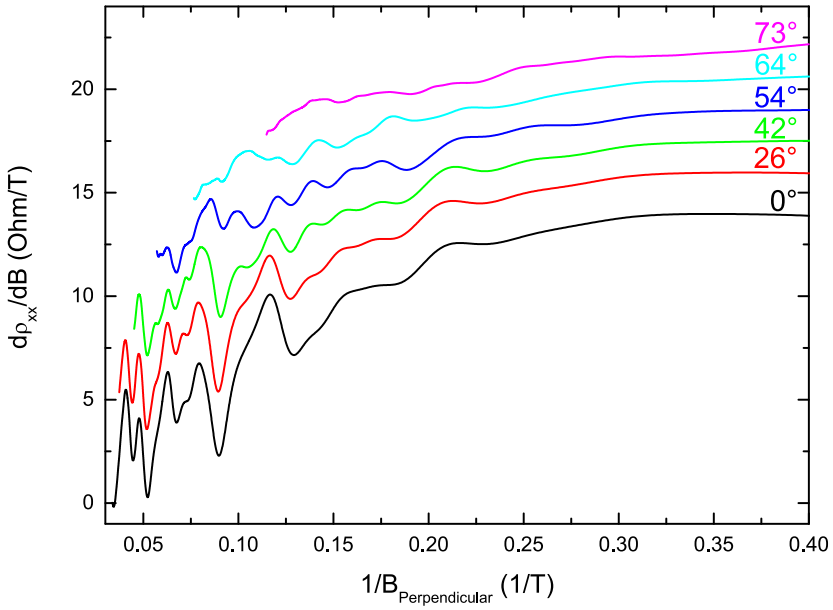

Fig. A.4: The derivative of the magnetoresistance for different magnetic field angles, vertically shifted for clarity. At 0° the magnetic field is perpendicular to the surface and at 90° the magnetic field is parallel to the surface. Measured on Bi_2Se_3 with $d = 190$ nm grown on InP(111).

A.3 Superparamagnetism in another Cr-doped sample

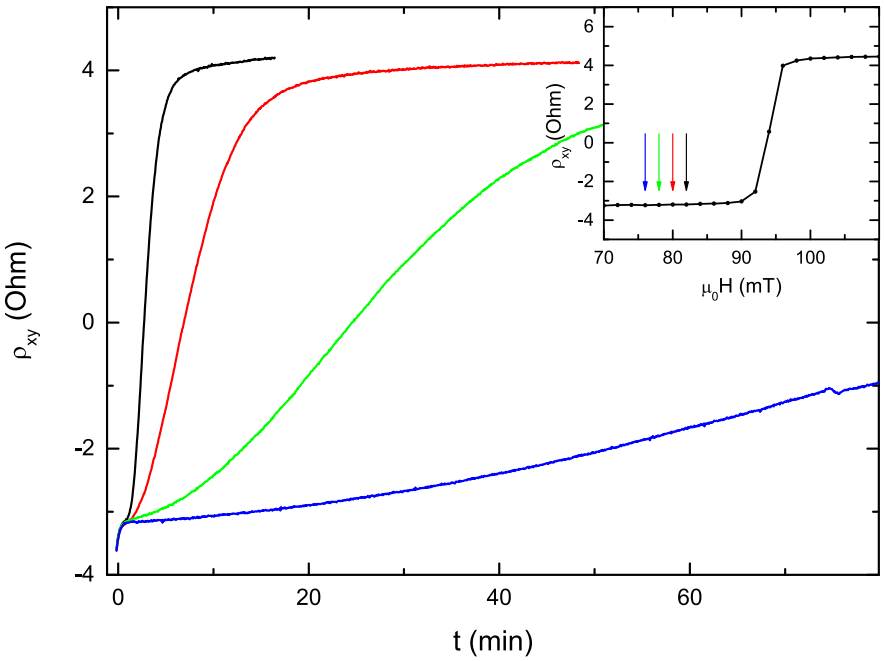

Fig. A.5: Measurement over time on a $Cr_{0.13}(Bi_{0.2}Sb_{0.8})_{1.87}Te_3$-layer with $d = 41$ nm at different constant magnetic fields and $T = 4.2$ K. The magnetization of the sample for each measurement was prepared by sweeping from negative saturation to the magnetic field indicated by the arrow of the corresponding color in the inset.

A.4 Measurement on another Cr-doped sample at millikelvin temperatures

The second $Cr_{0.13}(Bi_{0.2}Sb_{0.8})_{1.87}Te_3$ sample on which measurements at millikelvin temperatures could be conducted was grown at $T_{Sub} = 300°C$ and has a thickness of $d = 8$ nm. It does not show insulating behavior at $T = 30$ mK, the IV-curve is still linear. As it can be seen in the magnetic field sweep in the figure, conducted for the gate voltage with the maximum ρ_{xy}, the values of ρ_{xy} and ρ_{xx} are far from quantization.

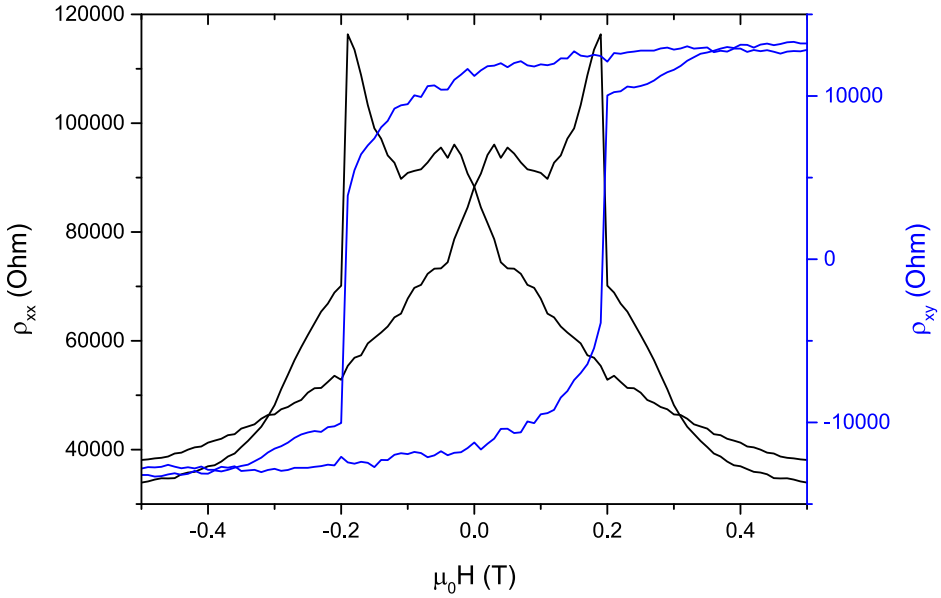

Fig. A.6: Measurement of the magnetic field dependence of ρ_{xx} (black) and ρ_{xy} (blue) on the $d = 8$ nm $Cr_{0.13}(Bi_{0.2}Sb_{0.8})_{1.87}Te_3$-layer at $T = 30$ mK and $V_g = 6.2$ V. The data was only acquired for one sweep direction and is reflected on the y-axis (ρ_{xx}) and the origin (ρ_{xy}) to emphasize the hysteresis.

A.5 Measurements on another sample in the QAHE regime

The results of measurements at fridge base temperature $T = 15$ mK for the $V_{0.1}(Bi_{0.20}Sb_{0.80})_{1.9}Te_3$ layer with $d = 9$ nm grown at $T_{Sub} = 190°C$ are shown in the following figures. The results agree with the ones shown in the main text. The values of ρ_{xy} and ρ_{xx} are close to quantization, non-local transport demonstrates the edge channel transport and the zero field feature, the spikes in the magnetoresistance and the jumps during warming are present.

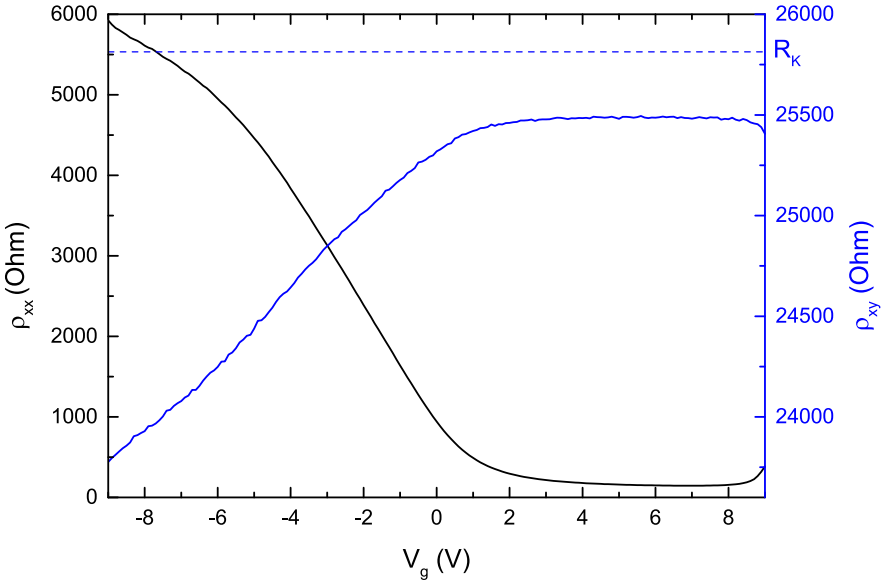

Fig. A.7: Measurement of the gate voltage dependence of ρ_{xx} (black) and ρ_{xy} (blue) on the described layer at $T = 15$ mK and $H = 0$. Quantization conditions are almost achieved and $V_0 = 6.8$ V is chosen for further measurements in the QAHE-regime.

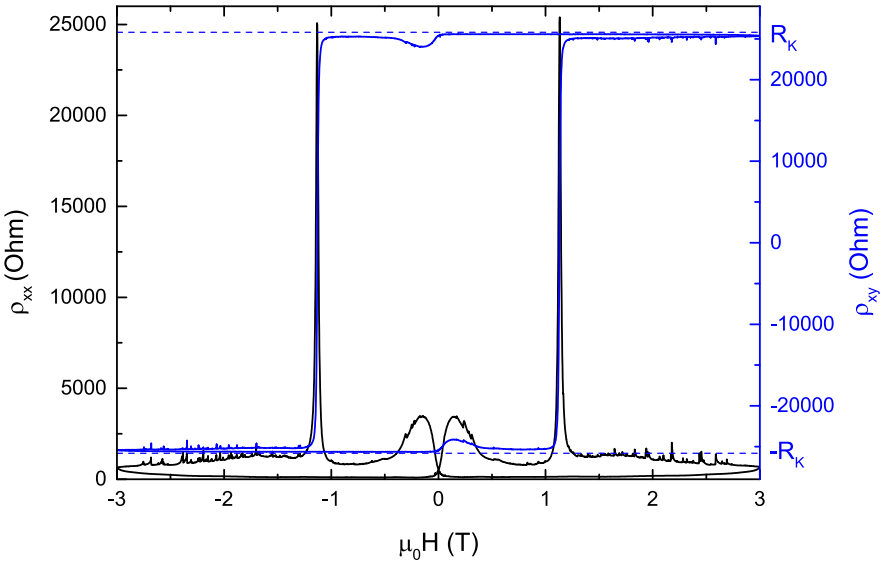

Fig. A.8: Magnetic field sweep at $T = 15$ mK and V_0. Hall (blue) and longitudinal (black) resistivity are shown to demonstrate the accuracy and stability of the quantization of the QAHE in the layer. At about 1.1 T the magnetization of the sample changes, which leads to a change of sign for hall resistivity and a large longitudinal resistivity during the switching process.

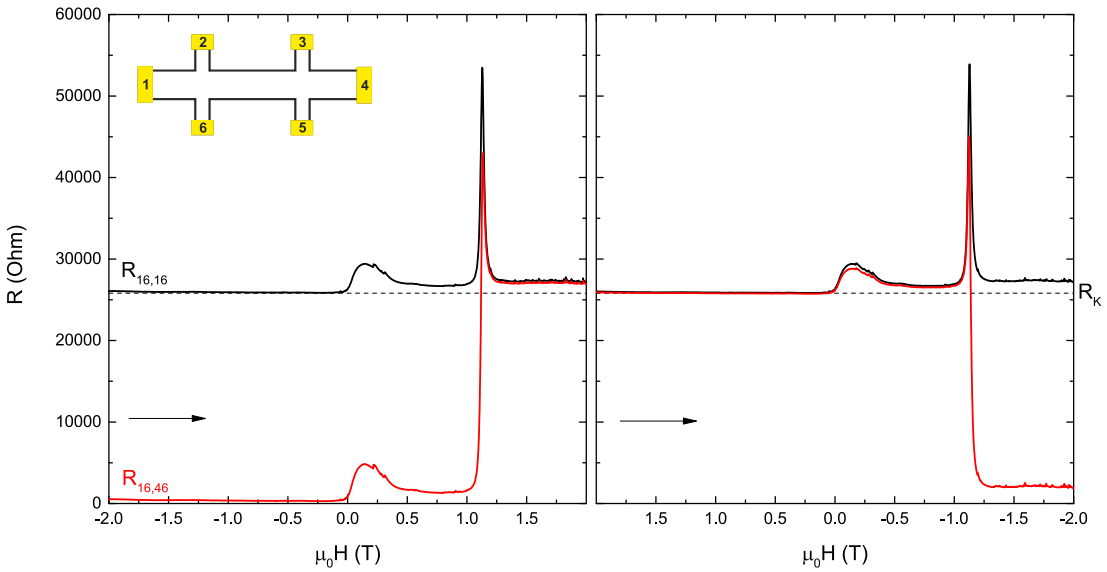

Fig. A.9: Measurement of a non-local and a two-terminal resistance, $R_{16,16}$ (black) and $R_{16,46}$ (red), on the sample at $T = 15$ mK and V_0. The position of the contacts on the Hall bar is shown by the schematic drawing in the upper left corner of the left figure. For both figures the magnetic field is swept in direction of the x-axis, as indicated by the arrows.

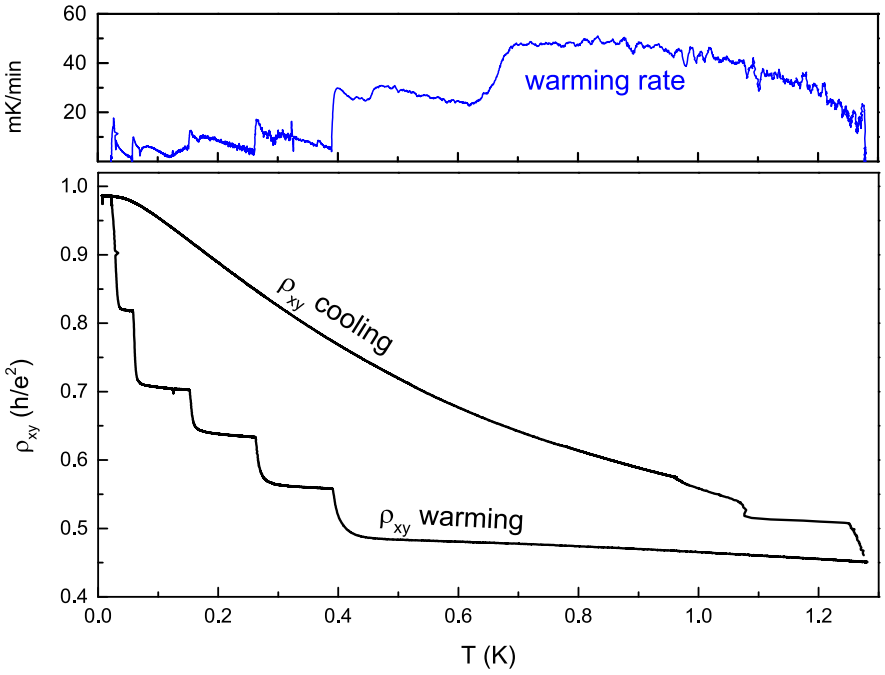

Fig. A.10: In the lower part of the figure the temperature dependence of ρ_{xy} during cooling and warming at V_0 and $H = 0$ is displayed. The upper part shows the rate of the temperature change of the fridge during warming. It can be seen that the sudden drops in ρ_{xy} coincide with changes of the warming rate.

Bibliography

[1] A. H. Wilson. The Theory of Electronic Semi-Conductors. *Proceedings of the Royal Society of London A: Mathematical, Physical and Engineering Sciences*, 133(822):458–491, 1931.

[2] K. v. Klitzing, G. Dorda, and M. Pepper. New Method for High-Accuracy Determination of the Fine-Structure Constant Based on Quantized Hall Resistance. *Physical Review Letters*, 45(6):494–497, 1980.

[3] The Law That's Not A Law. *IEEE Spectrum*, 52(4):38–57, April 2015.

[4] C. L. Kane and E. J. Mele. Quantum Spin Hall Effect in Graphene. *Physical Review Letters*, 95(22):226801, 2005.

[5] C. L. Kane and E. J. Mele. Z_2 Topological Order and the Quantum Spin Hall Effect. *Physical Review Letters*, 95(14):146802, 2005.

[6] L. Fu, C. L. Kane, and E. J. Mele. Topological Insulators in Three Dimensions. *Physical Review Letters*, 98(10):106803, 2007.

[7] L. Fu and C. L. Kane. Superconducting Proximity Effect and Majorana Fermions at the Surface of a Topological Insulator. *Physical Review Letters*, 100(9):096407, 2008.

[8] A. Y. Kitaev. Fault-tolerant quantum computation by anyons. *Annals of Physics*, 303(1):2–30, 2003.

[9] B. A. Bernevig, T. L. Hughes, and S.-C. Zhang. Quantum Spin Hall Effect and Topological Phase Transition in HgTe Quantum Wells. *Science*, 314(5806):1757–1761, 2006.

[10] B. A. Bernevig and S.-C. Zhang. Quantum Spin Hall Effect. *Physical Review Letters*, 96(10):106802, 2006.

[11] M. König, S. Wiedmann, C. Brüne, A. Roth, H. Buhmann, L. W. Molenkamp, X. Qi, and S. Zhang. Quantum Spin Hall Insulator State in HgTe Quantum Wells. *Science*, 318(5851):766–770, 2007.

[12] C.-Z. Chang, J. Zhang, X. Feng, J. Shen, Z. Zhang, M. Guo, K. Li, Y. Ou, P. Wei, L.-L. Wang, Z.-Q. Ji, Y. Feng, S. Ji, X. Chen, J. Jia, X. Dai, Z. Fang, S.-C. Zhang, K. He, Y. Wang, L. Lu, X.-C. Ma, and Q.-K. Xue. Experimental Observation of the Quantum Anomalous Hall Effect in a Magnetic Topological Insulator. *Science*, 340(6129):167–170, 2013.

[13] X.-L. Qi, R. Li, J. Zang, and S.-C. Zhang. Inducing a Magnetic Monopole with Topological Surface States. *Science*, 323(5918):1184–1187, 2009.

[14] H. Zhang, C.-X. Liu, X.-L. Qi, X. Dai, Z. Fang, and S.-C. Zhang. Topological insulators in Bi_2Se_3, Bi_2Te_3 and Sb_2Te_3 with a single Dirac cone on the surface. *Nat Phys*, 5(6):438–442, 2009.

[15] D. Hsieh, D. Qian, L. Wray, Y. Xia, Y. S. Hor, R. J. Cava, and M. Z. Hasan. A topological Dirac insulator in a quantum spin Hall phase. *Nature*, 452(7190):970–974, 2008.

[16] Y. L. Chen, J. G. Analytis, J.-H. Chu, Z. K. Liu, S.-K. Mo, X. L. Qi, H. J. Zhang, D. H. Lu, X. Dai, Z. Fang, S. C. Zhang, I. R. Fisher, Z. Hussain, and Z.-X. Shen. Experimental Realization of a Three-Dimensional Topological Insulator, Bi_2Te_3. *Science*, 325(5937):178–181, 2009.

[17] T. Zhang, P. Cheng, X. Chen, J.-F. Jia, X. Ma, K. He, L. Wang, H. Zhang, X. Dai, Z. Fang, X. Xie, and Q.-K. Xue. Experimental Demonstration of Topological Surface States Protected by Time-Reversal Symmetry. *Physical Review Letters*, 103(26):266803, 2009.

[18] S. Grauer, S. Schreyeck, M. Winnerlein, K. Brunner, C. Gould, and L. W. Molenkamp. Coincidence of superparamagnetism and perfect quantization in the quantum anomalous Hall state. *Physical Review B*, 92(20):201304, 2015.

[19] D. J. Thouless, M. Kohmoto, M. P. Nightingale, and M. den Nijs. Quantized Hall Conductance in a Two-Dimensional Periodic Potential. *Physical Review Letters*, 49(6):405–408, 1982.

[20] M. Kohmoto. Topological invariant and the quantization of the Hall conductance. *Annals of Physics*, 160(2):343 – 354, 1985.

[21] L. Fu and C. L. Kane. Topological insulators with inversion symmetry. *Physical Review B*, 76(4):045302, 2007.

[22] C.-X. Liu, X.-L. Qi, H. Zhang, X. Dai, Z. Fang, and S.-C. Zhang. Model Hamiltonian for topological insulators. *Physical Review B*, 82(4):045122, 2010.

[23] K. Nomura, M. Koshino, and S. Ryu. Topological Delocalization of Two-Dimensional Massless Dirac Fermions. *Physical Review Letters*, 99(14):146806, 2007.

[24] R. Jackiw. Fractional charge and zero modes for planar systems in a magnetic field. *Physical Review D*, 29(10):2375–2377, 1984.

[25] C. Brüne, C. X. Liu, E. G. Novik, E. M. Hankiewicz, H. Buhmann, Y. L. Chen, X. L. Qi, Z. X. Shen, S. C. Zhang, and L. W. Molenkamp. Quantum Hall Effect from the Topological Surface States of Strained Bulk HgTe. *Physical Review Letters*, 106(12):126803, 2011.

[26] Y. Xia, D. Qian, D. Hsieh, L. Wray, A. Pal, H. Lin, A. Bansil, D. Grauer, Y. S. Hor, R. J. Cava, and M. Z. Hasan. Observation of a large-gap topological-insulator class with a single Dirac cone on the surface. *Nat Phys*, 5(6):398–402, 2009.

[27] D. Rowe. *CRC Handbook of Thermoelectrics*. CRC Press, 1995.

[28] S. Souma, K. Kosaka, T. Sato, M. Komatsu, A. Takayama, T. Takahashi, M. Kriener, K. Segawa, and Y. Ando. Direct Measurement of the Out-of-Plane Spin Texture in the Dirac-Cone Surface State of a Topological Insulator. *Physical Review Letters*, 106(21):216803, 2011.

[29] T. Hanaguri, K. Igarashi, M. Kawamura, H. Takagi, and T. Sasagawa. Momentum-resolved Landau-level spectroscopy of Dirac surface state in Bi_2Se_3. *Physical Review B*, 82(8):081305, 2010.

[30] D. Hsieh, Y. Xia, D. Qian, L. Wray, J. H. Dil, F. Meier, J. Osterwalder, L. Patthey, J. G. Checkelsky, N. P. Ong, A. V. Fedorov, H. Lin, A. Bansil, D. Grauer, Y. S. Hor, R. J. Cava, and M. Z. Hasan. A tunable topological insulator in the spin helical Dirac transport regime. *Nature*, 460(7259):1101–1105, 2009.

[31] K. Kuroda, M. Arita, K. Miyamoto, M. Ye, J. Jiang, A. Kimura, E. E. Krasovskii, E. V. Chulkov, H. Iwasawa, T. Okuda, K. Shimada, Y. Ueda, H. Namatame, and M. Taniguchi. Hexagonally Deformed Fermi Surface of the 3D Topological Insulator Bi_2Se_3. *Physical Review Letters*, 105(7):076802, 2010.

[32] S. R. Park, W. S. Jung, C. Kim, D. J. Song, C. Kim, S. Kimura, K. D. Lee, and N. Hur. Quasiparticle scattering and the protected nature of the topological states in a parent topological insulator Bi_2Se_3. *Physical Review B*, 81(4):041405, 2010.

[33] D. Hsieh, Y. Xia, D. Qian, L. Wray, F. Meier, J. H. Dil, J. Osterwalder, L. Patthey, A. V. Fedorov, H. Lin, A. Bansil, D. Grauer, Y. S. Hor, R. J. Cava, and M. Z. Hasan. Observation of Time-Reversal-Protected Single-Dirac-Cone Topological-Insulator States in Bi_2Te_3 and Sb_2Te_3. *Physical Review Letters*, 103(14):146401, 2009.

[34] S. R. Park, J. Han, C. Kim, Y. Y. Koh, C. Kim, H. Lee, H. J. Choi, J. H. Han, K. D. Lee, N. J. Hur, M. Arita, K. Shimada, H. Namatame, and M. Taniguchi. Chiral Orbital-Angular Momentum in the Surface States of Bi_2Se_3. *Physical Review Letters*, 108(4):046805, 2012.

[35] K. Miyamoto, A. Kimura, T. Okuda, H. Miyahara, K. Kuroda, H. Namatame, M. Taniguchi, S. V. Eremeev, T. V. Menshchikova, E. V. Chulkov, K. A. Kokh, and O. E. Tereshchenko. Topological Surface States with Persistent High Spin Polarization across the Dirac Point in Bi_2Te_2Se and Bi_2Se_2Te. *Physical Review Letters*, 109(16):166802, 2012.

[36] P. Cheng, C. Song, T. Zhang, Y. Zhang, Y. Wang, J.-F. Jia, J. Wang, Y. Wang, B.-F. Zhu, X. Chen, X. Ma, K. He, L. Wang, X. Dai, Z. Fang, X. Xie, X.-L. Qi, C.-X. Liu, S.-C. Zhang, and Q.-K. Xue. Landau Quantization of Topological Surface States in Bi_2Se_3. *Physical Review Letters*, 105(7):076801, 2010.

[37] J. G. Analytis, J.-H. Chu, Y. Chen, F. Corredor, R. D. McDonald, Z. X. Shen, and I. R. Fisher. Bulk Fermi surface coexistence with Dirac surface state in Bi_2Se_3: A comparison of photoemission and Shubnikov–de Haas measurements. *Physical Review B*, 81(20):205407, 2010.

[38] N. P. Butch, K. Kirshenbaum, P. Syers, A. B. Sushkov, G. S. Jenkins, H. D. Drew, and J. Paglione. Strong surface scattering in ultrahigh-mobility Bi_2Se_3 topological insulator crystals. *Physical Review B*, 81(24):241301, 2010.

[39] K. Eto, Z. Ren, A. A. Taskin, K. Segawa, and Y. Ando. Angular-dependent oscillations of the magnetoresistance in Bi_2Se_3 due to the three-dimensional bulk Fermi surface. *Physical Review B*, 81(19):195309, 2010.

[40] J. G. Analytis, R. D. McDonald, S. C. Riggs, J.-H. Chu, G. S. Boebinger, and I. R. Fisher. Two-dimensional surface state in the quantum limit of a topological insulator. *Nat Phys*, 6(12):960–964, 2010.

[41] D.-X. Qu, Y. S. Hor, J. Xiong, R. J. Cava, and N. P. Ong. Quantum Oscillations and Hall Anomaly of Surface States in the Topological Insulator Bi_2Te_3. *Science*, 329(5993):821–824, 2010.

[42] Z. Ren, A. A. Taskin, S. Sasaki, K. Segawa, and Y. Ando. Large bulk resistivity and surface quantum oscillations in the topological insulator Bi_2Te_2Se. *Physical Review B*, 82(24):241306, 2010.

[43] Z. Ren, A. A. Taskin, S. Sasaki, K. Segawa, and Y. Ando. Optimizing $Bi_{2-x}Sb_xTe_{3-y}Se_y$ solid solutions to approach the intrinsic topological insulator regime. *Physical Review B*, 84(16):165311, 2011.

[44] B. Sacépé, J. B. Oostinga, J. Li, A. Ubaldini, N. J. G. Couto, E. Giannini, and A. F. Morpurgo. Gate-tuned normal and superconducting transport at the surface of a topological insulator. *Nat Commun*, 2:575, 2011.

[45] A. A. Taskin, Z. Ren, S. Sasaki, K. Segawa, and Y. Ando. Observation of Dirac Holes and Electrons in a Topological Insulator. *Physical Review Letters*, 107(1):016801, 2011.

[46] J. Xiong, A. C. Petersen, D. Qu, Y. S. Hor, R. J. Cava, and N. P. Ong. Quantum oscillations in a topological insulator Bi_2Te_2Se with large bulk resistivity (6 Ohm cm). *Physica E: Low-dimensional Systems and Nanostructures*, 44(5):917–920, 2012.

[47] H. Cao, J. Tian, I. Miotkowski, T. Shen, J. Hu, S. Qiao, and Y. P. Chen. Quantized Hall Effect and Shubnikov-de Haas Oscillations in Highly Doped Bi_2Se_3: Evidence for Layered Transport of Bulk Carriers. *Physical Review Letters*, 108(21):216803, 2012.

[48] J. Xiong, Y. Luo, Y. Khoo, S. Jia, R. J. Cava, and N. P. Ong. High-field Shubnikov-de Haas oscillations in the topological insulator Bi_2Te_2Se. *Physical Review B*, 86(4):045314, 2012.

[49] Z. Ren, A. A. Taskin, S. Sasaki, K. Segawa, and Y. Ando. Fermi level tuning and a large activation gap achieved in the topological insulator Bi_2Te_2Se by Sn doping. *Physical Review B*, 85(15):155301, 2012.

[50] A. A. Taskin, S. Sasaki, K. Segawa, and Y. Ando. Manifestation of Topological Protection in Transport Properties of Epitaxial Bi_2Se_3 Thin Films. *Physical Review Letters*, 109(6):066803, 2012.

[51] M. Veldhorst, M. Snelder, M. Hoek, T. Gang, V. K. Guduru, X. L. Wang, U. Zeitler, W. G. van der Wiel, A. A. Golubov, H. Hilgenkamp, and A. Brinkman. Josephson supercurrent through a topological insulator surface state. *Nat Mater*, 11(5):417–421, 2012.

[52] L. He, F. Xiu, X. Yu, M. Teague, W. Jiang, Y. Fan, X. Kou, M. Lang, Y. Wang, G. Huang, N.-C. Yeh, and K. L. Wang. Surface-Dominated Conduction in a 6 nm thick Bi_2Se_3 Thin Film. *Nano Letters*, 12(3):1486–1490, 2012.

[53] S. S. Hong, J. J. Cha, D. Kong, and Y. Cui. Ultra-low carrier concentration and surface-dominant transport in antimony-doped Bi_2Se_3 topological insulator nanoribbons. *Nat Commun*, 3:757, 2012.

[54] M. Petrushevsky, E. Lahoud, A. Ron, E. Maniv, I. Diamant, I. Neder, S. Wiedmann, V. K. Guduru, F. Chiappini, U. Zeitler, J. C. Maan, K. Chashka, A. Kanigel, and Y. Dagan. Probing the surface states in Bi_2Se_3 using the Shubnikov–de Haas effect. *Physical Review B*, 86(4):045131, 2012.

[55] A. A. Taskin, S. Sasaki, K. Segawa, and Y. Ando. Achieving Surface Quantum Oscillations in Topological Insulator Thin Films of Bi_2Se_3. *Advanced Materials*, 24(41):5581–5585, 2012.

[56] L. He, X. Kou, M. Lang, E. S. Choi, Y. Jiang, T. Nie, W. Jiang, Y. Fan, Y. Wang, F. Xiu, and K. L. Wang. Evidence of the two surface states of $(Bi_{0.53}Sb_{0.47})_2Te_3$ films grown by van der Waals epitaxy. *Sci. Rep.*, 3, 2013.

[57] M. Brahlek, N. Koirala, M. Salehi, N. Bansal, and S. Oh. Emergence of Decoupled Surface Transport Channels in Bulk Insulating Bi_2Se_3 Thin Films. *Physical Review Letters*, 113(2):026801, 2014.

[58] H. Tang, D. Liang, R. L. J. Qiu, and X. P. A. Gao. Two-Dimensional Transport-Induced Linear Magneto-Resistance in Topological Insulator Bi_2Se_3 Nanoribbons. *ACS Nano*, 5(9):7510–7516, 2011.

[59] G. Zhang, H. Qin, J. Chen, X. He, L. Lu, Y. Li, and K. Wu. Growth of Topological Insulator Bi_2Se_3 Thin Films on $SrTiO_3$ with Large Tunability in Chemical Potential. *Advanced Functional Materials*, 21(12):2351–2355, 2011.

[60] X. He, T. Guan, X. Wang, B. Feng, P. Cheng, L. Chen, Y. Li, and K. Wu. Highly tunable electron transport in epitaxial topological insulator $(Bi_{1-x}Sb_x)_2Te_3$ thin films. *Applied Physics Letters*, 101(12):123111, 2012.

[61] X. Wang, Y. Du, S. Dou, and C. Zhang. Room Temperature Giant and Linear Magnetoresistance in Topological Insulator Bi_2Te_3 Nanosheets. *Physical Review Letters*, 108(26):266806, 2012.

[62] B. F. Gao, P. Gehring, M. Burghard, and K. Kern. Gate-controlled linear magnetoresistance in thin Bi_2Se_3 sheets. *Applied Physics Letters*, 100(21):212402, 2012.

[63] S. X. Zhang, R. D. McDonald, A. Shekhter, Z. X. Bi, Y. Li, Q. X. Jia, and S. T. Picraux. Magneto-resistance up to 60 Tesla in topological insulator Bi_2Te_3 thin films. *Applied Physics Letters*, 101(20):202403, 2012.

[64] Y. Yan, L.-X. Wang, D.-P. Yu, and Z.-M. Liao. Large magnetoresistance in high mobility topological insulator Bi_2Se_3. *Applied Physics Letters*, 103(3):033106, 2013.

[65] B. A. Assaf, T. Cardinal, P. Wei, F. Katmis, J. S. Moodera, and D. Heiman. Linear magnetoresistance in topological insulator thin films: Quantum phase coherence effects at high temperatures. *Applied Physics Letters*, 102(1):012102, 2013.

[66] Z. H. Wang, L. Yang, X. J. Li, X. T. Zhao, H. L. Wang, Z. D. Zhang, and X. P. A. Gao. Granularity Controlled Nonsaturating Linear Magnetoresistance in Topological Insulator Bi_2Te_3 Films. *Nano Letters*, 14(11):6510–6514, 2014.

[67] J. Tian, C. Chang, H. Cao, K. He, X. Ma, Q. Xue, and Y. P. Chen. Quantum and Classical Magnetoresistance in Ambipolar Topological Insulator Transistors with Gate-tunable Bulk and Surface Conduction. *Scientific Reports*, 4:4859, 2014.

[68] D. Kim, S. Cho, N. P. Butch, P. Syers, K. Kirshenbaum, S. Adam, J. Paglione, and M. S. Fuhrer. Surface conduction of topological Dirac electrons in bulk insulating Bi_2Se_3. *Nat Phys*, 8(6):459–463, 2012.

[69] J. Chen, H. J. Qin, F. Yang, J. Liu, T. Guan, F. M. Qu, G. H. Zhang, J. R. Shi, X. C. Xie, C. L. Yang, K. H. Wu, Y. Q. Li, and L. Lu. Gate-Voltage Control of Chemical Potential and Weak Antilocalization in Bi_2Se_3. *Physical Review Letters*, 105(17):176602, 2010.

[70] J. Chen, X. Y. He, K. H. Wu, Z. Q. Ji, L. Lu, J. R. Shi, J. H. Smet, and Y. Q. Li. Tunable surface conductivity in Bi_2Se_3 revealed in diffusive electron transport. *Physical Review B*, 83(24):241304, 2011.

[71] Y. S. Kim, M. Brahlek, N. Bansal, E. Edrey, G. A. Kapilevich, K. Iida, M. Tanimura, Y. Horibe, S.-W. Cheong, and S. Oh. Thickness-dependent bulk properties and weak antilocalization effect in topological insulator Bi_2Se_3. *Physical Review B*, 84(7):073109, 2011.

[72] H. Steinberg, J. B. Laloë, V. Fatemi, J. S. Moodera, and P. Jarillo-Herrero. Electrically tunable surface-to-bulk coherent coupling in topological insulator thin films. *Physical Review B*, 84(23):233101, 2011.

[73] J. Wang, A. M. DaSilva, C.-Z. Chang, K. He, J. K. Jain, N. Samarth, X.-C. Ma, Q.-K. Xue, and M. H. W. Chan. Evidence for electron-electron interaction in topological insulator thin films. *Physical Review B*, 83(24):245438, 2011.

[74] H.-T. He, G. Wang, T. Zhang, I.-K. Sou, G. K. L. Wong, J.-N. Wang, H.-Z. Lu, S.-Q. Shen, and F.-C. Zhang. Impurity Effect on Weak Anti-localization in the Topological Insulator Bi_2Te_3. *Physical Review Letters*, 106(16):166805, 2011.

[75] H. B. Zhang, H. L. Yu, D. H. Bao, S. W. Li, C. X. Wang, and G. W. Yang. Weak localization bulk state in a topological insulator Bi_2Te_3 film. *Physical Review B*, 86(7):075102, 2012.

[76] C. H. Li, O. M. J. van 't Erve, J. T. Robinson, LiuY, LiL, and B. T. Jonker. Electrical detection of charge-current-induced spin polarization due to spin-momentum locking in Bi_2Se_3. *Nat Nano*, 9(3):218–224, 2014.

[77] J. Horák, Z. Stary, P. Lošák, and J. Pancí. Anti-site defects in n-Bi_2Se_3 crystals. *Journal of Physics and Chemistry of Solids*, 51(12):1353–1360, 1990.

[78] J. Navrátil, J. Horák, T. Plecháček, S. Kamba, P. Lošt'ák, J. S. Dyck, W. Chen, and C. Uher. Conduction band splitting and transport properties of Bi_2Se_3. *Journal of Solid State Chemistry*, 177(4–5):1704–1712, 2004.

[79] Y. S. Hor, A. Richardella, P. Roushan, Y. Xia, J. G. Checkelsky, A. Yazdani, M. Z. Hasan, N. P. Ong, and R. J. Cava. Bi_2Se_3 for topological insulator and low-temperature thermoelectric applications. *Physical Review B*, 79(19):195208, 2009.

[80] F. T. Huang, M. W. Chu, H. H. Kung, W. L. Lee, R. Sankar, S. C. Liou, K. K. Wu, Y. K. Kuo, and F. C. Chou. Nonstoichiometric doping and Bi antisite defect in single crystal Bi_2Se_3. *Physical Review B*, 86(8):081104, 2012.

[81] S. Schreyeck, N. V. Tarakina, G. Karczewski, C. Schumacher, T. Borzenko, C. Brüne, H. Buhmann, C. Gould, K. Brunner, and L. W. Molenkamp. Molecular beam epitaxy of high structural quality Bi_2Se_3 on lattice matched InP(111) substrates. *Applied Physics Letters*, 102(4):041914, 2013.

[82] Z. Y. Wang, H. D. Li, X. Guo, W. K. Ho, and M. H. Xie. Growth characteristics of topological insulator Bi_2Se_3 films on different substrates. *Journal of Crystal Growth*, 334(1):96–102, 2011.

[83] N. V. Tarakina, S. Schreyeck, T. Borzenko, C. Schumacher, G. Karczewski, K. Brunner, C. Gould, H. Buhmann, and L. W. Molenkamp. Comparative Study of the Microstructure of Bi_2Se_3 Thin Films Grown on Si(111) and InP(111) Substrates. *Crystal Growth & Design*, 12(4):1913–1918, 2012.

[84] N. V. Tarakina, S. Schreyeck, M. Luysberg, S. Grauer, C. Schumacher, G. Karczewski, K. Brunner, C. Gould, H. Buhmann, R. E. Dunin-Borkowski, and L. W. Molenkamp. Suppressing Twin Formation in Bi_2Se_3 Thin Films. *Advanced Materials Interfaces*, 1:1400134, 2014.

[85] A. G. Baca, F. Ren, J. C. Zolper, R. D. Briggs, and S. J. Pearton. A survey of ohmic contacts to III-V compound semiconductors. *Thin Solid Films*, 308–309:599–606, 1997.

[86] W. Wang, L. Li, W. Zou, L. He, F. Song, R. Zhang, X. Wu, and F. Zhang. Intrinsic Topological Insulator $Bi_{1.5}Sb_{0.5}Te_{3-x}Se_x$ Thin Crystals. *Sci. Rep.*, 5, 2015.

[87] P. Lošt'ák, v. Drašar, H. Süssmann, P. Reinshaus, R. Novotný, and L. Beneš. Preparation and some physical properties of $(Bi_{1-x}Sb_x)_2Se_3$ single crystals. *Journal of Crystal Growth*, 179(1–2):144–152, 1997.

[88] V. A. Kulbachinskii, N. Miura, H. Nakagawa, H. Arimoto, T. Ikaida, P. Lostak, and C. Drasar. Conduction-band structure of $Bi_{2-x}Sb_xSe_3$ mixed crystals by Shubnikov–de Haas and cyclotron resonance measurements in high magnetic fields. *Physical Review B*, 59(24):15733–15739, 1999.

[89] J. Kašparová, v. Drašar, A. Krejčová, L. Beneš, P. Lošt'ák, W. Chen, Z. Zhou, and C. Uher. n-type to p-type crossover in quaternary $Bi_xSb_yPb_zSe_3$ single crystals. *Journal of Applied Physics*, 97(10):103720, 2005.

[90] J. Zhang, C.-Z. Chang, Z. Zhang, J. Wen, X. Feng, K. Li, M. Liu, K. He, L. Wang, X. Chen, Q.-K. Xue, X. Ma, and Y. Wang. Band structure engineering in $(Bi_{1-x}Sb_x)_2Te_3$ ternary topological insulators. *Nat Commun*, 2:574, 2011.

[91] I. Teramoto and S. Takayanagi. Relations between the electronic properties and the chemical bonding of $Sb_xBi_{2-x}Te_{3-y}Se_y$ system. *Journal of Physics and Chemistry of Solids*, 19(1):124–129, 1961.

[92] H. Shi, D. Parker, M.-H. Du, and D. J. Singh. Connecting Thermoelectric Performance and Topological-Insulator Behavior: Bi_2Te_3 and Bi_2Te_2Se from First Principles. *Physical Review Applied*, 3(1):014004, 2015.

[93] S. Schreyeck, K. Brunner, A. Kirchner, U. Bass, S. Grauer, C. Schumacher, C. Gould, G. Karczewski, J. Geurts, and L. W. Molenkamp. Kinetic limitation of chemical ordering in $Bi_2Te_{3-x}Se_x$ layers grown by molecular beam epitaxy. *Journal of Physics: Condensed Matter*, 28(14):145002, 2016.

[94] A. A. Abrikosov. Galvanomagnetic Phenomena in Metals in the Quantum Limit. *Soviet Journal of Experimental and Theoretical Physics*, 29:746, 1969.

[95] A. A. Abrikosov. Quantum magnetoresistance. *Physical Review B*, 58(5):2788–2794, 1998.

[96] P. Kapitza. The Study of the Specific Resistance of Bismuth Crystals and Its Change in Strong Magnetic Fields and Some Allied Problems. *Proceedings of the Royal Society of London A: Mathematical, Physical and Engineering Sciences*, 119(782):358–443, 1928.

[97] R. Xu, A. Husmann, T. F. Rosenbaum, M. L. Saboungi, J. E. Enderby, and P. B. Littlewood. Large magnetoresistance in non-magnetic silver chalcogenides. *Nature*, 390(6655):57–60, 1997.

[98] M. Lee, T. F. Rosenbaum, M. L. Saboungi, and H. S. Schnyders. Band-Gap Tuning and Linear Magnetoresistance in the Silver Chalcogenides. *Physical Review Letters*, 88(6):066602, 2002.

[99] M. M. Parish and P. B. Littlewood. Non-saturating magnetoresistance in heavily disordered semiconductors. *Nature*, 426(6963):162–165, 2003.

[100] M. M. Parish and P. B. Littlewood. Classical magnetotransport of inhomogeneous conductors. *Physical Review B*, 72(9):094417, 2005.

[101] J. Hu, M. M. Parish, and T. F. Rosenbaum. Nonsaturating magnetoresistance of inhomogeneous conductors: Comparison of experiment and simulation. *Physical Review B*, 75(21):214203, 2007.

[102] C. M. Wang and X. L. Lei. Linear magnetoresistance on the topological surface. *Physical Review B*, 86(3):035442, 2012.

[103] Y. Zhang, K. He, C.-Z. Chang, C.-L. Song, L.-L. Wang, X. Chen, J.-F. Jia, Z. Fang, X. Dai, W.-Y. Shan, S.-Q. Shen, Q. Niu, X.-L. Qi, S.-C. Zhang, X.-C. Ma, and Q.-K. Xue. Crossover of the three-dimensional topological insulator Bi_2Se_3 to the two-dimensional limit. *Nat Phys*, 6(8):584–588, 2010.

[104] H.-Z. Lu, W.-Y. Shan, W. Yao, Q. Niu, and S.-Q. Shen. Massive Dirac fermions and spin physics in an ultrathin film of topological insulator. *Physical Review B*, 81(11):115407, 2010.

[105] S. Hikami, A. I. Larkin, and Y. Nagaoka. Spin-Orbit Interaction and Magnetoresistance in the Two Dimensional Random System. *Progress of Theoretical Physics*, 63(2):707–710, 1980.

[106] B. L. Al'Tshuler and A. G. Aronov. Magnetoresistance of thin films and of wires in a longitudinal magnetic field. *Soviet Journal of Experimental and Theoretical Physics Letters*, 33:499, May 1981.

[107] G. Tkachov and E. M. Hankiewicz. Weak antilocalization in HgTe quantum wells and topological surface states: Massive versus massless Dirac fermions. *Physical Review B*, 84(3):035444, 2011.

[108] C.-X. Liu, H. Zhang, B. Yan, X.-L. Qi, T. Frauenheim, X. Dai, Z. Fang, and S.-C. Zhang. Oscillatory crossover from two-dimensional to three-dimensional topological insulators. *Physical Review B*, 81(4):041307, 2010.

[109] G. P. Mikitik and Y. V. Sharlai. Manifestation of Berry's Phase in Metal Physics. *Physical Review Letters*, 82(10):2147–2150, 1999.

[110] Y. Xu, I. Miotkowski, C. Liu, J. Tian, H. Nam, N. Alidoust, J. Hu, C.-K. Shih, M. Z. Hasan, and Y. P. Chen. Observation of topological surface state quantum Hall effect in an intrinsic three-dimensional topological insulator. *Nat Phys*, 10(12):956–963, 2014.

[111] R. Yoshimi, A. Tsukazaki, Y. Kozuka, J. Falson, K. S. Takahashi, J. G. Checkelsky, N. Nagaosa, M. Kawasaki, and Y. Tokura. Quantum Hall effect on top and bottom surface states of topological insulator $(Bi_{1-x}Sb_x)_2Te_3$ films. *Nat Commun*, 6, 2015.

[112] C.-X. Liu, X.-L. Qi, X. Dai, Z. Fang, and S.-C. Zhang. Quantum Anomalous Hall Effect in $Hg_{1-y}Mn_yTe$ Quantum Wells. *Physical Review Letters*, 101(14):146802, 2008.

[113] R. Yu, W. Zhang, H.-J. Zhang, S.-C. Zhang, X. Dai, and Z. Fang. Quantized Anomalous Hall Effect in Magnetic Topological Insulators. *Science*, 329(5987):61–64, 2010.

[114] N. Bloembergen and T. J. Rowland. Nuclear Spin Exchange in Solids: Tl^{203} and Tl^{205} Magnetic Resonance in Thallium and Thallic Oxide. *Physical Review*, 97(6):1679–1698, 1955.

[115] M. Li, C.-Z. Chang, L. Wu, J. Tao, W. Zhao, M. H. W. Chan, J. S. Moodera, J. Li, and Y. Zhu. Experimental Verification of the Van Vleck Nature of Long-Range Ferromagnetic Order in the Vanadium-Doped Three-Dimensional Topological Insulator Sb_2Te_3. *Physical Review Letters*, 114(14):146802, 2015.

[116] V. A. Kulbachinskii, A. Y. Kaminskii, K. Kindo, Y. Narumi, K. Suga, P. Lostak, and P. Svanda. Ferromagnetism in new diluted magnetic semiconductor $Bi_{2-x}Fe_xTe_3$. *Physica B: Condensed Matter*, 311(3–4):292–297, 2002.

[117] J. S. Dyck, P. Hájek, P. Lošt'ák, and C. Uher. Diluted magnetic semiconductors based on $Sb_{2-x}V_xTe_3$ $0.01 \leq x \leq 0.03$. *Physical Review B*, 65(11):115212, 2002.

[118] J. Choi, S. Choi, J. Choi, Y. Park, H.-M. Park, H.-W. Lee, B.-C. Woo, and S. Cho. Magnetic properties of Mn-doped Bi_2Te_3 and Sb_2Te_3. *physica status solidi (b)*, 241(7):1541–1544, 2004.

[119] J. S. Dyck, v. Drašar, P. Lošt'ák, and C. Uher. Low-temperature ferromagnetic properties of the diluted magnetic semiconductor $Sb_{2-x}Cr_xTe_3$. *Physical Review B*, 71(11):115214, 2005.

[120] Y. S. Hor, P. Roushan, H. Beidenkopf, J. Seo, D. Qu, J. G. Checkelsky, L. A. Wray, D. Hsieh, Y. Xia, S. Y. Xu, D. Qian, M. Z. Hasan, N. P. Ong, A. Yazdani, and R. J. Cava. Development of ferromagnetism in the doped topological insulator $Bi_{2-x}Mn_xTe_3$. *Physical Review B*, 81(19):195203, 2010.

[121] Y. H. Choi, N. H. Jo, K. J. Lee, J. B. Yoon, C. Y. You, and M. H. Jung. Transport and magnetic properties of Cr-, Fe-, Cu-doped topological insulators. *Journal of Applied Physics*, 109(7):07E312, 2011.

[122] D. A. Abanin and D. A. Pesin. Ordering of Magnetic Impurities and Tunable Electronic Properties of Topological Insulators. *Physical Review Letters*, 106(13):136802, 2011.

[123] P. P. J. Haazen, J.-B. Laloë, T. J. Nummy, H. J. M. Swagten, P. Jarillo-Herrero, D. Heiman, and J. S. Moodera. Ferromagnetism in thin-film Cr-doped topological insulator Bi_2Se_3. *Applied Physics Letters*, 100(8):082404, 2012.

[124] L. B. Abdalla, L. Seixas, T. M. Schmidt, R. H. Miwa, and A. Fazzio. Topological insulator Bi_2Se_3 (111) surface doped with transition metals: An *ab initio* investigation. *Physical Review B*, 88(4):045312, 2013.

[125] J.-M. Zhang, W. Ming, Z. Huang, G.-B. Liu, X. Kou, Y. Fan, K. L. Wang, and Y. Yao. Stability, electronic, and magnetic properties of the magnetically doped topological insulators Bi_2Se_3, Bi_2Te_3, and Sb_2Te_3. *Physical Review B*, 88(23):235131, 2013.

[126] C.-Z. Chang, J. Zhang, M. Liu, Z. Zhang, X. Feng, K. Li, L.-L. Wang, X. Chen, X. Dai, Z. Fang, X.-L. Qi, S.-C. Zhang, Y. Wang, K. He, X.-C. Ma, and Q.-K. Xue. Thin Films of Magnetically Doped Topological Insulator with Carrier-Independent Long-Range Ferromagnetic Order. *Advanced Materials*, 25(7):1065–1070, 2013.

[127] X. Kou, M. Lang, Y. Fan, Y. Jiang, T. Nie, J. Zhang, W. Jiang, Y. Wang, Y. Yao, L. He, and K. L. Wang. Interplay between Different Magnetisms in Cr-Doped Topological Insulators. *ACS Nano*, 7(10):9205–9212, 2013.

[128] Z. Zhang, X. Feng, M. Guo, K. Li, J. Zhang, Y. Ou, Y. Feng, L. Wang, X. Chen, K. He, X. Ma, Q. Xue, and Y. Wang. Electrically tuned magnetic order and magnetoresistance in a topological insulator. *Nat Commun*, 5:4915, 2014.

[129] J. G. Checkelsky, R. Yoshimi, A. Tsukazaki, K. S. Takahashi, Y. Kozuka, J. Falson, M. Kawasaki, and Y. Tokura. Trajectory of the anomalous Hall effect towards the quantized state in a ferromagnetic topological insulator. *Nat Phys*, 10(10):731–736, 2014.

[130] X. Kou, S.-T. Guo, Y. Fan, L. Pan, M. Lang, Y. Jiang, Q. Shao, T. Nie, K. Murata, J. Tang, Y. Wang, L. He, T.-K. Lee, W.-L. Lee, and K. L. Wang. Scale-Invariant Quantum Anomalous Hall Effect in Magnetic Topological Insulators beyond the Two-Dimensional Limit. *Physical Review Letters*, 113(13):137201, 2014.

[131] A. J. Bestwick, E. J. Fox, X. Kou, L. Pan, K. L. Wang, and D. Goldhaber-Gordon. Precise Quantization of the Anomalous Hall Effect near Zero Magnetic Field. *Physical Review Letters*, 114(18):187201, 2015.

[132] Y. Feng, X. Feng, Y. Ou, J. Wang, C. Liu, L. Zhang, D. Zhao, G. Jiang, S.-C. Zhang, K. He, X. Ma, Q.-K. Xue, and Y. Wang. Observation of the Zero Hall Plateau in a Quantum Anomalous Hall Insulator. *Physical Review Letters*, 115(12):126801, 2015.

[133] A. Kandala, A. Richardella, S. Kempinger, C.-X. Liu, and N. Samarth. Giant anisotropic magnetoresistance in a quantum anomalous Hall insulator. *Nat Commun*, 6:7434, 2015.

[134] C.-Z. Chang, W. Zhao, D. Y. Kim, H. Zhang, B. A. Assaf, D. Heiman, S.-C. Zhang, C. Liu, M. H. W. Chan, and J. S. Moodera. High-precision realization of robust quantum anomalous Hall state in a hard ferromagnetic topological insulator. *Nat Mater*, 14(5):473–477, 2015.

[135] C.-Z. Chang, W. Zhao, D. Y. Kim, P. Wei, J. K. Jain, C. Liu, M. H. W. Chan, and J. S. Moodera. Zero-Field Dissipationless Chiral Edge Transport and the Nature of Dissipation in the Quantum Anomalous Hall State. *Physical Review Letters*, 115(5):057206, 2015.

[136] A. Aharoni. *Introduction to the theory of ferromagnetism*. International Series of monographs on physics. Oxford University Press, second edition, 2000.

[137] G. I. Makovetskii and G. M. Shakhlevich. Magnetic properties of the $CrS_{1-x}Se_x$ system. *physica status solidi (a)*, 47(1):219–222, 1978.

[138] L. Néel. Some theoretical aspects of rock-magnetism. *Advances in Physics*, 4(14):191–243, 1955.

[139] M. Winnerlein, S. Schreyeck, S. Grauer, S. Rosenberger, K. M. Fijalkowski, C. Gould, K. Brunner, and L. W. Molenkamp. Epitaxy and Structural Properties of $(V,Bi,Sb)_2Te_3$ Layers Exhibiting the Quantum Anomalous Hall Effect. *Phys. Rev. Materials*, 1:011201, Jun 2017.

[140] F. D. M. Haldane. Model for a Quantum Hall Effect without Landau Levels: Condensed-Matter Realization of the "Parity Anomaly". *Physical Review Letters*, 61(18):2015–2018, 1988.

[141] M. Onoda and N. Nagaosa. Quantized Anomalous Hall Effect in Two-Dimensional Ferromagnets: Quantum Hall Effect in Metals. *Physical Review Letters*, 90(20):206601, 2003.

[142] Z. Qiao, S. A. Yang, W. Feng, W.-K. Tse, J. Ding, Y. Yao, J. Wang, and Q. Niu. Quantum anomalous Hall effect in graphene from Rashba and exchange effects. *Physical Review B*, 82(16):161414, 2010.

[143] K. Nomura and N. Nagaosa. Surface-Quantized Anomalous Hall Current and the Magnetoelectric Effect in Magnetically Disordered Topological Insulators. *Physical Review Letters*, 106(16):166802, 2011.

[144] X.-L. Qi, T. L. Hughes, and S.-C. Zhang. Chiral topological superconductor from the quantum Hall state. *Physical Review B*, 82(18):184516, 2010.

[145] M. Mogi, R. Yoshimi, A. Tsukazaki, K. Yasuda, Y. Kozuka, K. S. Takahashi, M. Kawasaki, and Y. Tokura. Magnetic modulation doping in topological insulators toward higher-temperature quantum anomalous Hall effect. *Applied Physics Letters*, 107(18):182401, 2015.

[146] X.-L. Qi, T. L. Hughes, and S.-C. Zhang. Topological field theory of time-reversal invariant insulators. *Physical Review B*, 78(19):195424, 2008.

[147] J. Wang, B. Lian, X.-L. Qi, and S.-C. Zhang. Quantized topological magnetoelectric effect of the zero-plateau quantum anomalous Hall state. *Physical Review B*, 92(8):081107, 2015.

[148] A. M. Essin, J. E. Moore, and D. Vanderbilt. Magnetoelectric Polarizability and Axion Electrodynamics in Crystalline Insulators. *Physical Review Letters*, 102(14):146805, 2009.

[149] M. C. Huang and P. Sikivie. Structure of axionic domain walls. *Physical Review D*, 32(6):1560–1568, 1985.

[150] F. Wilczek. Two applications of axion electrodynamics. *Physical Review Letters*, 58(18):1799–1802, 1987.

[151] R. D. Peccei and H. R. Quinn. **CP** Conservation in the Presence of Pseudoparticles. *Physical Review Letters*, 38(25):1440–1443, 1977.

[152] G. W. Fraser, A. M. Read, S. Sembay, J. A. Carter, and E. Schyns. Potential solar axion signatures in X-ray observations with the XMM–Newton observatory. *Monthly Notices of the Royal Astronomical Society*, 445(2):2146–2168, 2014.

[153] C. Beck. Axion mass estimates from resonant Josephson junctions. *Physics of the Dark Universe*, 7–8:6–11, 2015.

[154] L. Wu, M. Salehi, N. Koirala, J. Moon, S. Oh, and N. P. Armitage. Quantized Faraday and Kerr rotation and axion electrodynamics of a 3D topological insulator. *Science*, 354(6316):1124–1127, 2016.

[155] V. Dziom, A. Shuvaev, A. Pimenov, G. V. Astakhov, C. Ames, K. Bendias, J. Böttcher, G. Tkachov, E. M. Hankiewicz, C. Brüne, H. Buhmann, and L. W. Molenkamp. Observation of the universal magnetoelectric effect in a 3D topological insulator. *ArXiv e-prints*, March 2016.

[156] K. N. Okada, Y. Takahashi, M. Mogi, R. Yoshimi, A. Tsukazaki, K. S. Takahashi, N. Ogawa, M. Kawasaki, and Y. Tokura. Terahertz spectroscopy on Faraday and Kerr rotations in a quantum anomalous Hall state. *Nature Communications*, 7:12245, 2016.

[157] A. J. Niemi and G. W. Semenoff. Axial-Anomaly-Induced Fermion Fractionization and Effective Gauge-Theory Actions in Odd-Dimensional Space-Times. *Physical Review Letters*, 51(23):2077–2080, 1983.

[158] A. N. Redlich. Gauge Noninvariance and Parity Nonconservation of Three-Dimensional Fermions. *Physical Review Letters*, 52(1):18–21, 1984.

[159] S. Grauer, K. M. Fijalkowski, S. Schreyeck, M. Winnerlein, K. Brunner, R. Thomale, C. Gould, and L. W. Molenkamp. Scaling of the Quantum Anomalous Hall Effect as an Indicator of Axion Electrodynamics. *Phys. Rev. Lett.*, 118:246801, Jun 2017.

[160] H. P. Wei, D. C. Tsui, M. A. Paalanen, and A. M. M. Pruisken. *Scaling of the Integral Quantum Hall Effect*, pages 11–15. Springer, Berlin, 1987.

[161] S. V. Kravchenko and V. M. Pudalov. Does a scaling theory describe the magnetoconductivity of silicon metal-insulator-semiconductor structures? *JETP Lett*, 50(2), 1989.

[162] S. V. Kravchenko, B. K. Medvedev, V. G. Mokerov, V. M. Pudalov, D. A. Rinberg, and S. G. Semenchinsky. On the phase diagrams of the magnetoconductivity for 2D electron systems. *Surface Science*, 229(1):63–66, 1990.

[163] V. T. Dolgopolov, A. A. Shashkin, B. K. Medvedev, and V. G. Mokerov. Scaling under conditions of the integral quantum Hall effect. *Zh. Eksp. Teor. Fiz.*, 99(1):201–214, 1991.

[164] B. Huckestein. Scaling theory of the integer quantum Hall effect. *Reviews of Modern Physics*, 67(2):357–396, 1995.

[165] D. E. Khmel'nitskii. Quantization of Hall conductivity. *JETP lett*, 38(9):552, 1983.

[166] A. M. M. Pruisken. Dilute instanton gas as the precursor to the integral quantum Hall effect. *Physical Review B*, 32(4):2636–2639, 1985.

[167] A. M. Dykhne and I. M. Ruzin. Theory of the fractional quantum Hall effect: The two-phase model. *Physical Review B*, 50(4):2369–2379, 1994.

[168] M. Hilke, D. Shahar, S. H. Song, D. C. Tsui, Y. H. Xie, and M. Shayegan. Semicircle: An exact relation in the integer and fractional quantum Hall effect. *Europhysics Letters*, 46(6):775, 1999.

[169] P. M. Ostrovsky, I. V. Gornyi, and A. D. Mirlin. Theory of anomalous quantum Hall effects in graphene. *Physical Review B*, 77(19):195430, 2008.

List of publications

* N. V. Tarakina, S. Schreyeck, T. Borzenko, **S. Grauer**, C. Schumacher, G. Karczewski, C. Gould, K. Brunner, H. Buhmann, L. W. Molenkamp. Microstructural characterisation of Bi_2 Se_3 thin films.
Journal of Physics: Conference Series **471**: 012043 (2013).

* N. V. Tarakina, S. Schreyeck, M. Luysberg, **S. Grauer**, C. Schumacher, G. Karczewski, K. Brunner, C. Gould, H. Buhmann, R. E. Dunin-Borkowski, L. W. Molenkamp. Suppressing Twin Formation in Bi_2Se_3 Thin Films.
Advanced Materials Interfaces **1**, 1400134 (2014).

* M. Orlita, B. A. Piot, G. Martinez, N. Kumar, K. Sampath, C. Faugeras, M. Potemski, C. Michel, E. M. Hankiewicz, T. Brauner, Č. Drašar, S. Schreyeck, **S. Grauer**, K. Brunner, C. Gould, C. Brüne, L. W. Molenkamp. Magneto-Optics of Massive Dirac Fermions in Bulk Bi_2Se_3.
Physical Review Letters **114**, 186401 (2015).

* **S. Grauer**, S. Schreyeck, M. Winnerlein, K. Brunner, C. Gould, L. W. Molenkamp. Coincidence of superparamagnetism and perfect quantization in the quantum anomalous Hall state.
Physical Review B **92**, 201304 (2015).

* S. Schreyeck, K. Brunner, A. Kirchner, U. Bass, **S. Grauer**, C. Schumacher, C. Gould, G. Karczewski, J. Geurts, L. W. Molenkamp. Kinetic limitation of chemical ordering in $Bi_2Te_{3-x}Se_x$ layers grown by molecular beam epitaxy.
Journal of Physics: Condensed Matter **28**, 145002 (2016).

* S. Wiedmann, A. Jost, B. Fauqué, J. van Dijk, M. J. Meijer, T. Khouri, S. Pezzini, **S. Grauer**, S. Schreyeck, C. Brüne, H. Buhmann, L. W. Molenkamp, N. E. Hussey. Anisotropic and strong negative magnetoresistance in the three-dimensional topological insulator Bi_2Se_3.
Physical Review B **94**, 081302 (2016).
* T. Peixoto, H. Bentmann, S. Schreyeck, M. Winnerlein, C. Seibel, H. Maaß, M. Al-Baidhani, K. Treiber, S. Schatz, **S. Grauer**, C. Gould, K. Brunner, A. Ernst, L. W. Molenkamp, F. Reinert. Impurity states in the magnetic topological insulator V:$(Bi,Sb)_2Te_3$.
Physical Review B **94**, 195140 (2016).
* **S. Grauer**, K. Fijalkowski, S. Schreyeck, M. Winnerlein, K. Brunner, R. Thomale, C. Gould, L. W. Molenkamp. Scaling of the Quantum Anomalous Hall Effect as an Indicator of Axion Electrodynamics.
Physical Review Letters **118**, 246801 (2017).
* M. Winnerlein, S. Schreyeck, **S. Grauer**, S. Rosenberger, K. Fijalkowski, C. Gould, K. Brunner, L. W. Molenkamp. Epitaxy and Structural Properties of (V,Bi,Sb)$_2$Te$_3$ Layers Exhibiting the Quantum Anomalous Hall Effect.
Physical Review Materials **1**, 011201 (2017).

Acknowledgements

Finally I want to thank the people who all contributed in their way to the success of this thesis.

- Prof. Dr. Laurens W. Molenkamp for guidance and the chance to work at EP3
- PD Dr. Charles Gould for all the discussions, insights and help
- Maciek Sawicki for his support with SQUID measurements
- Steffen Schreyeck and Martin Winnerlein for discussion and the growth of numerous samples
- Kajetan Fijalkowski for carrying the project on
- Tanja Borzenko for all the help with lithography
- Volkmar Hock for his support in the cleanroom
- Roland Ebert and Cornelius Ziga for a continuous supply of liquid helium and help with cryogenics
- All the members of EP3 for a good work climate

Special thanks go to my family that always showed interest in my work and supported me in many ways.